الجمهورية الجزائرية الديمقراطية الشعبية
République Algérienne Démocratique et Populaire
وزارة التعليم العالي والبحث العلمي
Ministère de l'enseignement supérieur et la recherche scientifique

Université 20 Août 1955

- Skikda -

Faculté de Technologie
Départment de Génie Electrique

Réf : D012126009D

جامعة 20 أوت 1955

- سكيكدة -

كلية التكنولوجيا قسم
الهندسة الكهربائية

THÈSE DE DOCTORAT

En vue de l'obtention du diplôme de doctorat de 3^{ième} cycle (D-LMD)

Option : Electrotechnique
Specialité: Commandes électriques
Laboratoire LES

Commande et diagnostic des systèmes d'énergies renouvelables multi-sources

Présenté par

Ilyes Djemili

Soutenue le 16/04/2026 devant le jury composé de :

Comité du jury:

Nom et Prénom :	**Grade**	**Établissement d'affiliation**	**Désignation**
Pr. Omar Boudebbouz	Professeur	Université 20 Août 1955-Skikda	Président
Pr. Ammar Medoued	Professeur	Université 20 Août 1955-Skikda	Directeur de Thèse
Pr. Youcef Soufi	Professeur	Université Larbi Tebessi -Tébessa	Co-directeur
Pr. Ahcene Boukadoum	Professeur	Université 20 Août 1955-Skikda	Examinateur
Pr. Nabil Kahoul	Professeur	Université Badji Mokhtar - Annaba	Examinateur
Dr. Moufid Mohammedi	MCA	Université Badji Mokhtar - Annaba	Examinateur

Université de Skikda, FT – 2025

الجمهورية الجزائرية الديمقراطية الشعبية
People's Democratic Republic of Algeria
وزارة التعليم العالي والبحث العلمي
Ministry of Higher Education and Scientific Research

University of 20 August 1955

- Skikda -

Faculty of Technology

Electrical Engineering Department

Ref : D012126009D

جامعة 20 أوت 1955

- سكيكدة -

كلية التكنولوجيا قسم الهندسة الكهربائية

DOCTORAL THESIS

With a view to obtaining the 3rd cycle doctoral degree (D- LMD)
option : Electrical Engineering
Speciality: Electrical control
LES Laboratory

Control and diagnosis of multi-source renewable energy systems

Presented by

Ilyes Djemili

Defended on 16/04/2026 before the jury composed of:

Committee of Jury:

First and Last Name :	Grade	Institution of Affiliation	Designation
Pr. Omar Boudebbouz	Professor	University of 20 August 1955-Skikda	President
Pr. Ammar Medoued	Professor	University of 20 August 1955-Skikda	Supervisor
Pr. Youcef Soufi	Professor	Larbi Tebessi University-Tebessa	Co-Supervisor
Pr. Ahcene Boukadoum	Professor	University of 20 August 1955-Skikda	Examiner
Pr. Nabil Kahoul	Professor	Université Badji Mokhtar - Annaba	Examiner
Dr. Moufid Mohammedi	MCA	Université Badji Mokhtar - Annaba	Examiner

Skikda University, FT – 2025

ملخص

تقدّم هذه الأطروحة مقاربات جديدة تهدف إلى تعزيز موثوقية وكفاءة أنظمة الطاقة المتجددة، مع التركيز على مراقبة حالة توربينات الرياح (WT) والتحكم في الأنظمة الكهروضوئية (PV). في ما يخص توربينات الرياح، تم تطوير تقنيات متقدمة للتشخيص تجمع بين تحليل الاهتزازات واستخدام الذكاء الاصطناعي الحديث. تسمح هذه الأساليب بالكشف المبكر عن الأعطال الميكانيكية، خصوصاً في المحامل وصناديق التروس والمولدات، من خلال توظيف معالجة الإشارات ونماذج التعلم العميق. كما يتيح دمج الذكاء الاصطناعي القابل للتفسير بناء نماذج يمكن فهمها وتحديداً موثوقاً لأسباب الأعطال، وقد تم التحقق من فعاليتها من خلال تجارب شاملة على بيانات حقيقية ومحاكاة من مزارع الرياح. تسهم هذه الاستراتيجيات الذكية في خفض تكاليف الصيانة، إطالة عمر الأنظمة، وتقليل فترات التوقف غير المخطط لها، من خلال الانتقال من الصيانة التفاعلية إلى الصيانة التنبؤية في محطات طاقة الرياح الكبرى.

أما بالنسبة للأنظمة الكهروضوئية، فقد تم تطبيق عدة خوارزميات لتتبع نقطة القدرة العظمى(MPPT) ، تشمل تقنيات تحكم كلاسيكية وذكية تحت ظروف إشعاع شمسي متغيرة. أظهرت المحاكاة تأثير الطرق التكيفية في تحسين إنتاج الطاقة ورفع أداء الأنظمة الكهروضوئية. تمثل هذه المساهمات خطوة نحو حلول موثوقة وفعالة من حيث التكلفة لدمج وإدارة مصادر الطاقة المتجددة ضمن شبكات الكهرباء الحديثة.

الكلمات المفتاحية: توربينات الرياح، تشخيص أعطال المحامل، إشارة الاهتزاز، إزالة تضمين الغلاف، التشخيص الذكي، الشبكات العصبية الالتفافية العميقة، الأنظمة الكهروضوئية، تتبع نقطة الطاقة القصوى.

RESUME

Cette thèse présente de nouvelles approches visant à améliorer la fiabilité et l'efficacité opérationnelle des systèmes d'énergie renouvelable, en mettant l'accent sur la surveillance des éoliennes (WT) et le contrôle des systèmes photovoltaïques (PV). Pour les éoliennes, des techniques avancées de diagnostic ont été développées en combinant l'analyse vibratoire et l'intelligence artificielle de pointe. Ces méthodes permettent la détection précoce des défaillances mécaniques — notamment au niveau des roulements, des multiplicateurs et des générateurs — grâce à l'exploitation du traitement du signal et des modèles d'apprentissage profond. L'intégration de l'intelligence artificielle (AI) rend les modèles interprétables et assure une identification fiable des causes de pannes, validée par des expérimentations sur des données réelles et simulées de parcs éoliens. Ces stratégies de surveillance intelligente réduisent les coûts de maintenance, prolongent la durée de vie des systèmes et minimisent les arrêts non planifiés en favorisant le passage d'une maintenance réactive à une maintenance prédictive dans les centrales éoliennes à grande échelle.

Concernant la partie photovoltaïque, la thèse met en œuvre plusieurs algorithmes de Maximum Power Point Tracking (MPPT), incluant des stratégies de commande classiques et intelligentes, sous des conditions d'irradiance variables. Les simulations démontrent l'impact des méthodes adaptatives MPPT sur l'optimisation du rendement énergétique et l'amélioration des performances des systèmes PV. Ensemble, ces contributions favorisent des solutions fiables, économiques et adaptées à l'intégration et à la gestion des sources d'énergie renouvelable dans les réseaux électriques modernes.

Mots-clés : Mots-clés : Éolienne, Diagnostic des défauts de roulement, Signal vibratoire, Démodulation d'enveloppe, Diagnostic intelligent, Réseaux de neurones convolutifs profonds, Systèmes photovoltaïques, Suivi du point de puissance maximale, Particle Swarm Optimization.

Abstract

This thesis presents novel approaches for enhancing the reliability and operational efficiency of renewable energy systems, with emphasis on wind turbine (WT) condition monitoring and photovoltaic (PV) control. For wind turbines, advanced diagnosis techniques are developed combining vibration-based analysis, and cutting-edge artificial intelligence. These methods enable early detection of mechanical faults—particularly in bearings, gearboxes, and generators—by leveraging signal processing, and deep learning models. The integration of AI further allows for interpretable models and reliable identification of fault causes, which is validated through comprehensive experiments on real and simulated wind farm datasets. Such intelligent monitoring strategies reduce maintenance costs, extend system lifespan, and minimize unplanned downtime by supporting a shift from reactive to predictive maintenance in large-scale wind power plants.

On the PV side, the thesis implements several Maximum Power Point Tracking (MPPT) algorithms—including both classical and intelligent control strategies—under dynamic irradiance conditions. Simulations demonstrate the impact of adaptive MPPT methods on optimizing energy yield and improving PV performance. Together, these contributions advance high-availability, cost-effective solutions for the integration and management of renewable energy sources in modern power systems

Keywords: Wind Turbine, Bearing Fault Diagnosis, Vibration Signal, Envelope Demodulation, Intelligent Diagnosis, Deep Convolutional Neural Networks, Photovoltaic systems, Maximum Power Point Tracking, Particle Swarm Optimization.

Table of contents

ملخص ____ **I**

RESUME ____ **II**

Abstract ____ **III**

Table of contents ____ **IV**

List of figures ____ **VIII**

Liste of tables ____ **X**

Chapter 01 : Introduction _______________________________________ ***1***

1.1 Background ____ 1

1.2 Motivations ____ 2

1.3 Project scope ____ 3

1.4 Thesis outline ____ 4

Chapter 02 : Overview of Renewable Energy ___________________________ ***5***

2.1 Biomass/Bioenergy ____ 5

2.2 Hydroelectric Energy ____ 6

2.3 Geothermal Energy ____ 7

2.4 Wind energy ____ 9

2.4.1 Types of Wind Turbines _______________________________________ 10

- Horizontal-Axis Wind Turbines (HAWT) ________________________________ 10
- Vertical-Axis Wind Turbines (VAWT) ________________________________ 11

2.4.2 Overview of Wind Power Systems (WPS) ____________________________ 12

- Fixed-Speed Wind Turbines ____ 13
- Variable-Speed Wind Turbines with Partial Power Converters _______________ 13
- Variable-Speed Concept with Full-Scale Power Converters __________________ 15

2.5 Photovoltaic System ____ 16

2.5.1 photovoltaic effect ____ 17

2.5.2 Photovoltaic cells ____ 18

- Types of Photovoltaic Cells ____ 18

2.5.3 Photovoltaic modules ____ 19

- Association of Photovoltaic Cells ______________________________________ 19

2.5.4 Fault Detection and Diagnosis in Photovoltaic Systems ____________________ 22

- Introduction ____ 22
- Classification of PV System Faults ______________________________________ 22
- Fault Detection and Diagnosis Methods ____________________________________ 24

Chapter 03 : Introduction to Wind Turbines Failures and Diagnosis Techniques ***27***

3.1 Introduction ______ 27

3.2 Common Failures in Wind Energy Systems ______ 28

3.2.1 Electrical Control System Failures ______ 30

3.2.2 Yaw System Failures ______ 30

3.2.3 Grid Connection Failures ______ 30

3.2.4 Hydraulic System Failures ______ 31

3.2.5 Blade Failures ______ 31

3.2.6 Failures in Electrical Generators ______ 32

3.2.7 Gearbox Failures ______ 36

3.3 Definition of Maintenance ______ 36

3.4 Types of Maintenance ______ 37

3.4.1 Reactive Maintenance ______ 37

3.4.2 Proactive Maintenance ______ 38

3.5 Dependability ______ 40

3.5.1 Definition ______ 40

3.5.2 Attributes ______ 41

3.6 Fault Diagnosis Techniques ______ 42

3.6.1 Model-Based Fault Diagnosis ______ 42

3.6.2 Signal-Based Fault Diagnosis ______ 43

3.6.3 Knowledge-Based Fault Diagnosis ______ 43

3.6.4 Hybrid Fault Diagnosis ______ 44

3.7 Vibration Analysis ______ 44

3.7.1 Time domain analysis ______ 45

- Peak Amplitude ______ 46
- Mean Amplitude ______ 46
- Root Mean Square (RMS) Amplitude ______ 46
- Skewness ______ 47
- Kurtosis ______ 47
- Entropy ______ 47

3.7.2 Frequency domain analysis ______ 47

3.7.3 Envelope Analysis ______ 48

3.7.4 Time-Frequency Analysis ______ 49

- Variational Mode Decomposition (VMD) ______ 50
- EMD, EEMD, CEEMDAN and Improved CEEMDAN ______ 52

3.8 Conclusion ______ 54

Chapter 04 : Contribution To Rolling Element Bearing Faults Identification In WT ______ ***55***

4.1 Introduction ____ 55
4.2 Experimental setup____ 56
4.2.1 CWRU Bearing Test Rig ____ 56
4.2.2 Real-World faulty bearing of a wind turbine generator provided by the Green Power Monitoring Systems (U.S) ____ 58
4.3 Proposed Methodology ____ 59
4.3.1 Signal decomposition ____ 61
4.3.2 Signal pre-processing____ 62
4.3.3 Envelope Analysis ____ 63
4.4 Application Of The Proposed Model On CWRU Setup _______________________ 64
4.4.1 Outer Race Bearing Fault Analysis_______________________________________ 64
4.4.2 Inner Race Bearing Fault Analysis _______________________________________ 66
4.4.3 Rolling Element Bearing Fault Analysis ___________________________________ 68
4.5 comparison with literature methods_______________________________________ 70
4.6 Real-World Validation of Bearing Fault Detection Methodology on Wind Turbine Data _ 71
4.7 Conclusion ____ 71

Chapter 05 : Contribution To An Intelligent Bearing Diagnosis __________ 73

5.1 Introduction ____ 73
5.2 Data Preparation and Experimental Setup ___________________________________ 73
5.3 Experiments Procedure ____ 75
5.3.1 Signal Decomposition ____ 77
5.3.2 Discrete Signal Separation ____ 78
5.3.3 Image Generation ____ 79
5.4 Machine Learning Technique ____ 81
5.5 Experimental Settings and Results ___________________________________ 82
5.6 Comparison with other CNNs and state-of-the-art methods ____________________ 84
5.7 Conclusion ____ 85

Chapter 06 : A Study of MPPT control techniques for PV systems under normal and partial shading _____________________________________ 87

6.1 Introduction ____ 87
6.2 Maximum Power Point Tracking Techniques ___________________________ 88
6.2.1 Conventional Methods____ 88
- Perturb and Observe (P&O) ____ 88
- Incremental Conductance Algorithm (INC)___________________________________ 90
- Hill Climbing Algorithm ____ 91
6.2.2 soft computing techniques____ 92
- Fuzzy Logic Controller (FLC) ____ 92
- Particle Swarm Optimization (PSO) ___________________________________ 93

6.3 SIMULATION AND RESULTS ____ 95
6.3.1 Model design and simulation ____ 95
6.3.2 Results under different radiation ____ 97
- Simulation using Perturb and Observe technique ____ 98
- Simulation using Incremental Conductance ____ 101
- Simulation using Particle Swarm Optimization ____ 103
- Simulation using Fuzzy Logic Control ____ 106

6.3.3 Results under partial shading ____ 108
- Simulation using Perturb and Observe technique ____ 108
- Simulation using Incremental Conductance ____ 109
- Simulation using Particle Swarm Optimization ____ 111
- Simulation using Fuzzy Logic Control ____ 112

6.4 Conclusion ____ 113

General conclusion and perspectives ____ ***115***

Appendixes ____ ***117***

Appendix A.1 ____ 117
Appendix A.2 ____ 118
Appendix A.3 ____ 118

References ____ ***120***

List of figures

Figure 1 : Cycle of biomass energy [2] 6
Figure 2 : Operation of a hydroelectric power plant [4] 7
Figure 3: Geothermal Energy [9] 8
Figure 4 : configuration of the wind turbine system 9
Figure 5 : Horizontal Axis Wind Turbine (HAWT) 11
Figure 6 : Vertical-Axis Wind Turbines (VAWT) 12
Figure 7 : configuration of a wind power generation system 12
Figure 8 : Fixed speed of a wind turbine using a SCIG [15] 13
Figure 9 : variable speed of a wind turbine with a DFIG [15] 14
Figure 10 : variable speed direct-drive of a wind turbine with a PMSG [15] 15
Figure 11 : The photovoltaic effect 17
Figure 12 : Monocrystalline silicon cells 18
Figure 13 : Polycrystalline silicon cells 18
Figure 14 : Thin-film solar cells 19
Figure 15 : Association of photovoltaic cells in series 20
Figure 16 : Association of photovoltaic cells in parallel 21
Figure 17 : component failure rates of wind turbines [26] 29
Figure 18 : Failure rates of electrical generator [33] 32
Figure 19 : Ball bearing components 35
Figure 20 : Dependability tree [47] 42
Figure 21 : Case Western Reserve University (CWRU) test rig [97] 57
Figure 22 : Inner race fault on the high-speed shaft bearing [99] 58
Figure 23 : Proposed method [96] 60
Figure 24 : ICEEMDAN decomposition of a bearing with inner race defect 61
Figure 25 : Correlation coefficient between original signal and its IMFs 62
Figure 26 : Squared envelope spectrum of a faulty bearing (with inner crack) 64
Figure 27 : Results obtained from a bearing with Outer race crack 65
Figure 28 : Kurtosis of each order P of an inner race cracked bearing 67
Figure 29 : Signal transformation of an Inner race cracked bearing 67
Figure 30 : the squared envelope spectrum of a bearing with inner race crack: (a) without processing, (b) using our proposed method 68
Figure 31 : Rolling element-fault results obtained using our proposed methods: (a) Correlation coefficient between raw signal and it's IMFs, (b) residual signal after Autoregressive filtering of 1st IMF, (c) Enhanced residual signal with MEDA and (d) it's Squared envelope spectrum 69
Figure 32 : Squared envelope spectrum of 48th day 71
Figure 33 : Data augmentation with overlap 74
Figure 34 : VMD-AR-ConvNext Methodology 76
Figure 35 : VMD decomposition result 77

Figure 36 : Correlation coefficient between raw signal and its IMFs ... 78
Figure 37 : Kurtosis of each order P ... 78
Figure 38 : Hilbert envelope spectrum ... 79
Figure 39 : The results of Hilbert envelope spectrum of different bearing state: (a) healthy bearing, (b) Inner race defect, (c) outer race defect, and (d) rolling element defect ... 80
Figure 40 : Transfer learning framework ... 81
Figure 41 : Bearing fault diagnosis based on fine-tuning ... 82
Figure 42 : The accuracy and loss curves of the ConvNeXt model ... 83
Figure 43 : The confusion matrix of the test dataset ... 84
Figure 44 : flowchart of the Perturb and Observe (P&O) algorithm ... 89
Figure 45 :Flowchart of Incremental Conductance (INC) algorithm ... 91
Figure 46 : Flowchart of the Fuzzy Logic Controller (FLC) ... 93
Figure 47 : Flowchart of the Particle Swarm Optimization (PSO) ... 94
Figure 48 : PV string configuration under partial shading ... 96
Figure 49 : The proposed SIMULINK model ... 97
Figure 50 : time-varying irradiance profile ... 98
Figure 51 : The SIMULINK block of P&O technique ... 99
Figure 52 : The parameters for the P&O algorithm ... 99
Figure 53 : The P-V diagram of PV module using P&O ... 100
Figure 54 : The output power at the level of the load using P&O technique ... 101
Figure 55 : The SIMULINK block of the INC technique ... 102
Figure 56 : The P-V diagram of PV module using INC ... 102
Figure 57 : The output power at the level of the load using INC technique ... 103
Figure 58 : The SIMULINK block of PSO technique ... 104
Figure 59 : The P-V diagram of PV module using PSO ... 104
Figure 60 : The output power at the level of the load using PSO technique ... 105
Figure 61 : The SIMULINK block of FLC technique ... 106
Figure 62 : The output power at the level of the load using FLC technique ... 107
Figure 63 : The P-V diagram of PV module using P&O under partial shading ... 108
Figure 64: The output power at the level of the load using P&O technique under partial shading ... 109
Figure 65 : The P-V diagram of PV module using INC under partial shading ... 110
Figure 66 : The output power at the level of the load using INC technique under partial shading ... 111
Figure 67 : The P-V diagram of PV module using PSO under partial shading ... 111
Figure 68 : The output power at the level of the load using PSO technique under partial shading ... 112
Figure 70 : The output power at the level of the load using FLC technique under partial shading ... 112
Figure 69 : The P-V diagram of PV module using FLC under partial shading ... 113

Liste of tables

Table 1 : Bearing fault frequencies 58
Table 2 : Comparison of our method with other advanced bearing-fault-diagnosis methods 70
Table 3 : Dataset division 75
Table 4 : Comparison of the proposed method with state-of-art approaches and DL architectures 85
Table 5 : JA SOLAR JAM6-60 250W parameters 95

1

Introduction

1.1 Background

The transition to renewable energy is reshaping the global power sector as societies strive to meet rising electricity demands with minimal environmental impact. Among renewable options, wind turbines (WT) and photovoltaic (PV) systems have emerged as key contributors, each presenting unique technical challenges. Modern wind turbines are increasingly deployed offshore and in remote locations, operating under fluctuating loads and harsh weather. Their mechanical complexity leaves them vulnerable to component failures—especially in bearings, gearboxes, and generators—which can lead to costly outages. To mitigate this, advanced condition monitoring techniques, involving vibration analysis, signal processing, and artificial intelligence, are now employed to detect and diagnose faults early, enabling predictive maintenance and improving system reliability.

Meanwhile, PV systems face challenges of their own: variable irradiance and shading can cause the system's power output to fluctuate, leading to substantial efficiency losses if not properly managed. Controlling the power electronics interface and employing robust Maximum Power Point Tracking (MPPT) algorithms are essential to maximize the energy harvested from sunlight. Successful MPPT control requires real-time adaptation to changes in solar input, partial shading, and temperature, making it a cornerstone of PV performance and economic viability. Collectively, these strategies—fault detection in wind turbines and MPPT control in PV—are vital for ensuring the reliability, efficiency, and rapid expansion of renewable energy systems in modern grids.

1.2 Motivations

As the demand for reliability and safety in multi-power systems continues to grow, it becomes essential to detect and address anomalies and potential faults at an early stage, so then efficient Fault-tolerant control (FTC) mechanisms can then be built to minimize performance degradation and avoid hazardous situations that might lead to system downtime. Early detection and identification of faults are also vital to maintaining optimal energy production throughout the system's lifespan. This ensures the safety of operations, reduces risks to human life, and minimizes power output losses.
Wind power stands out as the fastest-growing sector. Over the past decade, global wind energy capacity has seen an average annual growth rate of 30%. However, The harsh operational conditions and extreme environments in which wind turbines operate make them susceptible to various faults, leading to substantial maintenance requirements, it has been shown that bearing failures cause around 70% of gearbox downtime and 21–70% of generator downtime and more than 50% of all coasts of faults on gearbox, therefore, condition monitoring and early fault diagnosis of WT for bearings have become extremely precious and intensively studied in recent years. This not only improves the safety and reliability of wind turbines but also reduces maintenance costs and enhances overall efficiency. By adopting such measures, renewable energy systems can deliver sustainable, cost-effective, and reliable power to meet the growing demands of modern society.

In hybrid and stand-alone renewable energy systems, maximizing energy extraction from available resources is crucial for efficiency, cost-effectiveness, and system reliability. Variability in solar irradiance and wind speed leads to constant shifts in the operating point of photovoltaic and wind generators. Without effective control, these systems may operate far below their potential, resulting in energy loss and reduced return on investment. Maximum Power

Point Tracking (MPPT) techniques are designed to dynamically adapt the converters' operation, ensuring that renewable generators continuously deliver their optimal output regardless of environment changes. The motivation lies in the need to address the shortcomings of conventional MPPT algorithms and to explore intelligent, robust approaches capable of coping with rapid fluctuations, partial shading, and system uncertainties of the photovoltaic systems. Enhanced MPPT control directly contributes to the overall resilience and sustainability of modern renewable power systems.

1.3 Project scope

Wind Turbine Bearing Diagnosis

The focus of this project is to improve wind turbine bearing system diagnosis, which is essential for reliability as well as efficiency. Advanced methods like vibration analysis and machine learning will be implemented for early defect detection because bearing failures significantly increase wind turbine downtime and maintenance expenses. In order to increase safety, lower expenses, and guarantee continuous energy production, these techniques will detect problems under various circumstances and be verified through simulations and experiments.

Control of PV Energy Systems

To ensure effective energy management in photovoltaic systems, this part of the work focuses on evaluating MPPT control strategies under various operating conditions. The scope includes developing and simulating multiple MPPT control algorithms using MATLAB/Simulink. Four techniques—P&O, INC, PSO, and FLC—are implemented under identical PV configurations. Their performance is evaluated based on convergence speed, stability, and tracking efficiency under varying irradiance and shading. The study also assesses the suitability of each method for practical PV systems, providing guidelines for selecting appropriate control strategies in real-world installations.

1.4 Thesis outline

This thesis is organized as follows:
The initial chapters provide an overview of renewable energy sources, focusing particularly on photovoltaic and wind power systems and their role in modern energy supply. Subsequent chapters delve into the fundamentals of fault diagnosis and maintenance in wind turbines, highlighting key challenges and advanced diagnostic strategies. The core contributions of the thesis revolve around the diagnosis of wind turbine bearing faults using signal processing and machine learning methods. Later sections discuss the control and optimization of PV systems, with specific emphasis on Maximum Power Point Tracking (MPPT) algorithms. Finally, the thesis compares different MPPT approaches under various operating scenarios and discusses their implementation, effectiveness, and limitations.

2

Overview of Renewable Energy

An energy source is deemed renewable if its consumption does not restrict its future supply. This pertains to energy sourced from solar, wind, hydro, geothermal, and biomass resources, as these are naturally regenerated within a human timescale, regardless of humidity or aridity. Conversely, fossil fuels and nuclear energy are finite resources.

The energy landscape of the 21st century is anticipated to be influenced by emerging entities within the renewable energy industry, promoting sustainable development. Solar energy is captured through solar power systems, while wind energy is employed in wind turbine systems, both facilitating the shift towards a more sustainable energy future.[1]

A broad review of renewable energy sources will be given in this chapter, with particular attention given to photovoltaic solar and wind systems, which best reflect the state of renewable energy today.

2.1 Biomass/Bioenergy

Biomass refers to the biodegradable fraction of products, waste, and residues of biological origin derived from agriculture, animal husbandry, fishing, aquaculture, as well as the biodegradable portion of industrial and municipal waste. It can be utilized primarily in two ways:

- Through the fermentation of organic waste, during which methane gas is produced and can be harnessed as a source of energy;
- By direct incineration of biomass to generate heat.

In both cases, the thermal energy generated can be converted into electricity using thermal power plants. Biomass is considered a renewable energy source, provided that the rate of consumption does not exceed the rate of natural regeneration.

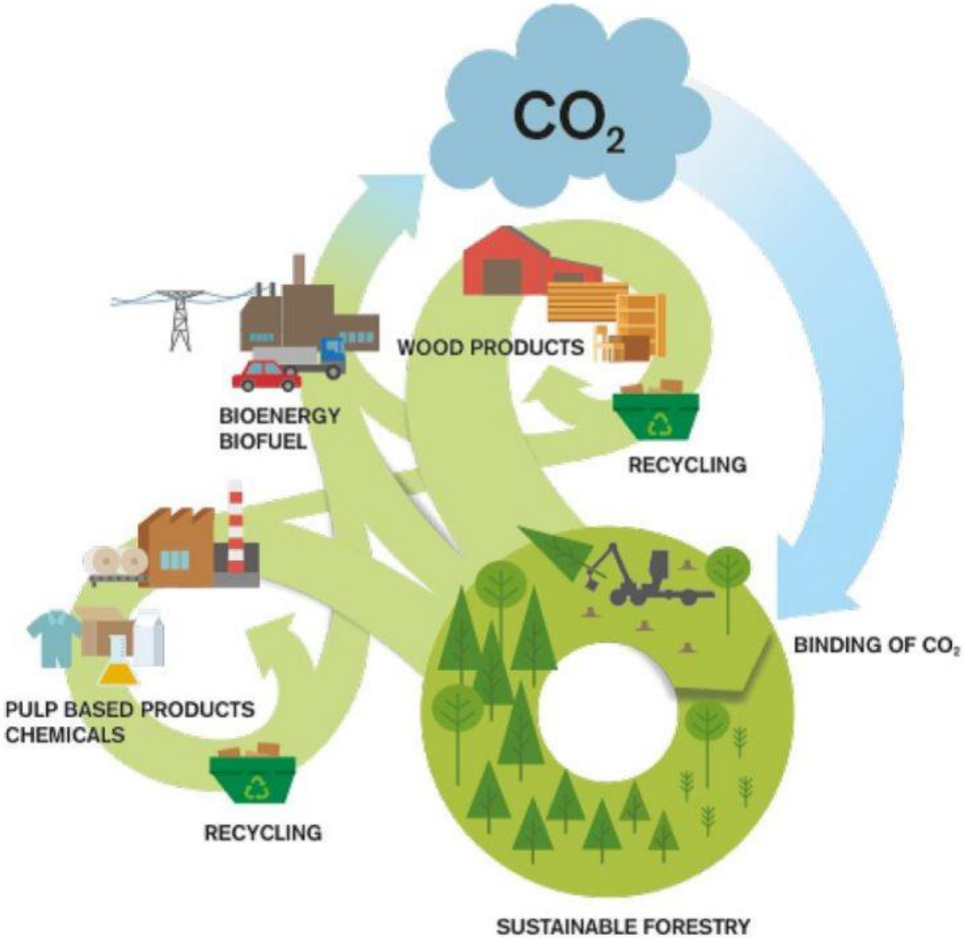

Figure 1 : Cycle of biomass energy [2]

A key advantage of biomass energy lies in its carbon neutrality: the carbon dioxide released during combustion is approximately equal to the amount absorbed by the plants during their growth, thus maintaining a balanced carbon cycle in the atmosphere.[3]

2.2 Hydroelectric Energy

Hydropower remains the most mature and widely developed form of renewable energy. It involves the conversion of the kinetic energy of flowing water into electrical energy through one or more hydraulic turbines connected to electrical generators. The maximum power output depends on the height of the water fall, the flow rate, and the mechanical characteristics of the turbine.

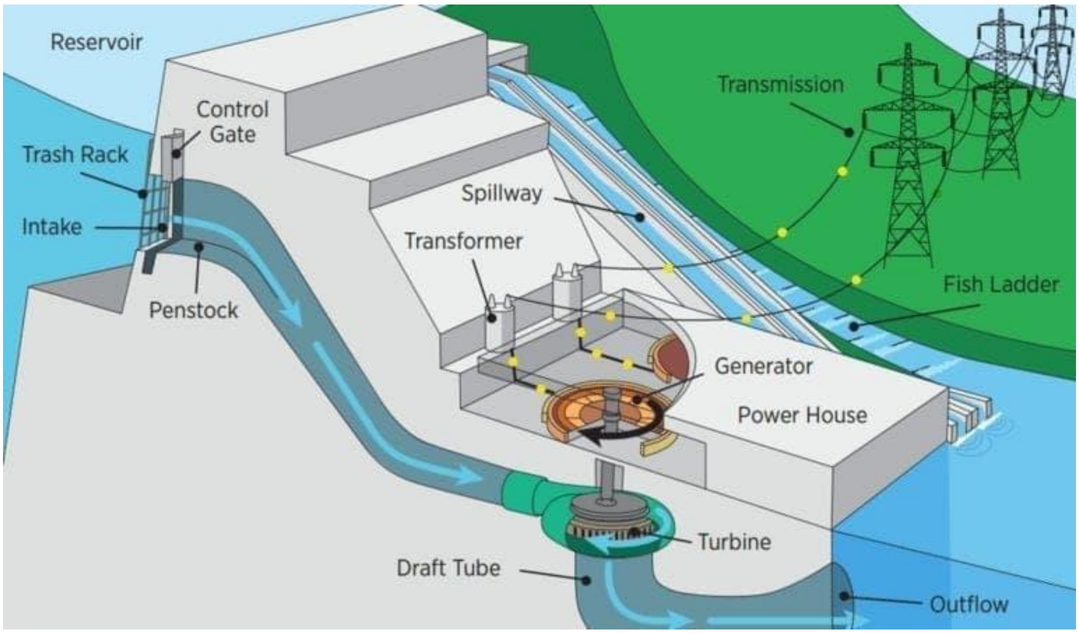

Figure 2 : Operation of a hydroelectric power plant [4]

One of the key advantages of hydroelectric energy is its non-intermittent nature. The technology required for its deployment is well-established, maintenance costs are relatively low, and hydroelectric installations are designed for long operational lifespans.[5]

However, this energy source also presents several drawbacks. These include high initial construction costs, noise pollution, significant impact on aquatic ecosystems, large-scale infrastructure requirements, and the limited availability of suitable sites for exploitation.[6]

2.3 Geothermal Energy

Within the Earth's crust, there is a natural temperature difference of about 3°C per 100 meters of depth. Geothermal energy seeks to understand and utilize the phenomenon of temperature increase with depth. The utilization of this resource involves collecting geothermal heat from the subsurface and transforming it into power using turbines.

To extract geothermal energy, a fluid is circulated through the deep subsurface layers. This fluid could come from a naturally occurring limited aquifer, water pumped into impermeable hot rock formations, or cycled through specially drilled wells. In all circumstances, the fluid absorbs heat before returning to the surface at a higher temperature. [7], [8]

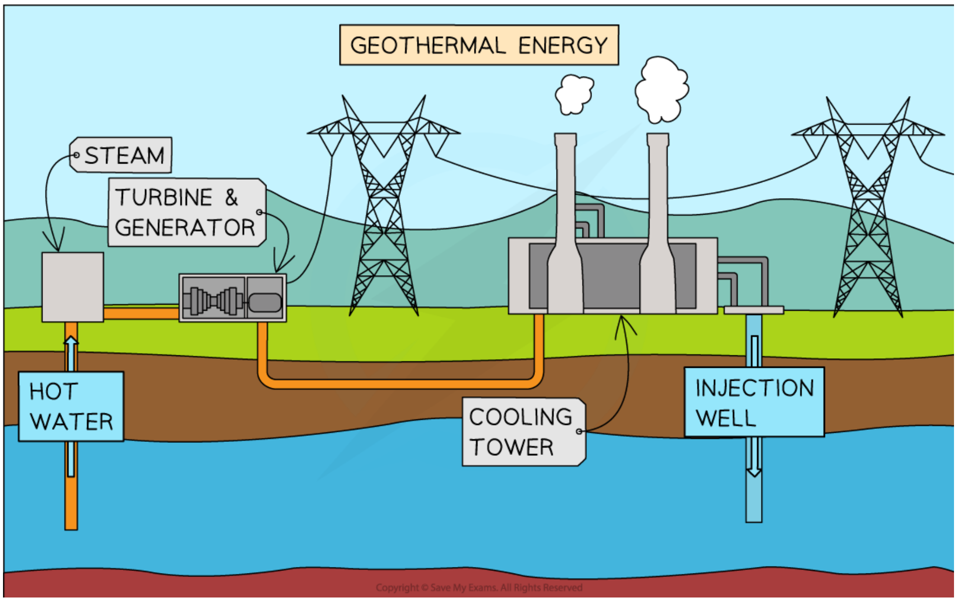

Figure 3: Geothermal Energy [9]

Geothermal energy has the advantage of being ecologically friendly and weather-independent, making it a consistent and dependable source of energy over time. However, it does present certain obstacles, such as the necessity for deep drilling, which might provide unclear findings, and the comparatively long development period required for installation, which can extend up to a quarter of a century.

2.4 Wind energy

The wind power generation system harvests the kinetic energy of the wind flow, converts it into electrical energy, and finally feeds it into the grid.

Figure 4 depicts a simplified configuration of the wind turbine system (WTS), which includes the wind turbine, gearbox, generator, power converter, and transformer.

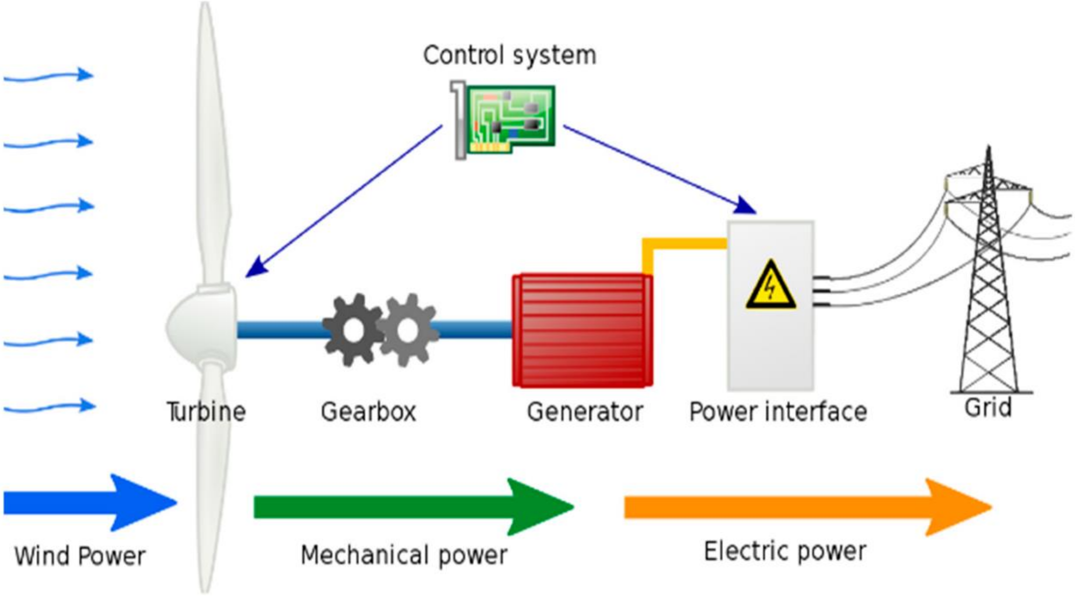

Figure 4 : configuration of the wind turbine system

Wind Turbine: The wind turbine collects kinetic energy from the wind and converts it into mechanical energy on the turbine's shaft. Early wind turbines typically operated at a nearly constant speed, whereas today's wind turbines can modify their rotational speed in response to changes in wind speed, thereby enhancing the efficiency of wind energy capture .[10]

Gearbox: The gearbox functions to modify the rotational speed of the shaft, ensuring compatibility with the generator. In certain instances, such as in directly driven wind power systems utilizing multiple-pole synchronous generators, the gearbox may be eliminated.

Generator: The generator converts the mechanical energy on the shaft into electrical energy. The generator in various WTS types might be either a permanent magnet synchronous generator (PMSG), a caged generator (CG), or a doubly fed induction generator (DFIG).

Power converters: The power converter functions as an interface between the generator and the power grid. It converts the original electrical energy from the generator, which may be unstable with regard to amplitude or frequency, into the relatively stable electrical energy, which is more accepted by the power grid. However, in order to increase the effectiveness of energy harvesting, the power converter also regulates the generator to work with the wind turbine. [11]

Transformer: This device feeds wind energy into distribution or transmission power lines by raising the power converter's output voltage.

2.4.1 Types of Wind Turbines

- **Horizontal-Axis Wind Turbines (HAWT)**

Horizontal-axis wind turbines (HAWTs) are characterized by a rotor shaft that is parallel to the ground. These turbines can be classified based on several design features: the rotor's position relative to the tower (upwind or downwind), the hub design (rigid or teetering), rotor control mechanisms (pitch or stall control), the number of blades (typically two or three), and their method of wind alignment (passive yaw or active yaw systems). HAWTs are currently the most widely used type of wind turbine, primarily due to their efficiency in large-scale wind farms. However, despite their advantages, they typically have an operational lifespan of around 15 to 20 years.[12]

Figure 5 : Horizontal Axis Wind Turbine (HAWT)

- **Vertical-Axis Wind Turbines (VAWT)**

Vertical-axis wind turbines (VAWTs), as their name suggests, have a rotor shaft that is perpendicular to the ground. This configuration allows the turbine to capture wind from any direction without reorientation. VAWTs are mainly divided into two types:

Darrieus turbines, which feature vertically oriented blades that revolve around a central shaft. These turbines are typically more efficient but require an external mechanism or manual push to initiate rotation.

Savonius turbines, known for their simple, scoop-like blades. These turbines operate at lower speeds and are capable of generating high torque, making them ideal for small-scale applications where reliability is prioritized over efficiency.

Figure 6 : Vertical-Axis Wind Turbines (VAWT)

2.4.2 Overview of Wind Power Systems (WPS)

An overview of wind power systems (WPS) is illustrated in Figure 7. Broadly, wind turbines operate under two main concepts: fixed-speed and variable-speed configurations.

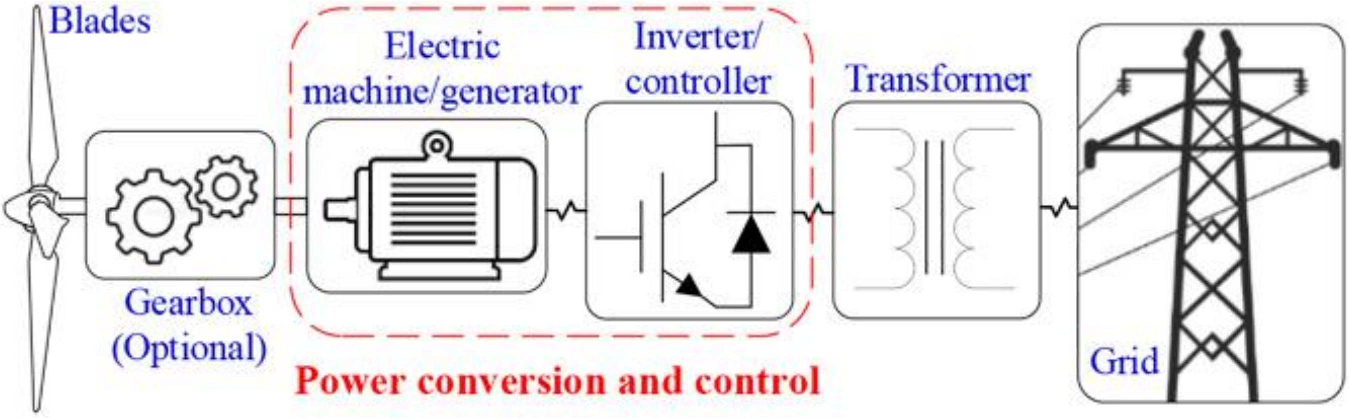

Figure 7 : configuration of a wind power generation system

- ### Fixed-Speed Wind Turbines

Historically, the earliest wind turbines were designed to operate at a constant rotational speed, a configuration commonly referred to as the fixed-speed concept. This setup, exemplified by the well-known "Danish concept," involves directly connecting a squirrel cage induction generator (SCIG) to the grid via a transformer. As shown in Figure 8, this system is valued for its structural simplicity, low cost, and reliability. Additionally, it does not require synchronization devices.[13], [14]

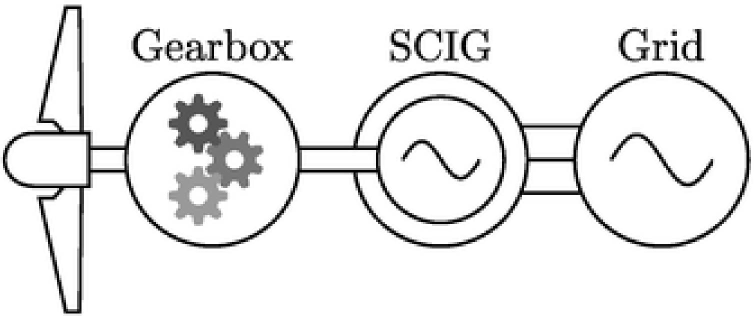

Figure 8 : Fixed speed of a wind turbine using a SCIG [15]

However, fixed-speed turbines have several limitations. They demand a relatively rigid power grid to maintain stability and are more susceptible to mechanical stress due to wind gusts, which can lead to torque fluctuations in the drive train. Furthermore, these turbines typically exhibit lower efficiency in converting wind energy, as they cannot adjust their speed in response to changing wind conditions. To improve performance, enhancements such as capacitor banks for reactive power compensation and soft starters for smoother grid integration were introduced in the 1980s.

- ### Variable-Speed Wind Turbines with Partial Power Converters

In contrast, variable-speed wind turbines offer a more dynamic and efficient approach. These systems adjust their rotational speed according to wind conditions, thereby optimizing energy capture. The ability to modulate speed reduces mechanical stress on critical components such as the tower, gearbox, and drivetrain, ultimately extending system longevity and reducing maintenance needs.

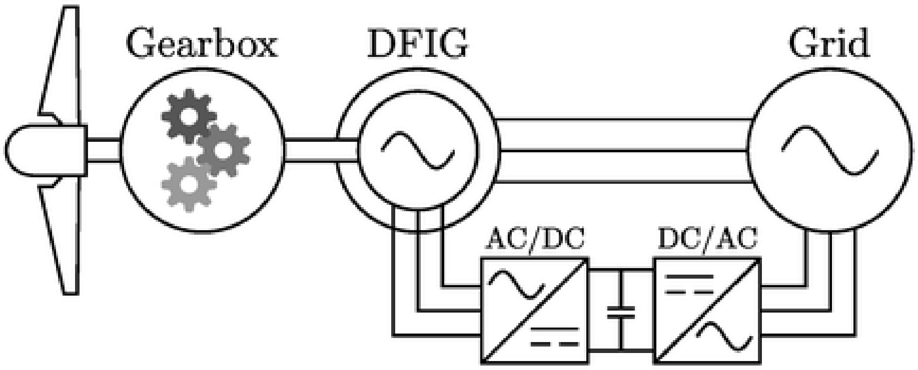

Figure 9 : variable speed of a wind turbine with a DFIG [15]

Among variable-speed systems, the Doubly-Fed Induction Generator (DFIG) configuration is the most widely adopted today, as illustrated in Figure 9. In this arrangement, the stator is directly connected to the grid, while the rotor is interfaced through a partial-scale power electronic converter. This converter consists of two components: the rotor-side converter (RSC) and the grid-side converter (GSC). The RSC controls the rotor current, enabling precise regulation of power output, torque, and rotor speed. Because the converter handles only a fraction—typically around 30%—of the generator's rated power, this design is both cost-effective and energy efficient.

Despite its benefits, the DFIG system has some drawbacks. It is more sensitive to grid voltage disturbances, such as faults, harmonic distortions, and imbalances. Nevertheless, advancements in control strategies and converter technologies are progressively improving the fault ride-through capabilities and overall resilience of variable-speed systems.

In summary, while fixed-speed wind turbines are cost-effective and straightforward, variable-speed systems offer enhanced efficiency, better grid compatibility, and reduced mechanical wear—key advantages that make them the preferred choice in modern wind energy applications.

- **Variable-Speed Concept with Full-Scale Power Converters**

The variable-speed concept with full-scale power converters represents a modern and efficient approach to wind energy conversion. In this configuration, the generator is fully decoupled from the electrical grid using a full-scale power electronic converter, which enables complete control over the generator's operation. This decoupling allows the generator to operate at variable speeds, thereby optimizing energy extraction under varying wind conditions and improving overall system efficiency.

One of the most commonly used configurations within this concept is the **Permanent Magnet Synchronous Generator (PMSG)** system, illustrated in Figure 10. The rotor of the PMSG is equipped with permanent magnets, eliminating the need for magnetizing current and slip rings. This design not only reduces energy losses but also simplifies the structure and lowers maintenance costs. The stator is controlled by a generator-side converter (GSC), while the generated power is transmitted to the grid via a line-side converter (LSC).

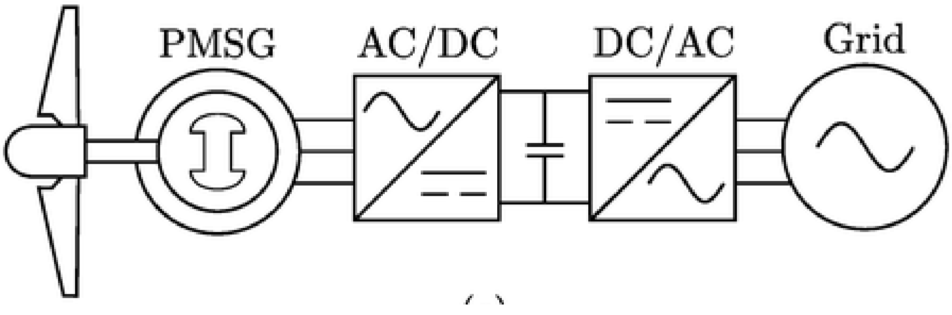

Figure 10 : variable speed direct-drive of a wind turbine with a PMSG [15]

Because the generator is electrically isolated from the grid, the system exhibits greater resilience to voltage disturbances and fluctuations—an advantage over Doubly-Fed Induction Generator (DFIG) systems. Moreover, the elimination of slip rings, and in some cases even the gearbox, enhances mechanical reliability and reduces maintenance requirements, making this architecture particularly attractive for offshore or remote installations.[16]

However, the main limitation of this approach lies in the higher cost of the full-scale power converters compared to the partial-scale alternative. To mitigate this, other generator types such as Squirrel Cage Induction Generators (SCIGs) or Wound Rotor Synchronous Generators may be used in conjunction with full converters to reduce the overall system cost while maintaining performance.[17]

2.5 Photovoltaic System

Solar energy stands as the most abundant and widely accessible source of renewable energy, capable of being harnessed even under cloudy conditions. The amount of solar radiation reaching the Earth is approximately 10,000 times greater than the total global energy consumption, underscoring its immense potential.

Solar technologies convert sunlight into electrical energy through two primary methods: **photovoltaic (PV) systems**, which directly transform sunlight into electricity using semiconductor materials, and **concentrated solar power (CSP) systems**, which employ mirrors or lenses to focus solar radiation and generate heat that is then converted into electricity.

Over the past decade, the cost of producing solar panels has declined significantly, making solar energy one of the most cost-effective sources of electricity available today. Modern solar panels typically have a lifespan of about 30 years and are manufactured in various shades and appearances, depending on the materials and technologies employed in their production

2.5.1 photovoltaic effect

The photovoltaic effect refers to the physical process through which a photovoltaic (PV) cell generates an electric voltage or current when exposed to sunlight. A typical solar cell is composed of two layers of semiconductor materials—p-type and n-type—that are joined together to form a p–n junction, as illustrated in Figure 11.[18]

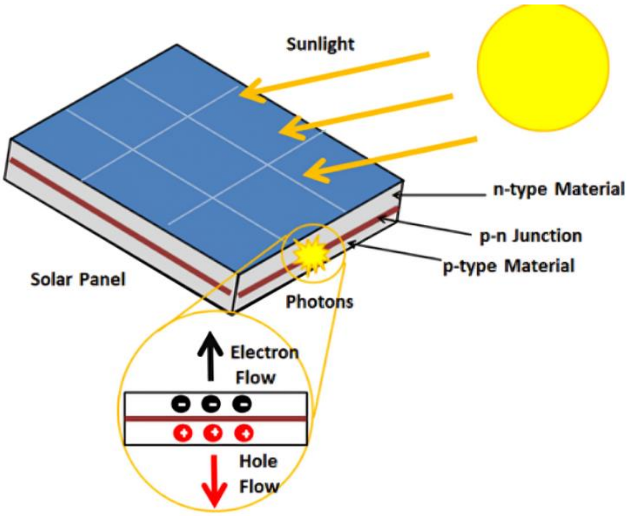

Figure 11 : The photovoltaic effect

When these two semiconductor layers are combined, an electric field is established across the junction due to the movement of charge carriers: electrons migrate toward the positively charged p-type region, while holes move toward the negatively charged n-type region. This internal electric field drives negatively charged electrons and positively charged holes in opposite directions, creating the potential difference required for current flow.

Sunlight is composed of photons, which are discrete packets of electromagnetic energy. When photons with sufficient energy strike the semiconductor surface, their energy is absorbed by electrons in the material. This excitation enables the electrons to transition from the valence band to the conduction band, freeing them to move through the material and thus generating an electric current within the photovoltaic cell.[19], [20]

2.5.2 Photovoltaic cells

A photovoltaic (PV) cell is an energy conversion device that transforms sunlight into electrical energy through the photovoltaic effect. Various types of PV cells exist, all of which rely on semiconductor materials to absorb photons from sunlight and convert their energy into the movement of electric charges, thereby generating an electric current.

- **Types of Photovoltaic Cells**

Photovoltaic (PV) cells are typically composed of semiconductor materials such as silicon (Si), germanium (Ge), selenium (Se), cadmium sulfide (CdS), cadmium telluride (CdTe), or gallium arsenide (GaAs). Among these, silicon remains the most widely used material due to its abundance and natural availability.

There are several main types of silicon-based PV cells:

- Monocrystalline silicon cells — characterized by their bluish-gray or black uniform appearance, these cells offer high efficiency ranging from 13% to 17% , Figure 12.

Figure 12 : Monocrystalline silicon cells

- Polycrystalline silicon cells — recognized by their blue, mosaic-like texture, they typically achieve an efficiency of 11% to 15%, Figure 13.

Figure 13 : Polycrystalline silicon cells

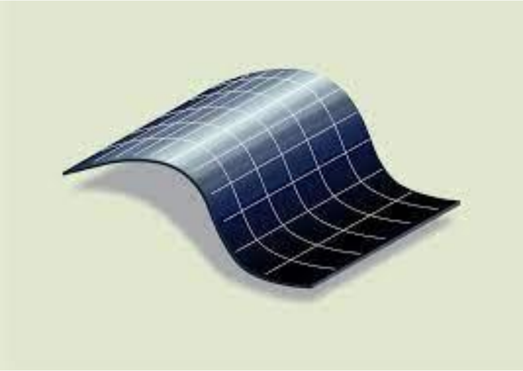

Figure 14 : Thin-film solar cells

- Thin-film solar cells (TFSC) — composed of thin layers of photovoltaic material, they are 6% to 10% efficient, making them a cost-effective but less efficient alternative, Figure 14.

2.5.3 Photovoltaic modules

Solar panels, sometimes called photovoltaic modules, are a web that collects solar radiation and turns it into clean energy. solar modules are composed of several separate, linked solar cells. Support structures contain the modules, ensuring that they are suitably inclined and face the sun. Each module has two output terminals that gather produced current and convey it to a solar power station's management systems.

• Association of Photovoltaic Cells

To generate greater electrical power, individual solar cells can be interconnected—either in series or in parallel—to form a photovoltaic module. This configuration allows for increased voltage or current, depending on the desired electrical output.

- Series Connection

The voltage output of a single photovoltaic (PV) cell is limited by the semiconductor’s bandgap potential. To increase the overall output voltage, multiple cells are connected in series. In this configuration, the same current flows through all cells, and the total voltage of the generator is proportional to the number of cells connected in series.

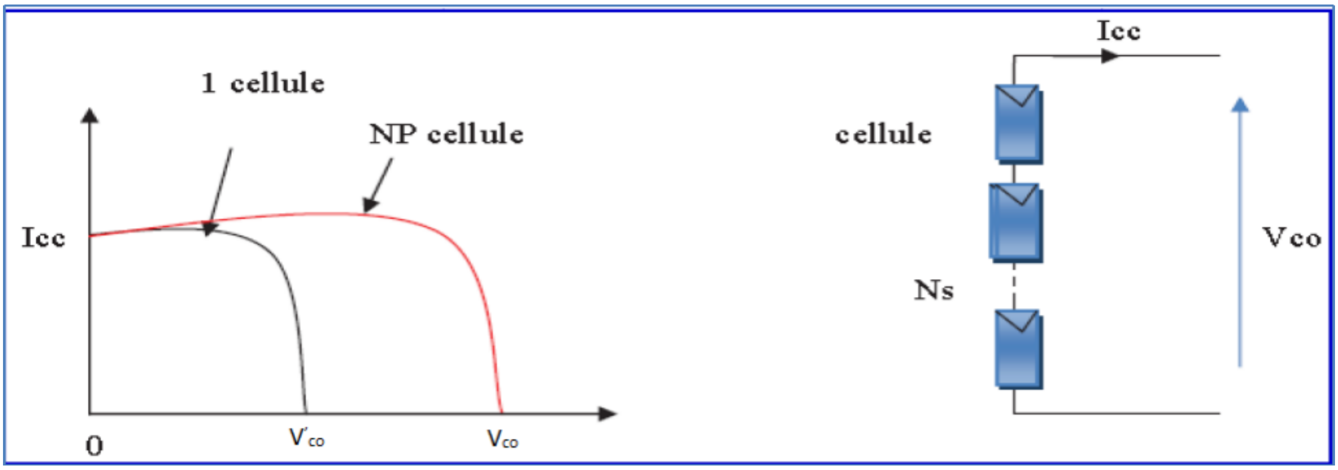

Figure 15 : Association of photovoltaic cells in series

Mathematically, this relationship can be expressed as:

$$V_{co} = N_s \times V'_{co} \quad ; V'_{co} \approx 0{,}5 \text{ à } 0{,}6 \text{ (V)}$$

$$I_{sc} = \text{cst}; \qquad (1)$$

Where:

Vco : Open-circuit voltage across Ns cells in series

V'co : Open-circuit voltage of a single cell

Isc : Short-circuit current through Ns cells in series

Ns : Number of cells connected in series

- Parallel Connection

When cells are connected in parallel, it is essential to ensure that their voltage levels are identical. In this configuration, the total current produced corresponds to the sum of the individual cell currents, while the voltage remains constant.

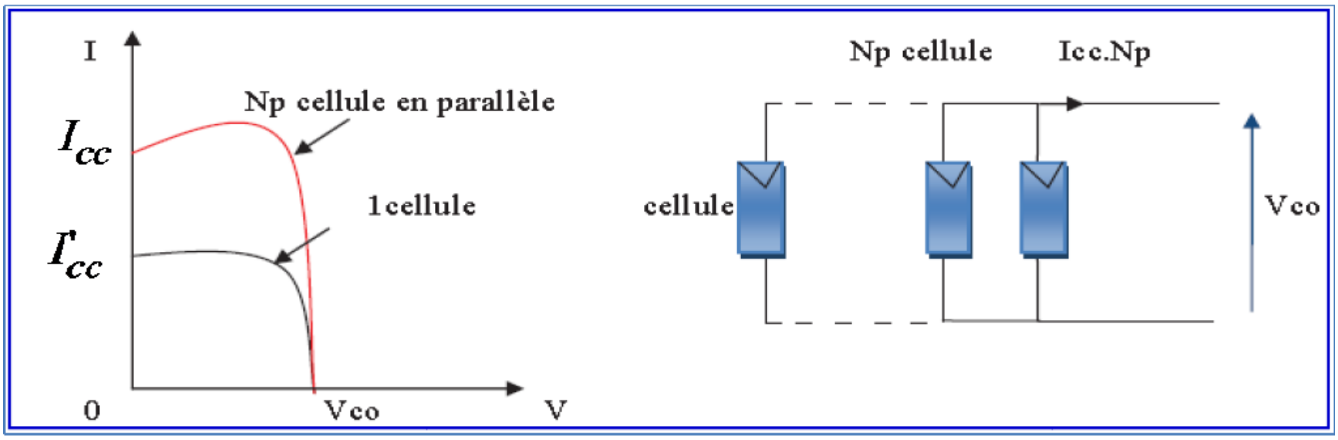

Figure 16 : Association of photovoltaic cells in parallel

This relationship is given by:

$$I_{cc} = N_p \times I'_{cc}$$
$$V_{co} = \mathrm{cst} \qquad (2)$$

Where:

Icc: Total short-circuit current for Np cells in parallel

Voc: Voltage across Np cells in parallel

Np: Number of cells connected in parallel

- Series–Parallel (Mixed) Configuration

To increase the overall power **output** of photovoltaic generators, cells are often arranged in a **combination of series and parallel connections**. This mixed configuration enables both higher voltage and current, forming an equivalent generator optimized for the desired energy production.

2.5.4 Fault Detection and Diagnosis in Photovoltaic Systems

- **Introduction**

The rapid expansion of the global photovoltaic (PV) market has led to an increased focus on the operational reliability and safety of PV systems. PV installations are continuously exposed to diverse external operating conditions, subjecting their components—including modules, cabling, protection devices, converters, and inverters—to various failure modes. If these faults are not swiftly detected and corrected, they can severely compromise the efficiency, energy yield, and overall reliability of the entire PV plant. Furthermore, the persistence of certain severe electrical faults, such as arc faults (AF) and line-to-line faults (LLF), can result in catastrophic fire hazards. Consequently, the integration of robust monitoring and Fault Detection and Diagnosis (FDD) systems is an indispensable requirement to guarantee the reliable, safe, and efficient operation of PV plants.

- **Classification of PV System Faults**

To design an effective diagnostic algorithm, it is critical to understand the nature and origin of the anomalies. Faults occurring within PV modules (PVM) and arrays (PVA) are generally classified into two main categories: permanent and temporary faults. Permanent faults involve irreversible physical damage, such as delamination, bubbles, yellowing of cells, scratches, and burnt cells, which necessitate the physical replacement of the affected module. These module defects are visually summarized in Figure 17 of the literature, which highlights physical damage like broken glass, oxidation, discoloration, delamination, and bubbles. In contrast, temporary faults are largely induced by environmental factors like partial shading effects, dust accumulation (soiling), dirt on the PVM, and snow, which can often be resolved without replacing the module.

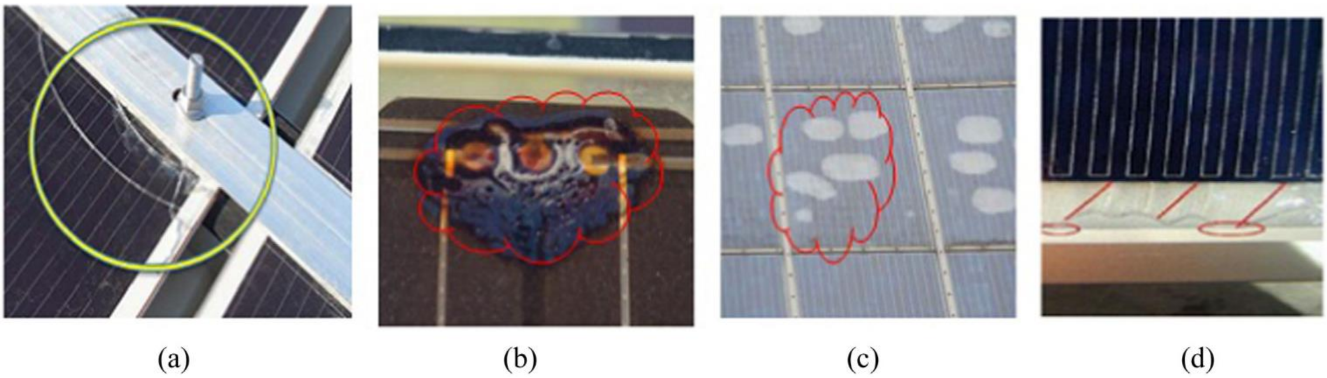

Figure 17 :Module defects: a) broken glass, b) oxidation and discoloration, c) delamination and d) bubbles.

The most critical faults occurring on the DC side of a PV system include:

- Hot Spot (HS) Faults:

HS faults can be caused when some cells in a PV string have different I-V characteristics, which can be triggered by external conditions like soiling and dust accumulation (as shown in Figure 18a and Figure 18b). When the bypass diode of shaded cells is damaged, the shaded cells consume power from non-shaded cells instead of generating it, leading to extreme localized heating and cellular damage (Figure 18c and Figure 18d).

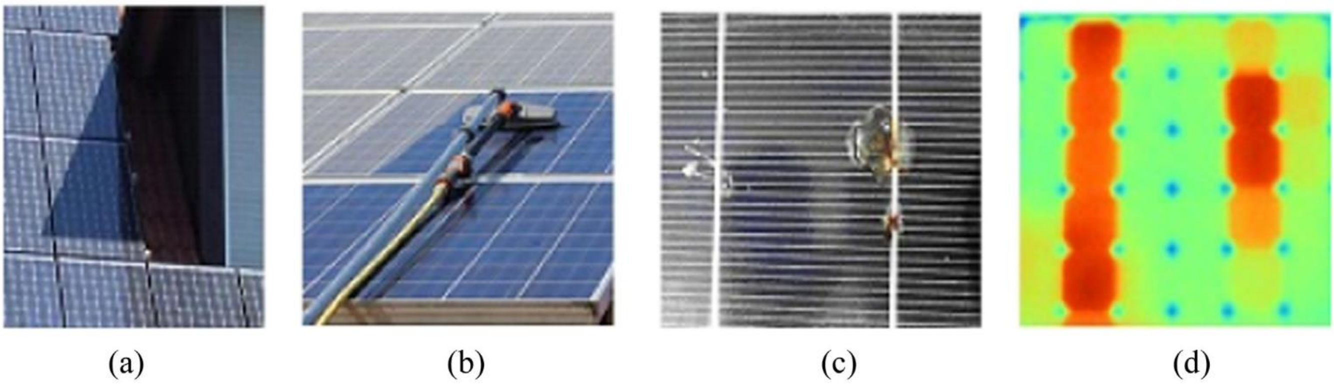

Figure 18 : HS fault: causes (a) shading, (b) soiling and dust accumulation; (c) HS damaged on solar cells; (d) detected HS phenomena on a PVM using infrared equipment

- Diodes and Junction Box Faults:

Bypass diodes (BpD) and blocking diodes (BkD) are essential for reverse voltage and reverse current protection, respectively. Prolonged shading can cause these diodes to short-circuit or open-circuit. Additionally, fretting corrosion within the junction box can escalate contact resistance, causing electric arcs, melting, and eventually destroying the module.

➢ Ground Faults (GF) and Line-to-Line Faults (LLF):

A ground fault is an accidental short circuit involving the ground and a current-carrying conductor, often due to insulation failure. Similarly, LLFs occur when two points of different potential accidentally connect due to mechanical damage or aging insulation. Both GF and LLF are highly dangerous as they generate DC arcs that sustain fire hazards.

- **Fault Detection and Diagnosis Methods**

The primary task of Fault Detection is to compare measured parameters against calculated reference values to determine if a fault has occurred. Subsequently, Fault Diagnosis (FDi) is employed to identify the exact type and location of the fault. FDD methodologies are broadly categorized into visual/thermal methods and electrical methods. While thermal methods (like infrared thermography) are highly effective for detecting physical defects like hotspots and delamination, they are often limited to small-scale systems. Electrical methods, which rely on system models and electrical parameter measurements, are far more versatile and are grouped into the following categories:

➢ Statistical and Signal Processing Approaches (SSPA)

Signal processing methods primarily rely on waveform analysis. Techniques such as Time Domain Reflectometry (TDR) and Earth Capacitance Measurement (ECM) have been utilized to detect and localize disconnections or degradation between modules within a PV string. For identifying Arc Faults (AF), spectral analysis techniques like the Fast Fourier Transform (FFT) and Wavelet Transform (WT) are widely applied to extract diagnostic frequency components. Furthermore, statistical techniques, such as the Analysis of Variance (ANOVA) and the exponentially weighted moving average (EWMA), are utilized to isolate short-circuits and shading phenomena from operational noise.

- I-V Characteristic and Power Losses Analysis

Anomalies physically alter the output curves of the PV system. Fault diagnosis can thus be achieved by analyzing the structural anomalies of the I-V characteristic curve, evaluating its first and second derivatives, or applying Kalman filters to adjust the I-V relationship dynamically. Alternatively, Power Losses Analysis (PLA) continuously compares the actual measured power against a theoretical simulated model. While PLA provides a highly cost-efficient detection metric by raising a fault flag when discrepancy thresholds (e.g., >5%) are exceeded, it generally lacks the capability to isolate the fault's exact location or type.

- Artificial Intelligence Techniques (AIT) and Intelligent Diagnosis

To overcome the limitations of traditional analytical models, modern FDD research has heavily shifted toward Artificial Intelligence (AI) and Machine Learning techniques. These methods excel at identifying complex, non-linear relationships hidden within massive electrical datasets.

Fuzzy Logic (FL) and Expert Systems: FL classifiers are utilized to evaluate diagnostic rules based on I-V measurements, demonstrating high accuracy in detecting partial shadows, Potential Induced Degradation (PID), and increased series-resistance losses.

Machine Learning Algorithms: Hybrid methodologies combining Support Vector Machines (SVM) with k-Nearest Neighbor (k-NN) algorithms have been deployed to detect and localize short-circuits and diode faults with remarkably low error rates.

Artificial Neural Networks (ANN): ANNs, frequently optimized via metaheuristics like Genetic Algorithms (GA) or Particle Swarm Optimization, offer robust dynamic repair and diagnosis capabilities for open-circuit and module degradation faults. Neural networks are highly effective in extracting the intrinsic parameters of the PV array without relying on rigid mathematical models.

3

Introduction to Wind Turbines Failures and Diagnosis Techniques

3.1 Introduction

Industrial systems are the bedrock of current technical and economic progress, ensuring dependability, safety, environmental sustainability, and cost effectiveness across all industries. One of the most difficult tasks in industrial engineering is to keep these systems performing optimally and lasting as long as possible while managing operational expenses throughout their lifespan.

To meet these problems, maintenance has shifted from a reactive response to equipment breakdowns to a purposeful and proactive practice. Maintenance can be divided into four categories: corrective, preventive, predictive, and condition-based maintenance, each with its own goals and approaches. The integration of monitoring technologies and intelligent diagnostic systems has resulted in a greater emphasis on reliability, cost optimization, and system availability.

Wind turbines are unique among industrial assets that require sophisticated maintenance techniques due to their structural complexity and sensitivity to changeable environmental conditions. Wind turbines are made up of multiple crucial components, including blades, gearboxes, bearings, and generators, which are susceptible to mechanical and electrical failures. These failures not only diminish energy production efficiency, but they can also cause costly downtime and equipment damage if not discovered promptly.[21]

To reduce these risks, contemporary maintenance frameworks include advanced problem diagnosis and condition monitoring techniques. Signal-based methods evaluate vibration, acoustic, or electrical signals to discover anomalies, whereas data-driven alternatives use artificial intelligence and machine learning to forecast failures from massive amounts of operational data. Together, these techniques provide accurate failure detection, classification, and prognosis, increasing wind turbine system reliability and extending service life.[22]

This chapter will therefore provide an overview of maintenance principles and categories, followed by a full examination of wind turbine failure modes and the diagnostic procedures used to monitor and assure their reliable functioning.

3.2 Common Failures in Wind Energy Systems

Wind turbines operate under highly variable and often extreme conditions, which can push their various components beyond their design limits. To develop effective predictive maintenance strategies, it is crucial to analyze failure statistics based on two key criteria: their frequency of occurrence and the downtime they cause. This analysis helps prioritize which failures require the most attention. However, obtaining such detailed statistics can be challenging, as manufacturers often restrict access to this sensitive data.

Studies of real-world failure data have identified the main components of a wind turbine system that are most prone to failure. When comparing the distribution of failures and associated downtime across these components, it becomes clear that the majority of failures are linked to the electrical system, various sensors, the blade pitch system, and the control system, respectively. However, in terms of total downtime, the control system and the gearbox have the most significant impact Figure 19.[23], [24], [25]

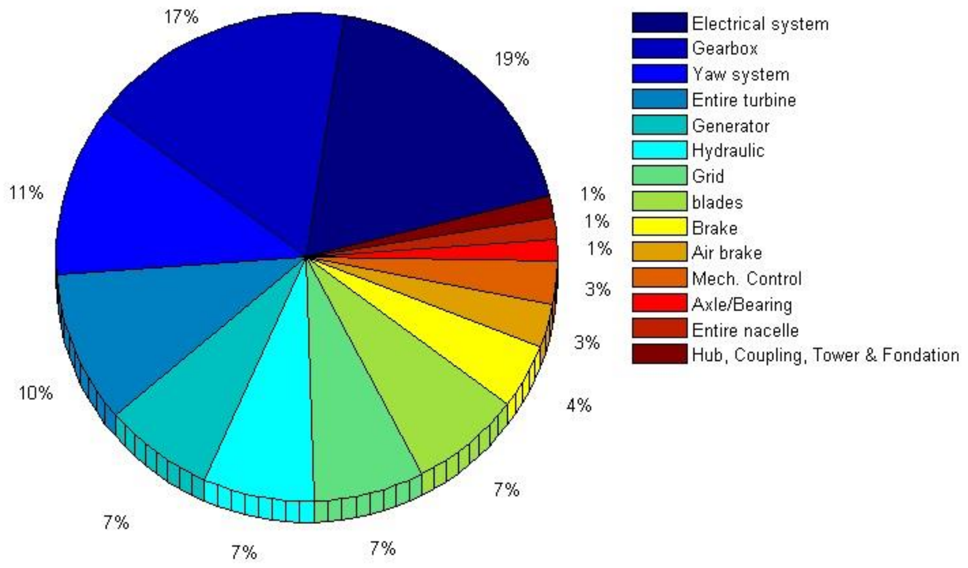

Figure 19 : component failure rates of wind turbines [26]

A separate study conducted on wind systems in Sweden and Germany between 1994 and 2004 corroborates this trend. In Germany, the highest failure rates were observed in the electrical control system and related electrical assemblies (such as the grid connection, yaw system, and blade pitch mechanism) rather than in purely mechanical components like the gearbox.[27]

The number of failures relative to the turbine's operational years is another critical factor in failure analysis. Data shows that the number of failures is relatively low during the initial years of operation but increases significantly after the first two years. The failure rate then stabilizes around the eighth year before dropping again in the eleventh year. A notable peak occurs in the twelfth year, after which the rate gradually declines through the nineteenth year.[28], [29]

While the gearbox is often considered the most critical component in indirectly driven wind turbines, it might be assumed that direct-drive applications have fewer failures. However, studies indicate that direct-drive wind turbines do not necessarily experience fewer failures than their indirect-drive counterparts. Research into the reliability of generators and power converters in wind energy systems reveals the following:

- Power converter failures in direct-drive applications are more common than in indirect-drive systems, though they are still less frequent than gearbox failures in indirect-drive turbines.

- The failure rate of the electrical system in direct-drive turbines is significant. When considering all electrical connection faults, their collective failure rate can be higher than that of gearboxes in indirect-drive systems.
- The failure rates of generators in direct-drive applications are approximately twice as high as those in indirect-drive systems.

3.2.1 Electrical Control System Failures

Common failures in the electrical control system include deterioration of generator windings, transformers, and wiring, as well as short circuits and voltage surges in electronic components. These issues can be triggered by several factors, including lightning strikes, improper electrical installations, technical defects, and resonance within Resistor-Capacitor (RC) circuits.[30]

3.2.2 Yaw System Failures

The yaw system controls the orientation of the nacelle to face the wind. Reported failures in this system include cracks in the drive shafts, fractured gear teeth, pitting in the hub bearing race, and failures of bearing fastening screws. Major causes of these failures are icing in extreme weather conditions and high vibration levels due to overloading.[31]

3.2.3 Grid Connection Failures

The wind is inherently variable in both direction and intensity, making it difficult to predict with precision. Without backup energy storage or an alternative power generation system, grid failures can occur during periods of high-power consumption coupled with low wind energy production.

3.2.4 Hydraulic System Failures

Hydraulic components are used in numerous high-pressure connections within a wind turbine, including the pitch system, the nacelle yaw system, the braking system, and the gearbox lubrication system. Leaks in these components are classified as hydraulic failures. Since wind turbines are typically located in harsh environments—subject to extreme temperatures, corrosion, and vibration—failures can arise from poor installation, flawed system design, low-quality components, or system misuse. Poor installation is estimated to be the root cause in up to 60% of hydraulic failures. Failures caused by faulty sensors or non-hydraulic events are often the most complex to diagnose and resolve, as troubleshooting procedures can be confusing and lead to situations not anticipated by the manufacturer.

3.2.5 Blade Failures

The blades are the primary components of the wind turbine rotor, responsible for transferring the wind's kinetic energy into mechanical energy on the drive shaft. They are typically made of composite materials, which can sometimes conceal minor defects or malfunctions that are difficult to detect with conventional methods. Furthermore, blades are constantly exposed to extreme natural phenomena like wind turbulence and lightning strikes. These can cause material defects and trigger the overspeed protection system, leading to catastrophic failures such as deterioration, cracks, bending, or even the loss of part or all of a blade. Such events endanger human safety and can undermine public confidence in wind energy. For instance, it has been reported that a broken blade was thrown more than 1.3 kilometers from its tower. Consequently, many countries have implemented regulations prohibiting public access near wind farms.

Most modern wind turbines are equipped with lightning protection systems connected to the turbine's control and monitoring system. However, complete protection against lightning damage is not always feasible. As a result, research is ongoing into methods for locating and classifying lightning impacts and monitoring blade health using networks of optical fiber sensors.[27]

3.2.6 Failures in Electrical Generators

Advances in engineering and material science have led to the development of lighter and more durable electrical machines. Despite these improvements in design techniques, faults can still occur. In low- and medium-power machines, the most common faults are stator-related. For high-power machines, failures due to mechanical stresses, particularly bearing failures, represent the highest percentage of faults Figure 20. [32]

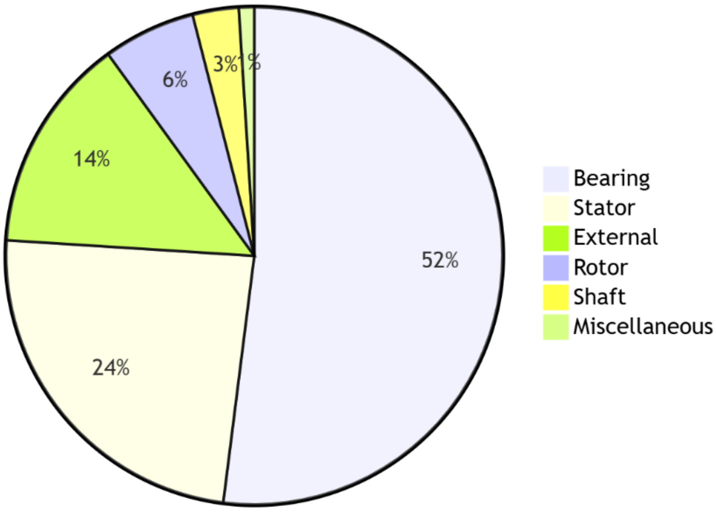

Figure 20 : Failure rates of electrical generator [33]

Main Mechanical Failures in Rotating Machinery:

Mechanical failures represent the most common class of faults in rotating systems. They often manifest as excessive vibration, noise, or loss of performance, and can propagate to other components if not detected early.

1. Imbalance Faults

Imbalance is among the most frequent causes of vibration in rotating machines. It arises when the mass distribution of a rotor is uneven, displacing its center of gravity away from the axis of rotation. This deviation generates centrifugal forces that induce vibration proportional to the rotational speed.

Imbalance can stem from several factors, including:

- Manufacturing or assembly errors,
- Material inconsistencies,
- Erosion, corrosion, or material accumulation on rotating elements,
- Thermal deformation of blades or fans,
- Uneven wear or displacement of parts under centrifugal stress.

Three main forms of imbalance can occur:

- Dynamic Imbalance
- Couple Imbalance
- Static Imbalance

2. Misalignment

Misalignment occurs when two connected rotating shafts are not properly aligned. This defect is one of the major sources of vibration and mechanical stress in rotating systems.

- Parallel Misalignment

Parallel misalignment occurs when the axes of the coupled shafts are parallel but displaced from each other. This defect induces alternating forces and vibrations along both the axial and radial directions.

Other common types include angular and mixed misalignment, each producing distinct vibrational patterns detectable through frequency analysis.

3. Gear Faults

Gears are widely used to transmit torque and motion between rotating shafts. Due to their cyclic loading, gear components are prone to faults such as pitting, cracking, spalling, or tooth breakage.

4. Bearing Faults

Bearings play a vital role in supporting rotating shafts and reducing friction between moving parts. Their failure can severely affect machine performance. Common bearing defects include wear, corrosion, cage damage, flaking, or cracking.

The outer race, inner race, cage, and rolling elements are the basic structural components of rolling element bearings. When a rolling element in a bearing passes over a localized defect—whether located on the **inner race**, **outer race**, or on the **rolling element** itself—a transient impact or shock is generated. Each impact excites a vibration that repeats periodically as the defect reappears in the same position relative to the rotating elements. The repetition rates of these impulses are referred to as **Bearing Characteristic Frequencies (BCFs)**.[34], [35]

The defect characteristic frequencies can be obtained [36] as follows:

Outer race frequency defect:

$$f_O = \frac{N_{ball}}{2} f_r \left(1 - \frac{D_{ball}}{D_{cage}} . \cos\theta \right) \quad (3)$$

Inner race frequency defect:

$$f_i = \frac{N_{ball}}{2} f_r \left(1 + \frac{D_{ball}}{D_{cage}} . \cos\theta \right) \quad (4)$$

Cage frequency defect:

$$f_c = \frac{f_r}{2}\left(1 - \frac{D_{ball}}{D_{cage}}\cos\theta\right) \qquad (5)$$

Rolling element (ball) frequency defect:

$$f_b = \frac{D_{cage}}{2D_{ball}} f_r\left(1 - \left(\frac{D_{ball}}{D_{cage}}\cos\theta\right)^2\right) \qquad (6)$$

Where D_{cage} and D_{ball} are cage (pitch) diameter and ball diameter respectively, θ is the contact angle of balls , N_{ball} is the number of the rolling element (ball), and f_r is the shaft rotational frequency.

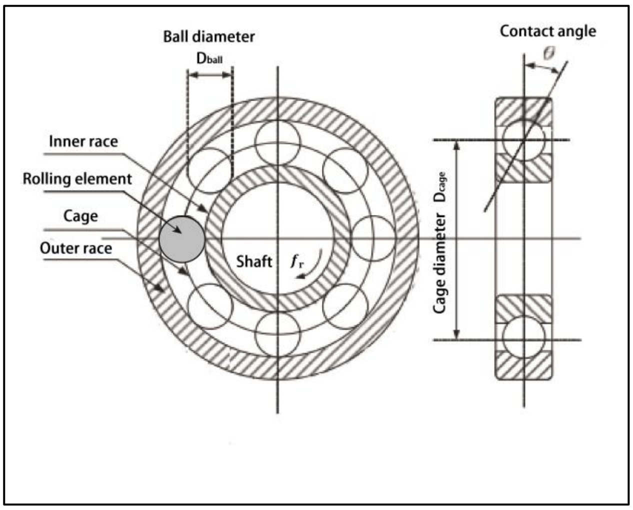

Figure 21 : Ball bearing components

5. Belt Faults

Belt drives transmit motion and power between pulleys. Faults in belts may include wear, cracking, or slippage.

Electrical Faults

In addition to mechanical issues, rotating machinery may also experience electrical faults, particularly in motors and generators. These can cause partial or complete operational failure.

1. **Rotor Faults**

   Rotor faults typically arise from broken bars, unbalanced windings, or air-gap irregularities. These faults lead to fluctuations in torque and current.

2. **Stator Faults**

   Stator failures are often caused by insulation degradation, phase imbalance, or overheating. Such faults generate harmonics in the electrical frequency spectrum, affecting efficiency and stability.

3.2.7 Gearbox Failures

Wind turbines typically operate in extremely harsh environments characterized by dust, humidity, temperature fluctuations, air pressure changes, and unpredictable loads from wind gusts. Consequently, wind turbine gearboxes are susceptible to severe tribological conditions, including wear, fatigue, and corrosion. These factors lead to increased component damage and machine malfunction. Surveys of wind farms in Europe and America consistently show that the gearbox is one of the least reliable subsystems and is a major contributor to turbine downtime and maintenance costs. [37]. The gearbox is subject to various wear mechanisms within the wind turbine system, such as abrasive wear, pitting, scuffing, erosion, cracking, and breakage.[38]

3.3 Definition of Maintenance

According to the standard **NF EN 13306**, maintenance is defined as “the combination of all technical, administrative, and managerial actions during the life cycle of an item intended to retain it in, or restore it to, a state in which it can perform the required function."

This definition underscores that maintenance is not limited to repairs but includes all systematic activities designed to ensure the continued performance, reliability, and availability of industrial assets throughout their operational lifespan.[39]

3.4 Types of Maintenance

Maintenance strategies can be broadly divided into two main categories: **reactive** and **proactive** maintenance. While reactive maintenance involves interventions after a failure occurs, proactive maintenance emphasizes prevention and prediction to minimize unplanned downtime and optimize system reliability.[40]

3.4.1 Reactive Maintenance

Reactive maintenance, often referred to as *unplanned* or *run-to-failure maintenance*, is a traditional approach that addresses maintenance issues only after they become evident—such as mechanical breakdowns, equipment stoppages, or defects.

This method is typically suited for facilities with limited machinery, where system reliability is not critical to overall production. It may also be justified when the probability and cost of failure are low or when failures pose no significant safety or environmental risks.

Reactive maintenance includes two main subcategories: **corrective maintenance** and **emergency maintenance**.

a. Corrective Maintenance

According to **NF EN 13306**, corrective maintenance consists of "actions carried out after fault recognition, intended to restore an item to a state in which it can

perform its required function.”
In this approach, maintenance is performed only after a fault or failure has occurred. While this method ensures rapid restoration of functionality, it often results in unscheduled downtime and potential production losses.

b. Emergency Maintenance

Emergency maintenance, also known as *breakdown maintenance*, is performed when immediate intervention is required to restore equipment operation. Although essential in critical situations, this type of maintenance is highly disruptive—it interrupts production processes, diverts technical staff from planned tasks, and can lead to delays in meeting operational schedules. The severity of its impact depends on factors such as the extent of the damage, repair duration, availability of spare parts, and the importance of the affected equipment.

3.4.2 Proactive Maintenance

Proactive maintenance, also referred to as *planned maintenance*, represents a more advanced and systematic approach. It encompasses all activities that are carefully planned, documented, and monitored to maintain equipment performance at acceptable levels.
Unlike reactive strategies, proactive maintenance focuses on anticipating failures before they occur by relying on historical data, performance monitoring, and statistical modeling. This approach not only enhances operational reliability but also improves cost-effectiveness and maintenance scheduling.
Proactive maintenance can be divided into two main categories: **preventive maintenance** and **predictive maintenance**.

a. Preventive Maintenance

Preventive maintenance is a scheduled, pre-planned approach aimed at avoiding equipment failure by performing maintenance tasks at predetermined intervals or under specific conditions. It is especially valuable in complex technological systems where unexpected failures can lead to significant downtime or safety hazards. The principle of preventive maintenance is to replace or service components before they fail, based on their expected life cycle or operational data. Maintenance tasks are thus scheduled during planned shutdowns or production pauses.

This approach includes several methodologies:

Constant Interval Maintenance – Maintenance operations are conducted at fixed time intervals. The interval duration is optimized to balance the cost of maintenance and the risk of potential failure.

Age-Based Maintenance – Maintenance is performed when the equipment reaches a predetermined operational age or usage threshold. If a failure occurs before this threshold, the next intervention is scheduled based on the new operating time.

Imperfect Maintenance – Recognizes that preventive actions may not always restore equipment to a “like-new” condition. Instead, maintenance returns the system to an intermediate state between full functionality and failure. This approach accounts for equipment uncertainty when scheduling future interventions.

b. Predictive Maintenance

Predictive maintenance (PdM) is an advanced, data-driven strategy that utilizes real-time monitoring, machine learning, and statistical modeling to predict equipment degradation and prevent potential failures before they occur. Unlike preventive maintenance, which operates on fixed schedules, predictive maintenance relies on continuous data analysis—such as vibration, temperature, and acoustic signals—to assess equipment health dynamically.[41], [42]

Predictive maintenance encompasses two major methodologies:

Condition-Based Maintenance (CBM):

This approach determines maintenance actions based on the actual condition of equipment. Parameters such as vibration, temperature, and oil quality are monitored continuously or periodically.[43] Maintenance is only performed when these indicators show signs of abnormality. This method allows maintenance to be predictive, evidence-based, and cost-efficient.[44]

Reliability-Centered Maintenance (RCM):

Initially developed for the aviation industry, RCM focuses on optimizing maintenance schedules based on system reliability and criticality. It prioritizes maintenance tasks that enhance safety, availability, and cost-effectiveness. The process begins by identifying all potential failure modes and categorizing them according to their impact on the system. The resulting analysis guides maintenance decisions, ensuring that resources are allocated efficiently to prevent critical failures.[45], [46]

3.5 Dependability

3.5.1 Definition

Dependability represents a system's ability to provide a service that can be *justifiably trusted*. This concept emphasizes the importance of ensuring that users can rely on the system's performance with confidence and that such trust is verifiable and well-founded .

From a quantitative perspective, dependability can be defined as the capability of a system to **avoid service failures** that occur more frequently or with greater severity than what is considered acceptable by its users. In other words, a dependable system consistently performs its intended functions while minimizing interruptions, malfunctions, or risks to acceptable levels.

3.5.2 Attributes

Over the past three decades, the notion of dependability has evolved into a **multidimensional concept** encompassing several key attributes that collectively define the trustworthiness of a system:

- **Availability** – the readiness of the system to deliver correct service when required.
- **Reliability** – the continuity and consistency of the system in delivering correct service over time.
- **Safety** – the assurance that the system operates without causing catastrophic consequences to users, equipment, or the environment.
- **Confidentiality** – the prevention of unauthorized disclosure of information.
- **Integrity** – the assurance that the system remains protected against improper or unauthorized modifications.
- **Maintainability** – the system's ability to undergo repairs, updates, or modifications efficiently and effectively.

In this context, **security** is viewed as the *concurrent existence* of availability (restricted to authorized users), confidentiality, and integrity—where "improper" denotes "unauthorized" actions.

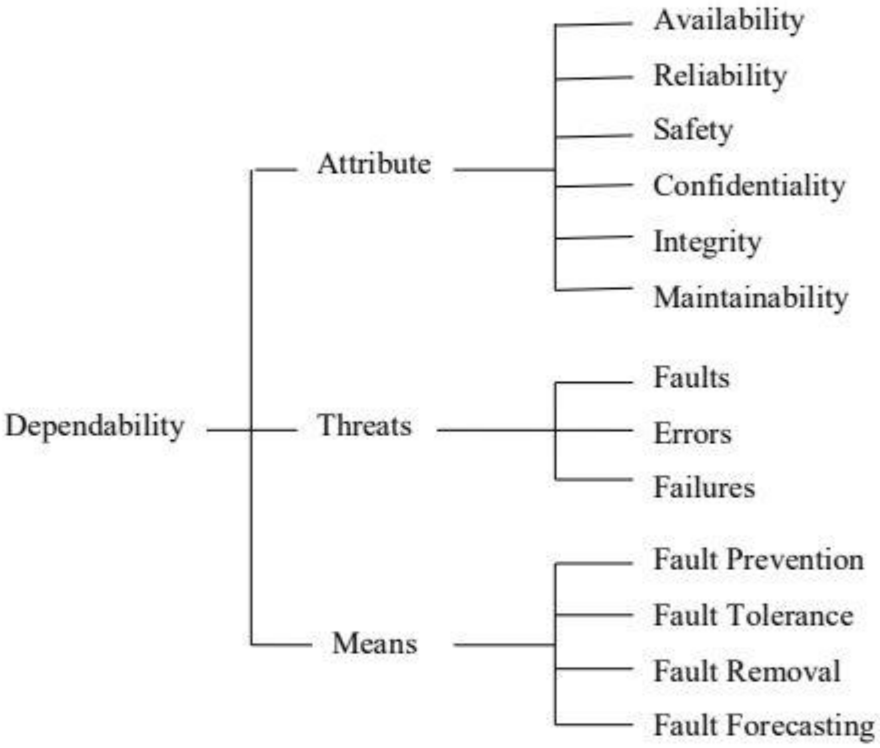

Figure 22 : Dependability tree [47]

The overall taxonomy of dependable computing, which organizes and relates these key attributes, is illustrated in Figure 22, providing a clear overview of the conceptual framework that underpins system dependability.

3.6 Fault Diagnosis Techniques

Fault diagnosis techniques for wind turbines can be broadly categorized into **model-based**, **signal-based**, **knowledge-based**, and **hybrid** approaches. Each method has distinct advantages depending on the type of fault, data availability, and computational resources.[48]

3.6.1 Model-Based Fault Diagnosis

Model-based techniques rely on the development of mathematical or physical models that describe the expected behavior of the system under normal operating conditions. By comparing the actual system response with the model's predictions, deviations—known as residuals—can be analyzed to identify and locate potential faults.[49]

These methods are highly effective for systems with well-defined dynamics and measurable parameters.[50], [51] However, their performance depends heavily on the accuracy of the model and can be limited in complex systems like wind turbines, where environmental disturbances and parameter variations are significant.[52], [53]

3.6.2 Signal-Based Fault Diagnosis

Signal-based methods focus on analyzing measurable signals—such as vibration, temperature, current, or acoustic emissions—to detect abnormal patterns indicative of faults. These approaches do not require a detailed physical model of the system, making them suitable for complex and nonlinear machinery like wind turbines.[48], [49], [54], [55]

Signal processing techniques such as **Fast Fourier Transform (FFT)** [56], [57], **Wavelet Transform (WT)** [58], [59], [60], and **Hilbert–Huang Transform (HHT)** [61], [62], [63] are commonly applied to extract meaningful features from raw sensor data. These features are then used to detect deviations from normal operation and to identify fault signatures.

One of the most prevalent and effective signal-based methods is **vibration analysis**, which provides valuable insight into the mechanical condition of rotating components. [64], [65]This technique will be presented in details later in this chapter.

3.6.3 Knowledge-Based Fault Diagnosis

Knowledge-based approaches depend on expert knowledge, historical data, and heuristic reasoning to identify and classify faults. They often employ methods such as **expert systems**, **fuzzy logic**, and **neural networks** to simulate human reasoning and decision-making processes.

These techniques are advantageous when physical models are unavailable or difficult to construct. However, their accuracy depends largely on the quality and completeness of the knowledge base, which must be continuously updated to adapt to new fault scenarios.

3.6.4 Hybrid Fault Diagnosis

Hybrid diagnostic systems combine the strengths of multiple approaches—such as model-based and data-driven methods—to enhance fault detection accuracy and robustness. For example, model-based residuals may be used to generate features for machine learning algorithms, leading to more reliable fault classification. [66]

This integrated approach leverages the complementary advantages of analytical modeling and empirical data analysis, making it particularly well-suited for complex and dynamic systems like wind turbines.[67]

3.7 Vibration Analysis

Even under normal operating conditions, wind turbines and other rotating machines inherently generate vibrations. Many of these vibrations are directly associated with periodic events occurring during machine operation, such as shaft rotation, gear meshing, and electromagnetic interactions within electric generators.[68]

Vibration analysis has become one of the most widely adopted techniques in preventive and predictive maintenance, particularly for detecting faults in rotating machinery. It provides valuable insight into the mechanical condition of components such as bearings, gears, couplings, and shafts. When mechanical defects such as bearing wear, looseness, imbalance, or misalignment occur, they alter the internal dynamic forces of the machine, resulting in measurable changes in vibration patterns.[69], [70]

According to the ISO 2041 standard, *"Vibrations and shocks – Vocabulary" (August 1990)*, vibration is defined as:

"A variation over time of the magnitude of a characteristic quantity of the motion or position of a mechanical system, when this magnitude alternates between values greater and smaller than a certain average or reference value."

In the context of fault diagnosis, vibration signals are analyzed in the time domain, frequency domain, or time–frequency domain to identify fault signatures and their evolution over time [68]. The amplitude, frequency, and phase of vibration components carry essential diagnostic information, allowing maintenance teams to detect early-stage failures and plan corrective actions before severe damage occurs.

Consequently, vibration analysis remains an indispensable tool in wind turbine condition monitoring, providing accurate, real-time indicators of mechanical health and supporting the transition from traditional reactive maintenance to proactive and predictive maintenance strategies.

3.7.1 Time domain analysis

Vibration signals collected from rotating machinery typically originate from multiple interacting sources, each contributing to a complex and often random vibration pattern. Because of this inherent randomness, these signals cannot be accurately represented by a single deterministic mathematical equation. Instead, they must be analyzed using statistical methods that describe their behavior over time.

Early research in vibration-based condition monitoring therefore focused heavily on time-domain statistical analysis, which remains one of the most fundamental approaches in fault diagnosis. This technique involves examining the raw vibration signal as a function of time and extracting numerical features—known as statistical indicators—that capture its amplitude, variability, and impulsiveness.[71], [72] These statistical features, derived directly from the time waveform, serve as essential tools for both manual inspection and automated fault detection. They provide a quantitative measure of the machine's condition, enabling maintenance teams to detect early signs of degradation or abnormal operation without the need for complex transformations or frequency-based models.[73]

The following sub-section presents a detailed overview of the main time-domain statistical functions commonly employed in vibration analysis. Each function provides unique insight into the signal's characteristics and helps identify changes that may indicate mechanical faults or performance deterioration.

- **Peak Amplitude**

The peak amplitude x_p corresponds to the maximum absolute value of the vibration signal. It can also be defined as half the difference between the signal's maximum and minimum amplitudes, as expressed as follows [74]:

$$x_p = \frac{1}{2}[x_{max}(t) - x_{min}(t)] \qquad (7)$$

- **Mean Amplitude**

The mean amplitude $\bar{x}$ represents the average value of the vibration signal over a sampling interval.[74] It is mathematically defined by:

$$\bar{x} = \frac{1}{T}\int x(t)\,dt \qquad (8)$$

For a discrete signal, it can be expressed as:

$$\bar{x} = \frac{1}{N}\sum_{i=1}^{N} x_i \qquad (9)$$

- **Root Mean Square (RMS) Amplitude**

The root mean square (RMS) amplitude x_{RMS} quantifies the quadratic mean of the vibration signal magnitude over a sampling period:

$$x_{RMS} = \sqrt{\frac{1}{T}\int |x(t)|^2 dt} \tag{10}$$

For discrete data:

$$x_{RMS} = \sqrt{\frac{1}{N}\sum_{i=1}^{N} |x_i|^2} \tag{11}$$

- **Skewness**

Skewness x_{SK} represents the third normalized central moment of the vibration signal and quantifies the degree of asymmetry in its probability distribution. It is expressed as:

$$x_{SK} = \frac{\sum_{i=1}^{N}(x_i - \bar{x})^3}{N\,\sigma_x^3} \tag{12}$$

- **Kurtosis**

Kurtosis x_{KURT} corresponds to the fourth normalized central moment of the vibration signal and characterizes the distribution's peak relative to its variance. [75]It is given by:

$$x_{KURT} = \frac{\sum_{i=1}^{N}(x_i - \bar{x})^4}{N\,\sigma_x^4} \tag{13}$$

- **Entropy**

Entropy x_{ENT} measures the uncertainty or randomness of the vibration signal's probability distribution. It is defined as:

$$x_{ENT} = \sum_{i=1}^{N} p_{x_i} \log p_{x_i} \tag{14}$$

where p_{xi} denotes the probability associated with each amplitude level.

3.7.2 Frequency domain analysis

Frequency-domain analysis, also known as spectral analysis, is among the most widely applied vibration analysis techniques used in machine condition monitoring [76]. This approach provides valuable insights into frequency characteristics that are often not evident in the time domain. The vibration signals measured in the time domain typically result from the combined motion of several machine components—such as bearings, shafts, and fans—where each component generates a sinusoidal waveform defined by a specific frequency and amplitude. In practice, the sensor records a superposition of all these individual vibrations rather than distinct frequency components. By transforming the time-domain waveform into its spectral representation, the resulting frequency spectrum allows clearer identification of each vibration source.[77]

As Known, rotating machinery produces different types of vibration signals—both random and periodic—under healthy and faulty operating conditions. Their frequency-domain representations are commonly obtained through Fourier analysis, which can be categorized into three main forms: the Fourier series, the continuous Fourier transform (CFT), and the discrete Fourier transform (DFT). The fundamental principle of Fourier analysis was established in the nineteenth century by the French mathematician J. Fourier, who demonstrated that any periodic function could be expressed as a summation of complex exponential functions. Among these, the DFT is particularly significant for analyzing discrete-time vibration signals .

3.7.3 Envelope Analysis

the vibration signals from faulty machinery are often amplitude-modulated, where characteristic fault frequencies are obscured by high-frequency resonances and background noise. To isolate these diagnostic features, demodulation analysis is employed. A prominent technique for this is envelope analysis, also known as high-frequency resonance analysis. This method is a powerful and dependable tool for the early detection of faults in rolling element bearings. The standard procedure involves three key steps: (1) band-pass filtering the raw vibration signal to isolate a resonant frequency band; (2) rectifying the signal, typically via the Hilbert-Huang Transform (HHT), to extract its amplitude envelope; and (3) applying a Fast Fourier Transform (FFT) to this envelope to produce an envelope spectrum [78], [79]. This final spectrum reveals distinct amplitude peaks at the fault frequencies, which are often imperceptible in a standard FFT of the raw signal.

3.7.4 Time-Frequency Analysis

As discussed in the previous chapter, the Fourier Transform provides a powerful means of converting a signal from the time domain to the frequency domain, revealing its spectral components. However, while this transformation captures the overall frequency content of a signal, it does not effectively convey how these frequency components evolve over time. The Fourier Transform inherently assumes that the signal is stationary, meaning that its frequency characteristics remain constant throughout its duration. In practice, this assumption often fails, particularly in rotating machinery, where vibration signals can vary significantly with changes in operating speed or load.

As Tiboni [76] noted, most vibration analyses of rotating machines involve speed sweeps, in which machines accelerate or decelerate across a range of revolutions per minute (RPM). Such variations produce nonstationary signals, whose frequency content continuously changes over time. Consequently, traditional frequency-domain techniques, though effective for stationary signals, are insufficient for accurately representing these time-dependent dynamics.

To address this limitation, time–frequency analysis techniques have been developed to jointly represent a signal in both the time and frequency domains. These methods provide a more comprehensive picture of a system’s dynamic behavior, making them particularly useful for analyzing nonstationary vibration signals generated by machinery faults. Over the years, numerous time–frequency analysis tools have been introduced and successfully applied to fault diagnosis, including the Short-Time Fourier Transform (STFT) [80], [81], Wavelet Transform (WT) [82], [83], Hilbert–Huang Transform (HHT) [84], [85], Empirical Mode Decomposition (EMD) [86], [87], [88], Variational Mode Decomposition (VMD) [89], [90] and Local Mean Decomposition (LMD), among others.

In this chapter, attention will be devoted to the time–frequency domain analysis of vibration signals, emphasizing data-driven decomposition methods. Specifically, the focus will be on the Empirical Mode Decomposition (EMD) technique, its advanced variants, and the Variational Mode Decomposition (VMD) approach, which collectively offer adaptive and robust frameworks for analyzing complex, nonlinear, and nonstationary signals in rotating machinery

• Variational Mode Decomposition (VMD)

Proposed by K. Dragomiretskiy and D. Zosso [91] , the Variational Mode Decomposition (VMD) technique is an adaptive signal decomposition method grounded in the principles of Wiener filtering, Hilbert transform, and frequency mixing. Its primary objective is to decompose a real-valued signal f into a set of modes uk , each characterized by compact frequency support and distinct sparsity properties. Each mode uk is associated with a specific center frequency ωk , and together, these modes reconstruct the original signal. The sparsity of each mode is intrinsically linked to its bandwidth in the frequency spectrum.

To estimate the bandwidth of each mode, the VMD framework follows a systematic procedure. First, the Hilbert transform is applied to each mode uk to generate an analytic signal with a one-sided frequency spectrum. Next, an exponential tuning operation is performed to shift each mode's frequency spectrum toward the baseband, based on its estimated center frequency. Finally, the Gaussian smoothness of the demodulated signal in the H1 space is assessed to determine the bandwidth of each mode accurately.

The fractional modal decomposition process within VMD formulates a variational optimization problem, where the objective is to minimize the sum of the estimated bandwidths of all modes while ensuring that their combination reconstructs the original signal. The variational problem can be expressed as:

$$\min_{\{u_k\},\{\omega_k\}} \left\{ \sum_k \left\| \partial_t \left[\left(\delta(t) + \frac{j}{\pi t} \right) * u_k(t) \right] e^{-j\omega_k t} \right\|_2^2 \right\} \qquad (15)$$
$$f = \sum_k u_k$$

Here, f represents the input signal, $\{uk\} = \{u1, . . ., uk\}$ are the decomposed modes, $\{\omega k\} = \{\omega 1, . . ., \omega k\}$ are their corresponding center frequencies, δ(t) denotes the Dirac distribution, $\|\cdot\|_2$ represents the Euclidean norm, and * signifies the convolution operator.

To convert this constrained optimization problem into an unconstrained form, a quadratic penalty term (denoted by α) and a Lagrange multiplier λ(t) are introduced. The resulting augmented Lagrangian function is defined as:

$$L(\{u_k\},\{\omega_k\},\lambda) = \left\| y(t) - \sum_k u_k(t) \right\|_2^2 + \left\langle \lambda(t), y(t) - \sum_k u_k(t) \right\rangle + \alpha \sum_k \left\| \partial_t \left[\left(\delta(t) + \frac{j}{\pi t} \right) * u_k(t) \right] e^{-j\omega_k t} \right\|_2^2 \qquad (16)$$

The optimization problem is then solved iteratively by updating the mode functions *uk*, the center frequencies *ωk*, and the Lagrange multiplier λ(t) according to the following expressions:

$$\hat{u}_k^{n+1}(\omega) = \frac{\hat{y}(\omega) - \sum_{i>k} \hat{u}_i(\omega) + (\hat{\lambda}(\omega)/2)}{1 + 2\alpha(\omega - \omega_k)^2} \qquad (17)$$

$$\hat{\omega}_k^{n+1} = \frac{\int_0^\infty \omega \left| \hat{u}_k(\omega) \right|^2 d\omega}{\int_0^\infty \left| \hat{u}_k(\omega) \right|^2 d\omega} \qquad (18)$$

$$\hat{\lambda}^{n+1}(\omega) = \hat{\lambda}^{n}(\omega) + \tau \left(y(\omega) - \sum_k \hat{u}_k^{n+1}(\omega) \right) \qquad (19)$$

Here, τ denotes the update parameter, and the superscript *(n)* indicates the iteration number. The iterative process continues until the convergence criterion defined by:

$$\frac{\sum_k \left\| \hat{u}_k^{n+1} - \hat{u}_k^{n} \right\|_2^2}{\left\| \hat{u}_k^{n} \right\|_2^2} < \varepsilon \qquad (20)$$

is satisfied, where ε is a predefined tolerance threshold.

Through this iterative variational process, VMD effectively decomposes the signal into a finite set of intrinsic mode functions (IMFs) with compact frequency support, enabling precise time–frequency characterization and improved fault detection in rotating machinery applications.

- **EMD, EEMD, CEEMDAN and Improved CEEMDAN**

Empirical Mode Decomposition (EMD) has emerged as a highly effective time–frequency analysis technique extensively applied in rotating machinery diagnostics and other engineering fields. Originally introduced by Huang et al. [92], EMD provides an adaptive and data-driven approach for decomposing nonlinear and non-stationary signals into a set of intrinsic mode functions (IMFs). Its capability to analyze complex vibration signals without assuming linearity or stationarity has made it a reference method in the field of fault detection and diagnosis, particularly for bearings in rotating machinery and wind turbines.

Despite its advantages, the classical EMD method suffers from challenges such as mode mixing and boundary effects, which can distort the accuracy of the decomposition. To address these issues, Wu and Huang [93] introduced the Ensemble Empirical Mode Decomposition (EEMD), a variant that incorporates auxiliary white Gaussian noise to maintain continuity across scales. However, the inclusion of noise can introduce reconstruction errors and reduce signal integrity. To overcome this, Torres et al. [94] developed the Complete Ensemble Empirical Mode Decomposition with Adaptive Noise (CEEMDAN), which adds adaptive noise at each decomposition stage and computes a unique residual for each mode, thereby mitigating mode mixing and improving decomposition completeness.

While CEEMDAN enhanced EMD’s robustness, it still presented spurious modes and residual noise within the IMFs. Consequently, Colominas et al. [95] proposed the Improved CEEMDAN (ICEEMDAN) algorithm, which refines the computation of the local mean of the signal to derive cleaner modes. This improvement effectively reduces noise contamination and eliminates spurious components, significantly enhancing diagnostic accuracy.

In recent years, ICEEMDAN has become a widely adopted technique in the field of fault detection and condition monitoring, owing to its improved precision, stability, and ability to preserve essential fault-related features in vibration signals.

The basic decomposition process of Improved CEEMDAN is as follows [95]:

1) Add Gaussian white noise to the original signal:

$$X^{(i)} = x + \varepsilon_0 E_i(\omega^{(i)}), \quad i = (1,2,3,....,N) \qquad (21)$$

Where x is the input signal, ε_0 represents the signal-to-noise ratio (SNR) of the first decomposed signal, $E_i(.)$ denotes i**th** mode decomposed by EMD and $\omega^{(i)}$ is the i**th** added Gaussian white noise.

2) Calculate the first residue:

$$r_1 = \left\langle M\left(X^{(i)}\right)\right\rangle \qquad (22)$$

Where $M(.)$ the operator which produces the local means of $X^{(i)}$ and $\langle . \rangle$ denotes the averaging action.

3) Calculate the first IMF1:

$$\mathrm{IMF}_1 = x - r_1 \qquad (23)$$

4) Estimate the second residue as $r_2 = \left\langle M\left(r_1 + \varepsilon_1 E_2(\omega^{(i)})\right)\right\rangle$ and the second IMF2 is $\mathrm{IMF}_2 = r_1 - r_2$

5) Calculate jth residue as

$$r_j = \left\langle M\left(r_{j-1} + \varepsilon_{j-1} E_j(\omega^i)\right)\right\rangle \tag{24}$$

6) Calculate jth IMF as

$$\mathrm{IMF}_j = r_{j-1} - r_j \tag{25}$$

7) Return to the 5th step to compute next j

3.8 Conclusion

This chapter presented an overview of wind turbine failures and the principal maintenance and diagnostic techniques used to ensure their reliability. It examined common faults in major subsystems such as electrical, mechanical, and control components, emphasizing the importance of proactive maintenance strategies and dependability in sustaining operational performance. Various fault diagnosis methods were reviewed, with particular attention to vibration analysis methods—time domain, frequency domain, envelope, and advanced time-frequency analysis methods including Variational Mode Decomposition and improved empirical mode decomposition techniques such as CEEMDAN and ICEEMDAN—demonstrates the progression towards more sophisticated tools that can handle the non-stationary and noisy characteristics of turbine signals

This foundation sets the stage for the following chapter, which focuses on bearing fault diagnosis in rotating machinery—the core contribution of this work.

4

Contribution To Rolling Element Bearing Faults Identification In WT

4.1 Introduction

The continuous development of condition monitoring and fault diagnosis in rotating machinery has become essential to ensure system reliability, safety, and operational efficiency. Among the various components of rotating systems, bearings play a critical role in mechanical performance, and their degradation often leads to severe failures if not detected at an early stage. Traditional diagnostic approaches, while effective under certain conditions, are often limited when dealing with complex, non-stationary, and noisy signals typically encountered in industrial environments.

To address these challenges, this chapter presents the development and validation of a novel, integrated fault diagnosis methodology designed to tackle the specific challenges of wind turbine bearing monitoring. The proposed method [96] combines the adaptive decomposition capability of ICEEMDAN, the deterministic noise cancellation prowess of the AR model, and the impulse enhancement fidelity of MEDA. The process culminates in a squared envelope analysis to clearly identify the characteristic fault frequencies. The efficacy of this approach is rigorously demonstrated through two validation pathways: first, using benchmark experimental data from the Case Western Reserve University (CWRU) bearing data center, and second, and most importantly, through its successful application to real-world vibration data from a faulty high-speed shaft bearing in an operational wind turbine, provided by Green Power Monitoring Systems.

4.2 Experimental setup

Two datasets were employed in this thesis to evaluate, and validate the proposed diagnostic methodology. The first dataset originates from the well-known Case Western Reserve University (CWRU) bearing dataset [97], which provides controlled vibration measurements collected from an electric motor equipped with bearings mounted on a single shaft. This dataset serves as a benchmark for testing our proposed algorithm due to its large datasets.

The second dataset consists of real-world vibration data acquired from a faulty high-speed shaft bearing in an operational wind turbine, provided by Green Power Monitoring Systems [98]. This dataset captures the complex, nonstationary behavior of rotating machinery under real operational and environmental conditions, allowing for the assessment of the proposed method's robustness in practical scenarios.

Together, these datasets enable a comprehensive evaluation of the proposed approach, combining both controlled experimental analysis and validation on actual industrial equipment to ensure accuracy, generalizability, and real-world applicability.

4.2.1 CWRU Bearing Test Rig

Some of the bearing vibration signals utilized in this study were obtained from the Bearing Data Center of Case Western Reserve University (CWRU) [97]. This publicly available dataset has been extensively used in the research community for benchmarking fault diagnosis methods. As illustrated in Figure 23, the experimental setup comprises an electric motor, a torque transducer, and a dynamometer, allowing controlled acquisition of bearing vibration data under various fault conditions. However, certain recorded signals contain impulsive noise generated by other mechanical components, which introduces challenges in accurately identifying the appropriate frequency band for reliable bearing fault diagnosis.

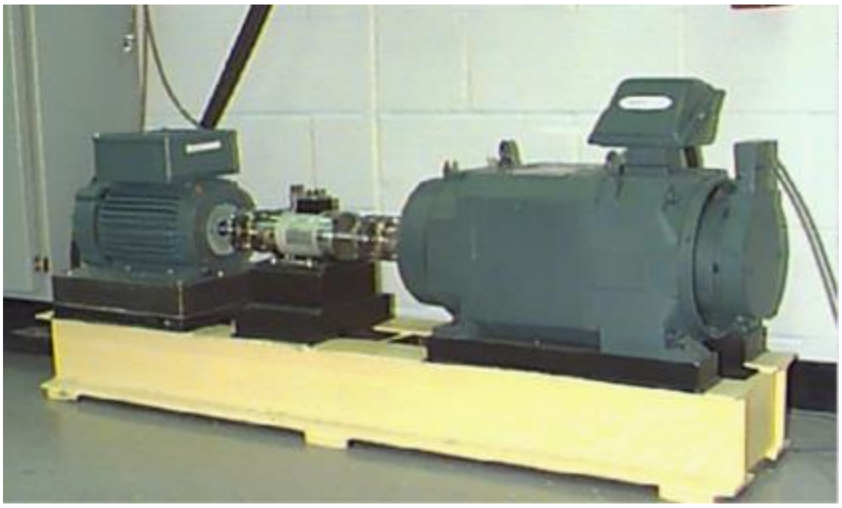

Figure 23 : Case Western Reserve University (CWRU) test rig [97]

Vibration measurements were acquired at the motor's drive end using an accelerometer mounted on the induction motor housing, with sampling conducted at 12 kHz and 48 kHz. Beyond the healthy baseline, three representative bearing defects—inner race, outer race, and rolling element—were introduced by electro-discharge machining (EDM) at severities of 0.007, 0.014, and 0.021 inches on SKF 6205-2RS JEM test bearings. The rig operated under loads from 0 to 3 HP, producing shaft speeds between 1797 and 1720 rpm across tests. Bearing corresponding characteristic defect frequencies are summarized in Table 1 to support frequency-domain interpretation and validation. In the analysis reported here, four cases are considered: an outer race fault, a rolling element fault, and an inner race fault—each with a 0.014-inch defect size—together with a healthy condition, all recorded at 1750 rpm using a 48 kHz sampling rate.

Table 1 : Bearing fault frequencies

Motor load (HP)	Rotation Speed (RPM)	Rotational Frequency (Hz)	Fault Frequency of Outer race (Hz)	Fault Frequency of Inner race (Hz)	Fault Frequency of Ball (Hz)
1	1750	29.16	104.56	157.94	137.48

4.2.2 Real-World faulty bearing of a wind turbine generator provided by the Green Power Monitoring Systems (U.S)

Vibration data were acquired on an in-service 2 MW wind turbine generator (Suzlon S88) instrumented for drivetrain monitoring [98]. The high-speed shaft, driven by a 200-tooth pinion gear and supported by high-speed stage bearings located upstream and downstream of the shaft, rotated between 1,500 and 1,800 rpm during power production. A total of 50 days were included in the data campaign, spanning March 07, 2013 to April 25, 2013. On each monitored day, a single raw recording of 6 seconds was collected at a 100 kHz sampling rate, yielding high-fidelity snapshots. On the final monitoring day, physical inspection of the test bearing confirmed an inner-race fault with the shaft operating at 30 Hz, the corresponding theoretical inner-race characteristic frequency of 284.3 Hz provided the diagnostic target.

Figure 24 : Inner race fault on the high-speed shaft bearing [99]

4.3 Proposed Methodology

Early-stage rolling bearing faults in wind turbines manifest as weak, impulsive signatures that are easily masked by discrete gear tones and broadband noise, which necessitates a diagnostic pipeline that can adaptively isolate, enhance, and demodulate fault-related content under non-stationary conditions. To address this challenge, the proposed method is structured into three sequential stages—Signal decomposition, Signal pre-processing, and Envelope analysis—forming an end-to-end procedure from raw vibration to fault frequency identification as summarized in the method flowchart Figure 25.

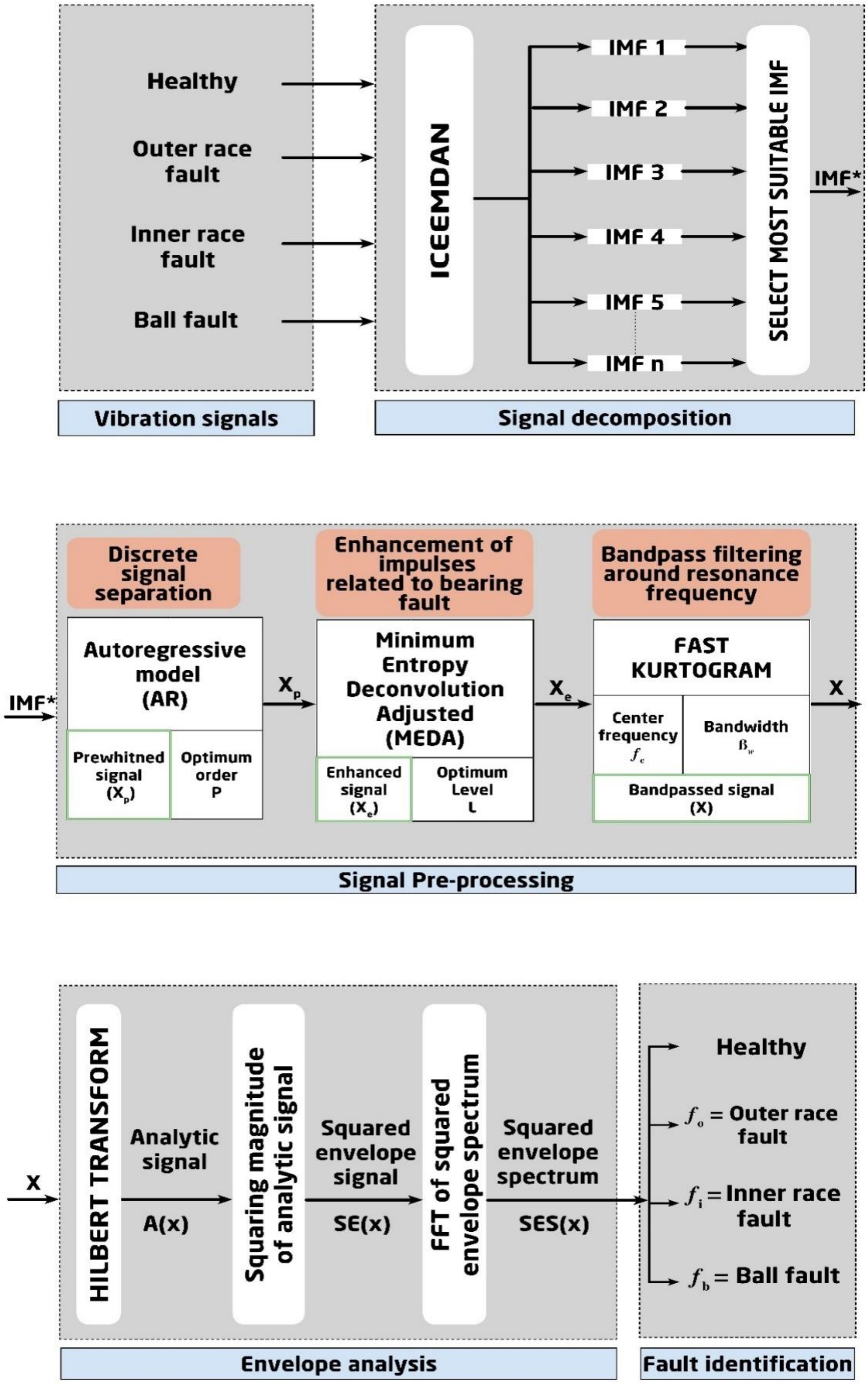

Figure 25 : Proposed method [96]

4.3.1 Signal decomposition

To reveal weak, impulsive signatures of early bearing faults hidden by gear tones and broadband noise, the method begins with adaptive signal decomposition using Improved Complete Ensemble Empirical Mode Decomposition with Adaptive Noise (ICEEMDAN), which partitions the raw vibration into intrinsic mode functions (IMFs) that better capture nonstationary, non-Gaussian dynamics while mitigating mode mixing and residual noise compared with conventional approaches. After decomposition, the most fault-informative IMF is selected via the Pearson correlation coefficient with the original signal—an objective criterion that prioritizes components preserving fault content. This two-step procedure is important because it separates bearing-related information from confounding excitations at the source.

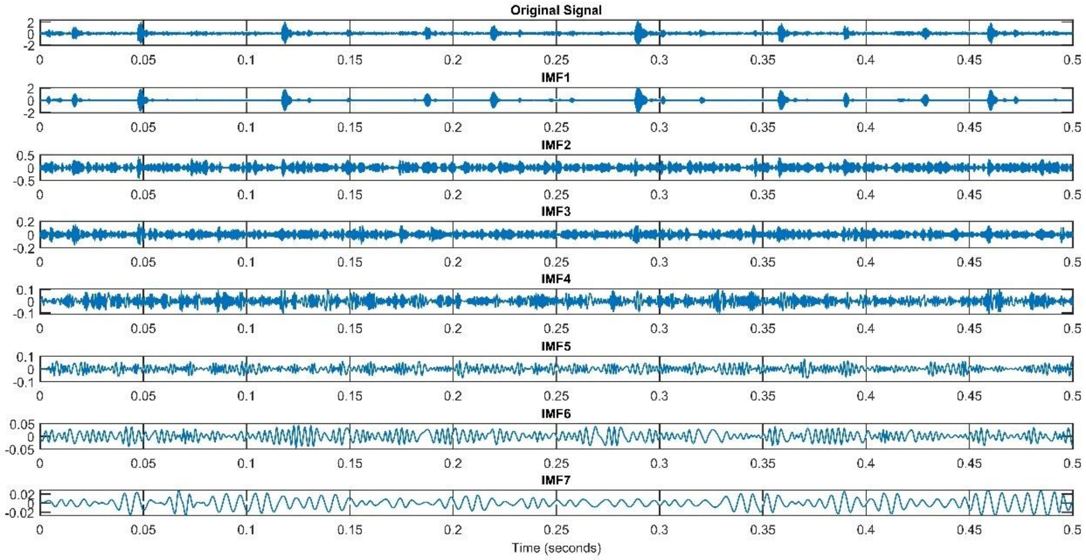

Figure 26 : ICEEMDAN decomposition of a bearing with inner race defect

In the case study illustrated for an inner-race crack, the ICEEMDAN decomposition visibly separates the raw vibration into a hierarchy of intrinsic mode functions (IMFs) in which the impulsive content associated with the defect concentrates in the highest-energy, higher-frequency modes (Figure 26), while lower-frequency IMFs predominantly capture slow structural or operational trends. To objectively select the most informative component for downstream processing, the Pearson correlation coefficient is computed between each IMF and the original faulty signal, yielding a ranked list that prioritizes the IMF best preserving the defects' impulsive signatures results depicted in Figure 27.

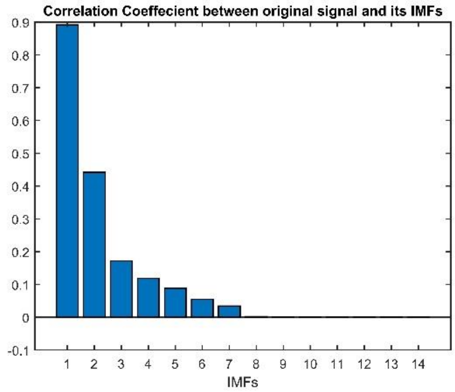

Figure 27 : Correlation coefficient between original signal and its IMFs

4.3.2 Signal pre-processing

Vibration signals from wind turbine drivetrains often exhibit strong discrete components from gearmesh and shaft harmonics that mask the weak, impulsive signatures of bearing faults, even when no gear damage is present[100]. To segregate these deterministic tones from fault-related content, the selected intrinsic mode function (IMF) is processed with a linear-prediction autoregressive (AR) model [101]; the model output estimates the deterministic part, and the prediction error (residual) serves as a prewhitened signal that retains the impulsive bearing information for diagnosis. This AR-based separation improves the signal-to-noise ratio for subsequent impulsive enhancement and envelope demodulation by attenuating gear-related lines at their source. In this study, the AR order is selected by maximizing the residual kurtosis, ensuring that whitening emphasizes transient events while avoiding overfitting and preserving diagnostically relevant impulses [102].

Once the autoregressive model has prewhitened the vibration signal to remove deterministic gear and shaft frequencies, the resulting residual is further processed using Minimum Entropy Deconvolution Adjusted (MEDA) [103], [104] to intensify fault-related impulses [105], [106]. MEDA works by finding a digital filter that maximizes the kurtosis of its output, effectively sharpening and accentuating impulsive features such as those produced by rolling element defects. Unlike conventional approaches, MEDA addresses common artifacts like spurious start-up impulses and improves the fidelity of periodic transients, which is essential for accurate fault detection. By enhancing the temporal structure and periodicity of these weak impacts, this step substantially boosts the detectability of characteristic bearing fault frequencies in the subsequent envelope analysis and ensures the diagnostic process is both sensitive and robust in the presence of noise and competing vibrations.

4.3.3 Envelope Analysis

After prewhitening and impulsive enhancement, the envelope analysis step is employed to extract the most diagnostically relevant modulation frequencies from the vibration signal. Once the signal has been bandpass-filtered around the optimal frequency band, as objectively determined by the Fast Kurtogram, the analytic signal is computed using the Hilbert transform and its envelope is squared. This squared envelope spectrum (SES) translates the periodic impacts of bearing faults into sharp spectral peaks, revealing their signature frequencies and harmonics even under intense noise and variable operating conditions. By centering on the resonance where faults are most pronounced, envelope analysis substantially increases sensitivity to weak faults, transforming subtle peaks in the time domain into clear markers within the frequency domain. This procedure is critical for reliably identifying the presence—and even the type—of bearing faults, facilitating maintenance and early intervention in wind turbine applications. The resulting FFT spectra of the squared envelope from faulty bearing is presented in Figure 28.

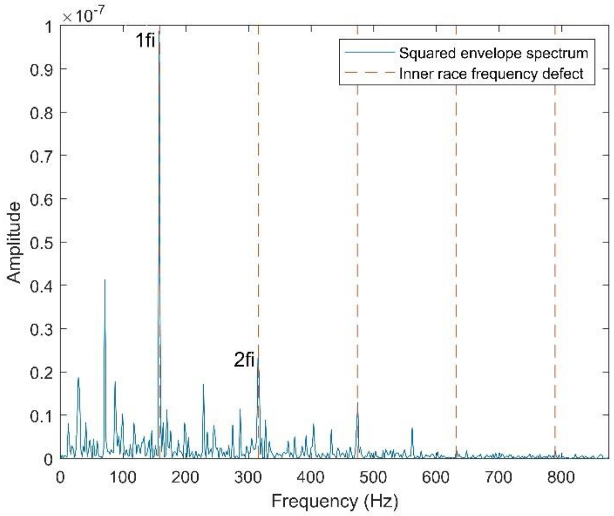

Figure 28 : Squared envelope spectrum of a faulty bearing (with inner crack)

4.4 Application Of The Proposed Model On CWRU Setup

This section details the practical application of the proposed diagnostic model using the Case Western Reserve University (CWRU) bearing test platform—a well-established benchmark for evaluating vibration-based fault detection methods. Here, the analysis targets three specific failure modes: inner race fault, outer race fault, and rolling element (ball) fault, each implemented as a single-point defect with a diameter of 0.014 inches. All datasets were collected at a rotational speed of 1750 rpm using an accelerometer with a 48 kHz sampling frequency, providing high-resolution time-series data for thorough investigation.

4.4.1 Outer Race Bearing Fault Analysis

For Case 1, the process of diagnosing an outer race bearing fault begins by decomposing the acquired vibration signal at 1750 rpm using ICEEMDAN, which separates the complex waveform into distinct intrinsic mode functions (IMFs) that capture relevant signal features while suppressing noise and mode mixing.

This step is vital because it allows the fault-related impulses—often masked by other mechanical and operational influences—to be isolated at a finer resolution. The next step involves selecting the most informative IMF based on the Pearson correlation coefficient; the first IMF typically exhibits the highest correlation with the original signal, ensuring that it retains the dominant fault characteristics necessary for downstream analysis (Figure 29a).

This selected IMF is then filtered with an autoregressive (AR) model to further enhance diagnostic clarity by removing deterministic periodic components, such as gearmesh or shaft harmonics. The AR order is carefully chosen—by maximizing the kurtosis of the residual—to preserve impulsive content critical to fault identification, yielding a prewhitened signal in which periodic impulses are amplified (Figure 29b). This prewhitening is fundamental: by normalizing and stabilizing the signal background, it makes subsequent impulse enhancement far more effective.

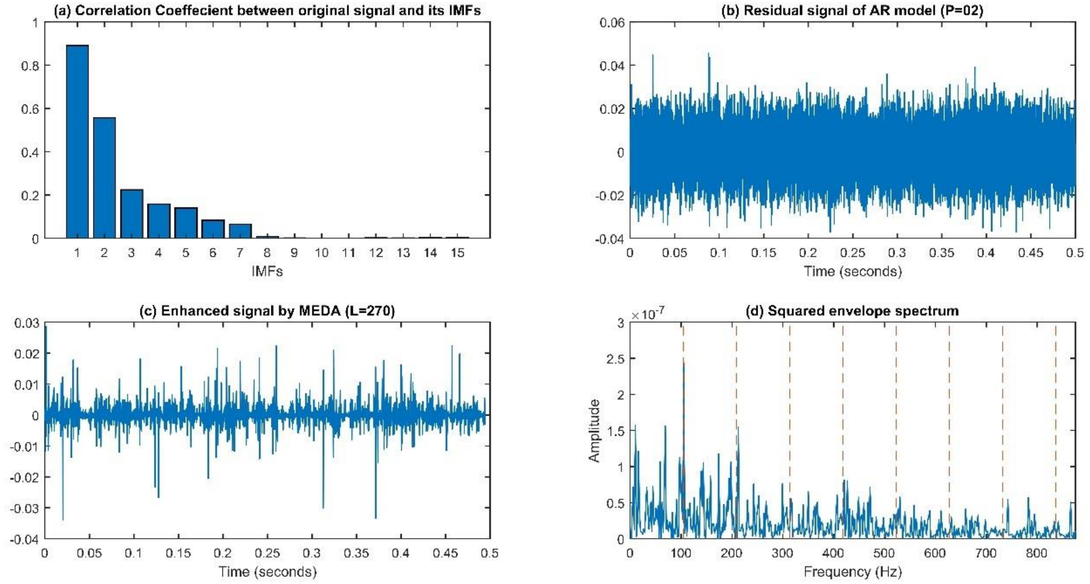

Figure 29 : Results obtained from a bearing with Outer race crack

The prewhitened residual is then processed using the Minimum Entropy Deconvolution Adjusted (MEDA) algorithm, which isolates and sharpens periodic shock signatures characteristic of bearing faults by maximizing the kurtosis (impulsiveness) of the filter output. MEDA is particularly advantageous compared to classical deconvolution methods because it mitigates the formation of spurious start-up impulses and robustly enhances weak, repetitive impacts typically associated with incipient failures. This results in a much higher signal-to-noise ratio for impulse detection (Figure 29c).

Next, the signal is bandpass-filtered within the optimal demodulation region, as determined by the Fast Kurtogram, typically covering 0–12 kHz in this case. Envelope analysis is performed by computing the squared envelope spectrum (SES) of the filtered output (Figure 29d). This final step is essential as it translates repeated impacts into sharp peaks at the defect's characteristic frequencies and their harmonics, allowing unambiguous identification of the fault type—in this instance, a dominant SES peak at 104.56 Hz corresponding to the theoretical outer race defect frequency (BPFO), corroborated by supporting harmonics.

The synergy of these sequential stages ensures weak fault signatures can be detected under real-world noise, mechanical variability, and operational complexity, greatly improving diagnostic reliability and robustness compared with traditional single-step approaches.

4.4.2 Inner Race Bearing Fault Analysis

For the analysis of the inner race bearing fault, vibration data were collected from a defective bearing using an accelerometer and processed following the structured methodology applied to the previous cases. Figure 30 showcases the critical step of selecting the optimal autoregressive (AR) model order P by plotting the kurtosis value for each possible AR order. The plot reveals a distinct peak at P=233, where kurtosis reaches its maximum. This indicates that at this order, the AR model is most effective at prewhitening the signal and enhancing the impulsiveness of residual fault-related features—essential for reliable defect detection.

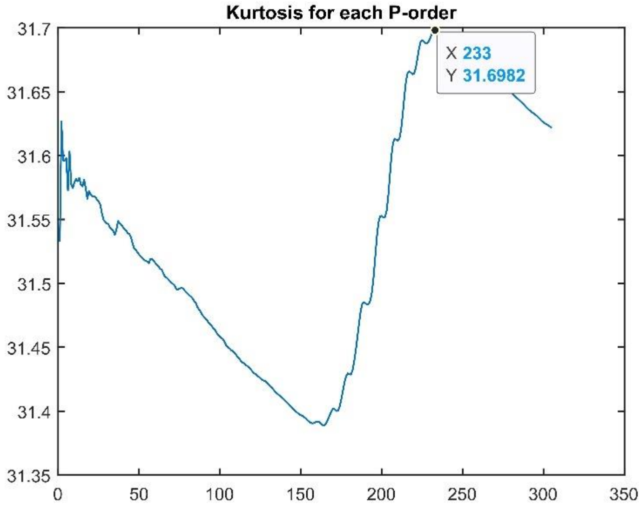

Figure 30 : Kurtosis of each order P of an inner race cracked bearing

Figure 31 illustrates the step-by-step signal transformation. The first subplot shows the original noisy vibration signal. The second subplot presents the optimum intrinsic mode function (IMF) extracted after ICEEMDAN decomposition, capturing the most fault-informative components. The third subplot demonstrates the resulting residual after AR filtering with the optimal order. This "very prewhitened" signal displays a significant reduction in deterministic components, allowing the impulsive events linked to the inner race defect to stand out more prominently. Together, these figures highlight the benefit of our processing methodology in isolating crucial defect-related features within complex and noisy bearing vibration data.

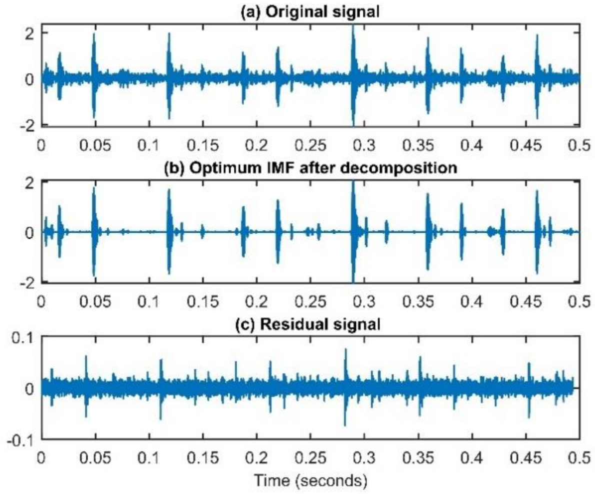

Figure 31 : Signal transformation of an Inner race cracked bearing

In the following analysis, the goal was to show that the proposed method preserves important fault information better than a standard envelope spectrum applied directly to raw data. By carefully preprocessing the signal and extracting the most relevant parts, our approach reveals fault frequencies and their harmonics with greater clarity and less noise (Figure 32a). In contrast, the conventional envelope spectrum, when used without these preprocessing steps (Figure 32b), tends to miss or blur these critical features—making faults harder to identify. This side-by-side comparison clearly demonstrates that our method is more effective in highlighting and retaining the essential details needed for accurate bearing fault diagnosis.

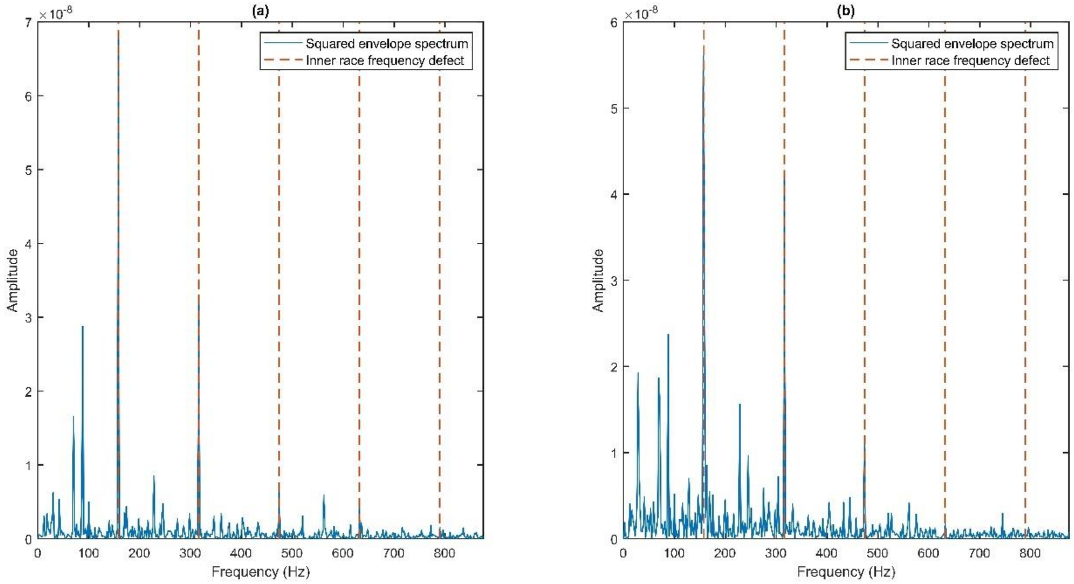

Figure 32 : the squared envelope spectrum of a bearing with inner race crack: (a) without processing, (b) using our proposed method

4.4.3 Rolling Element Bearing Fault Analysis

In the analysis of the rolling element bearing fault, the vibration signal recorded at 1750 rpm is initially decomposed using ICEEMDAN, isolating several intrinsic mode functions (IMFs) to enhance the separation of nonstationary and fault-related features from noise and structural tones. Among these IMFs, the first mode is identified as the most diagnostically significant by evaluating their

Pearson correlation coefficients in Figure 33(a) step that ensures the primary fault information is retained for further processing, as supported by studies showing correlation-based IMF selection improves clarity in time-frequency bearings analysis. This selected IMF is subsequently filtered with an autoregressive (AR) model (with optimal order P=2), which suppresses residual periodic disturbances so that the remaining signal is heavily weighted towards impulsive content characteristic of bearing defects.

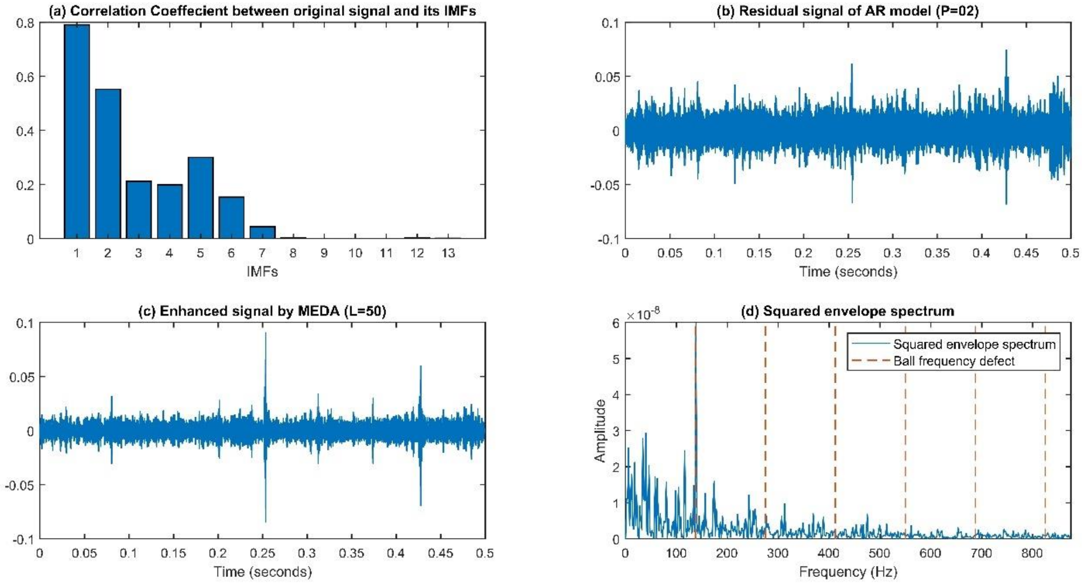
(a) Correlation Coeffecient between original signal and its IMFs

(b) Residual signal of AR model (P=02)

(c) Enhanced signal by MEDA (L=50)

(d) Squared envelope spectrum

Figure 33 : Rolling element-fault results obtained using our proposed methods: (a) Correlation coefficient between raw signal and it's IMFs, (b) residual signal after Autoregressive filtering of 1st IMF, (c) Enhanced residual signal with MEDA and (d) it's Squared envelope spectrum

Further refinement of this prewhitened signal is achieved using Minimum Entropy Deconvolution Adjusted (MEDA), with a selected filter length of 50, to maximize the kurtosis and sharpen transient impulses, making weaker fault events more prominent within a noisy environment (shown in Figure 33(c)). The necessity and advantage of this step are widely highlighted in modern bearing fault literature, emphasizing how MEDA accentuates periodic impacts and mitigates masking by operational and mechanical interferences. Finally, the enhanced output is subjected to envelope analysis in the frequency band 0–24 kHz, where the squared envelope spectrum depicted in Figure 33(d) reveals a clear dominant peak at 137.48 Hz. This frequency directly corresponds to the ball defect characteristic, confirming both the method's diagnostic accuracy and its ability to discriminate between different fault types, thus supporting reliable, real-world bearing condition monitoring.

4.5 comparison with literature methods

To assess the effectiveness of our method in detecting bearing faults, we conducted a comparative analysis using the same raw vibration data set and evaluated it against three advanced bearing fault diagnosis methods from the benchmark study by Smith et al [107], as well as the Minimum Entropy Deconvolution with Spectral Kurtosis (MED-SK) technique proposed by Sawalhi et al [108]. The objective was to determine which approach offers the most reliable and clear identification of different defect types. The results, shown in the table below, clearly demonstrate that our proposed method is consistently able to diagnose both outer race and rolling element defects, whereas the other methods either partially identify or fail to detect these faults under the same conditions.

Table 2 : Comparison of our method with other advanced bearing-fault-diagnosis methods

Defect type	Our proposed method	Method 1: Envelope analysis [99]	Method 2: Cepstrum prewhitening [99]	Method 3: Benchmark method [99]	Method 4: MED-SK [100]
Outer race damage	Yes	Partially	No	No	No
Rolling element damage	Yes	Partially	Partially	Yes	Yes

"Yes" represents fault clearly diagnosable, "Partially" represents fault partially diagnosable, "No" represents fault not diagnosable

4.6 Real-World Validation of Bearing Fault Detection Methodology on Wind Turbine Data

The proposed diagnostic method was tested on real data from a Suzlon S88 wind turbine with a high-speed shaft bearing over 50 days. This dataset was processed using our methodology, which identified a dominant spectral peak near the calculated fault frequency for an inner race defect (280.12 Hz vs. 284.3 Hz theoretical) in Figure 34, as well as its harmonic. This confirms that our approach reliably detects bearing faults under practical wind turbine conditions, demonstrating both its accuracy and effectiveness for real-world condition monitoring.

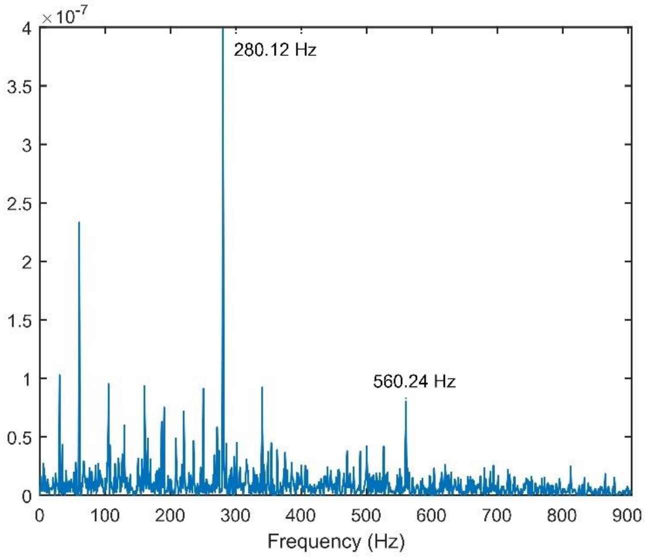

Figure 34 : Squared envelope spectrum of 48th day

4.7 Conclusion

In conclusion, this chapter has presented a comprehensive contribution to the field of bearing fault diagnosis, introducing a robust methodology that effectively combines advanced signal processing, adaptive mode selection, and impulsive feature enhancement. Through extensive validation on both benchmark laboratory datasets and real-world wind turbine measurements, the proposed approach consistently demonstrated superior accuracy, clarity, and reliability in detecting a variety of bearing faults—even in the presence of noise and operational complexity. By exceeding the diagnostic capabilities of conventional and state-of-the-art methods, this work not only advances the practical readiness of vibration-based monitoring in industrial settings but also provides a solid foundation for future extensions to more complex machinery health applications.

5

Contribution To An Intelligent Bearing Diagnosis

5.1 Introduction

This chapter presents a novel contribution to the field of intelligent bearing diagnosis for wind turbines, building on recent advances in both signal processing and deep learning. The new method integrates Variational Mode Decomposition (VMD) [91] for adaptive signal decomposition and Autoregressive (AR) filtering for noise suppression and impulsive feature enhancement. At its core is an improved deep learning architecture—ConvNeXt—which merges the strengths of Convolutional Neural Networks (CNNs) and Transformer models to capture both local and long-range features from [109] Hilbert envelope spectrum images. This combination is specifically tailored to address early-stage and weak bearing faults, which are often masked by noise and complex operational environments in wind turbines. The methodology was rigorously evaluated using the Case Western Reserve University (CWRU) bearing dataset and demonstrates superior accuracy, generalization, and robustness compared to several existing state-of-the-art approaches. This chapter not only extends the thesis's foundational research but also bridges the gap between advanced signal processing and modern deep learning for practical, automated condition monitoring in renewable energy systems.

5.2 Data Preparation and Experimental Setup

The data preparation and experimental setup in this study are designed to facilitate robust evaluation of the proposed intelligent bearing fault diagnosis framework. Vibration signals were collected from the Case Western Reserve University (CWRU) bearing test rig Figure 23 using acceleration sensors mounted at the drive end of the motor, with a sampling frequency of 12 kHz. Four bearing health conditions were considered: normal, ball fault, inner race fault, and outer race fault. Faults were artificially introduced via electro-discharge machining with diameters of 7 and 14 mils, and signals were acquired under motor loads of 0, 1, 2, and 3 hp for realistic operational diversity.

For effective network training and testing, each raw vibration record was segmented into frames of 9600 samples each which corresponds to a sample of 0.8 second as shown in Figure 35, with a sliding window of 512 data points to generate overlapping samples—expanding the dataset via data augmentation and increasing the model's exposure to diverse conditions. Each health state contributed 1,752 samples, with 755 additional samples for the normal class, culminating in 6,011 total samples. The dataset was then split into 5,105 samples for training and 906 for testing, with 20% of the training set further reserved for validation. Table 3 provides an overview of the dataset distribution.

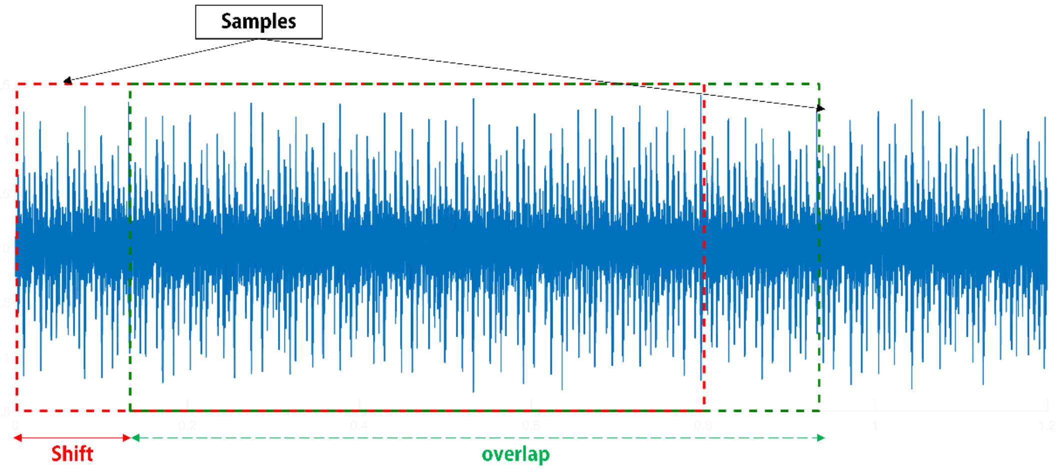

Figure 35 : Data augmentation with overlap

Table 3 : Dataset division

Bearing state	Motor load (hp)	Fault diameter (mil)	Number of samples
Ball fault (BF)	0 1 2 3	7 14	1752
Inner race fault (IF)	0 1 2 3	7 14	1752
Outer race fault (OF)	0 1 2 3	7 14	1752
Normal condition (NC)	0 1 2 3		755

5.3 Experiments Procedure

This research introduces a novel methodology that integrates Variational Mode Decomposition (VMD), Autoregressive (AR) filtering, and the ConvNeXt deep learning architecture to advance the diagnosis of wind turbine bearing faults. VMD and AR filtering are established techniques for enhancing signal quality, with VMD excelling at suppressing noise interference. However, VMD alone may not fully eliminate unknown interference, particularly from low-frequency components; AR filtering addresses this by further purifying the signal and isolating impulsive fault-related features.[110]

The true innovation of this approach lies in its synthesis with ConvNeXt, a modern deep learning model designed to capture intricate local and global characteristics in Hilbert envelope spectrum images. This is especially critical for the reliable identification of subtle bearing faults that are frequently masked by environmental noise and operational influences.

Distinguishing itself from traditional convolutional neural networks, ConvNeXt employs a Transformer-inspired design that is optimized for learning long-range dependencies in two-dimensional input data. This improved architecture enables more accurate diagnosis in scenarios where faults present with weak or obscured signatures, surpassing previous methods in both precision and consistency.

The methodological workflow—combining VMD, AR filtering, and ConvNeXt—is illustrated in Figure 36. By leveraging this integrated framework, the proposed system delivers robust, precise, and generalizable fault detection and classification, thus making a substantive contribution to intelligent condition monitoring in rotating machinery.

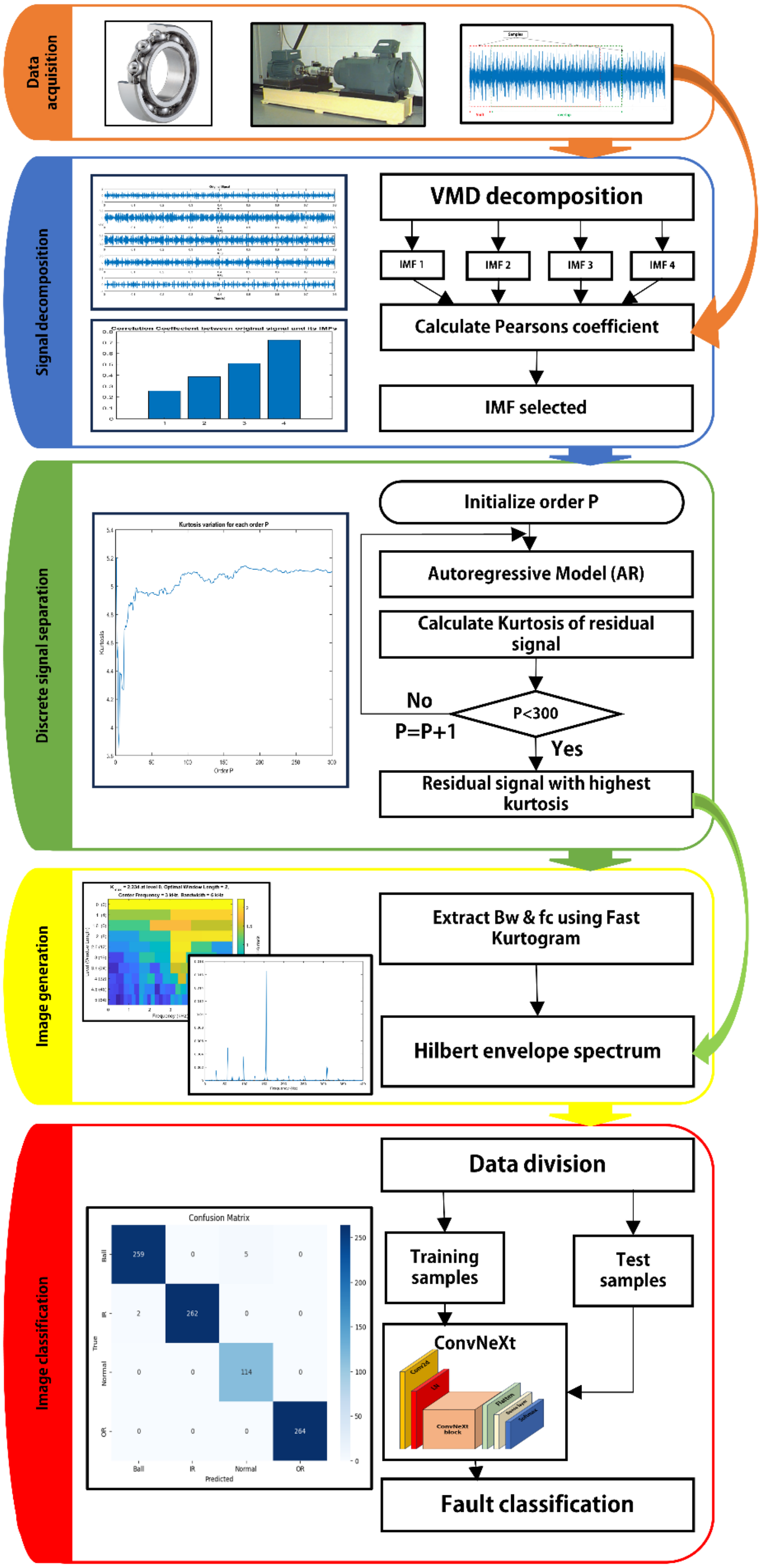

Figure 36 : VMD-AR-ConvNext Methodology

5.3.1 Signal Decomposition

In real-world vibration signals, the detection of bearing fault impulses is often made difficult by the presence of strong external and background interferences. Enhancing the visibility of these fault-related impulses requires effective reduction of high-frequency disturbances to improve the underlying signal's quality. To address this, Variational Mode Decomposition (VMD) is employed to decompose the raw signal into four stationary component modes, as illustrated in Figure 37.

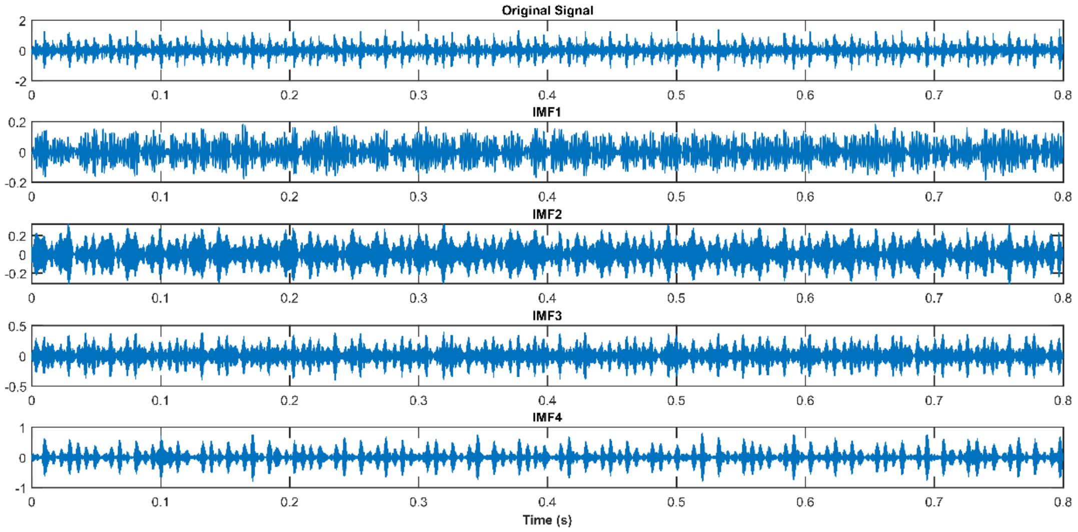

Figure 37 : VMD decomposition result

Each mode captures distinct oscillatory trends present in the signal. Among these, the Intrinsic Mode Function (IMF) that exhibits the highest correlation coefficient with the original signal is selected, as it encapsulates the most information about the bearing's health state. The relevance of each IMF is quantitatively assessed, with Figure 38 showing the correlation coefficients, thereby ensuring the most diagnostically informative component is propagated to subsequent analysis stages.

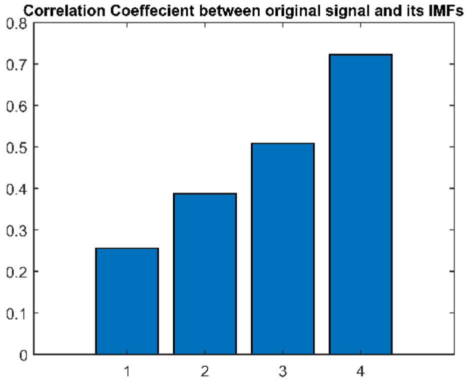

Figure 38 : Correlation coefficient between raw signal and its IMFs

5.3.2 Discrete Signal Separation

After mode decomposition, the IMF containing the most fault-related features is further refined using an Autoregressive (AR) model-based filtering technique. This step is essential for eliminating unknown, especially low-frequency, interference terms, ultimately increasing the signal-to-noise ratio and more distinctly isolating fault characteristics. The prediction performance of the AR model is critically dependent on its order p. To optimize this model, a systematic search is conducted over possible values of p, with the goal of selecting the order that maximizes the kurtosis of the resulting residual signal.

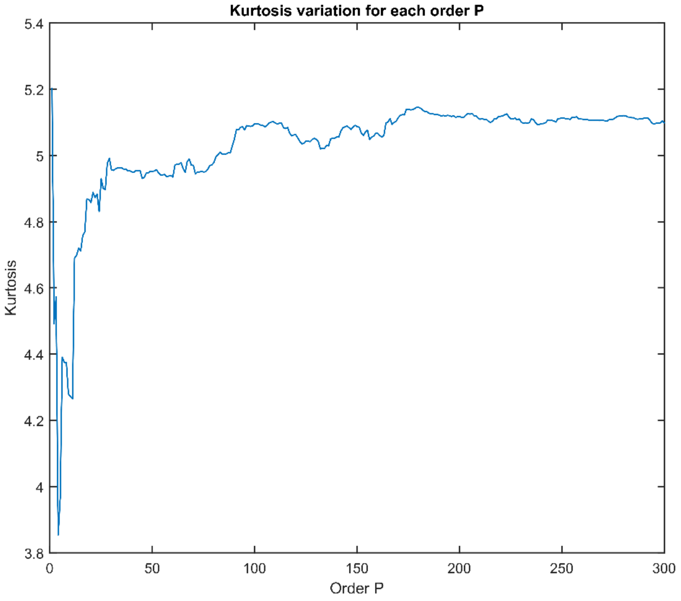

Figure 39 : Kurtosis of each order P

Figure 39 demonstrates how kurtosis serves as a quantitative indicator for optimal order selection, ensuring that the retained signal emphasizes the impulsive features most indicative of bearing faults.

5.3.3 Image Generation

Once the signal has been augmented and purified, focus shifts to the generation of a two-dimensional feature representation suitable for deep learning. First, the fast kurtogram is applied to the filtered signal to determine the most suitable demodulation band, specifically identifying the optimal center frequency (fc) and bandwidth (Bw) containing the target fault frequency. The signal is then bandpass filtered, and the Hilbert transform is employed to generate the Hilbert envelope spectrum image, as displayed in Figure 40.

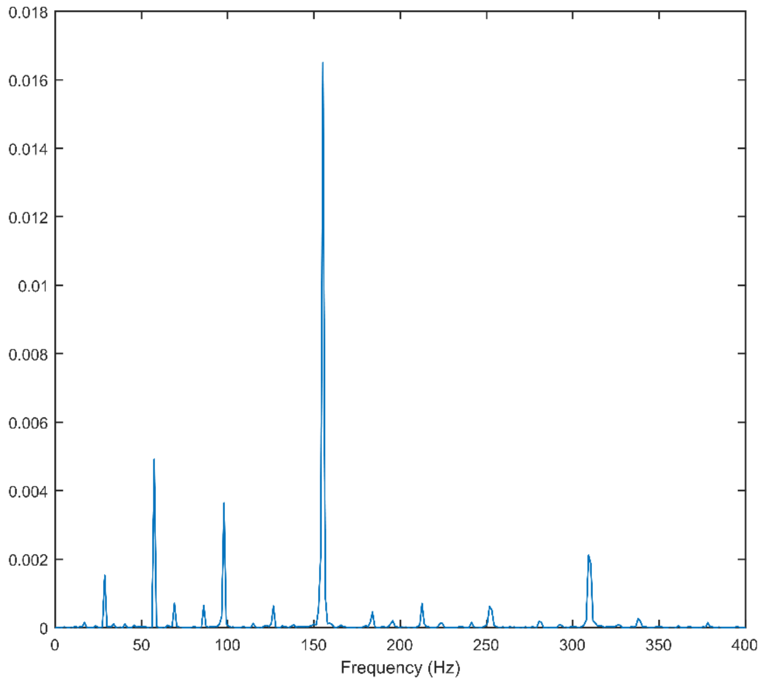

Figure 40 : Hilbert envelope spectrum

These spectrum images markedly reveal fault frequencies and their harmonics, visually capturing the presence of defects and providing valuable insight into the signal's fault characteristics.

Accurately identifying the state of a bearing using raw vibration signals alone can be challenging due to the complex and overlapping nature of signal components. Each type of bearing fault manifests unique characteristic frequencies and harmonics, which become evident in the Hilbert envelope spectrum. For instance, Figure 41(a) illustrates the spectrum of a healthy bearing, marked primarily by the frequency of the rotating shaft, while Figure 41(b), (c), and (d) display distinct spectral peaks corresponding to inner race, outer race, and ball defects, respectively.

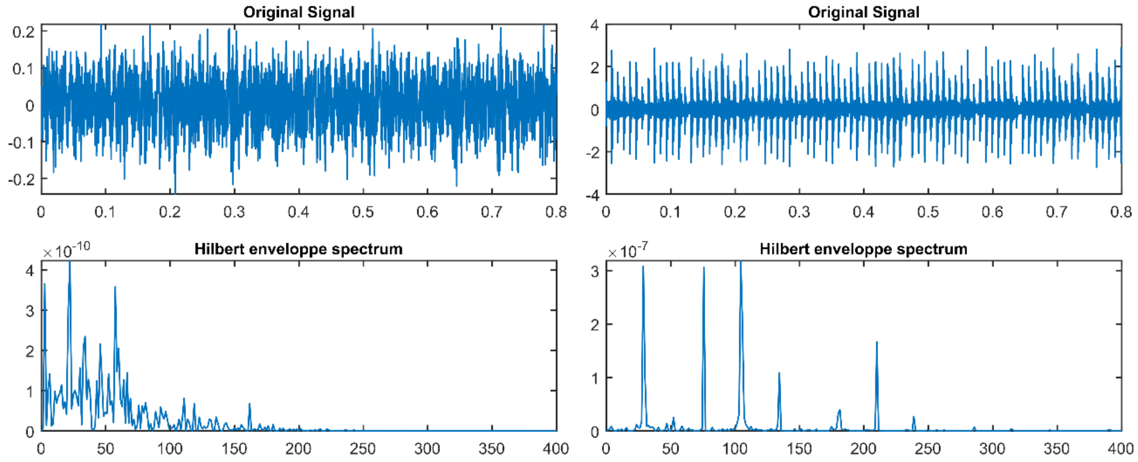

(a) Normal condition **(b) Inner race fault**

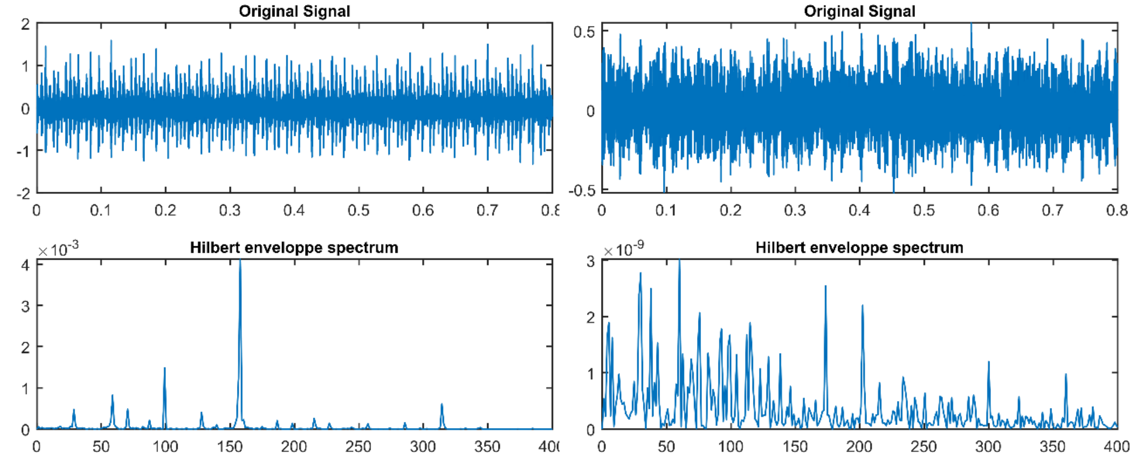

(c) Outer race fault **(d) Ball Fault**

Figure 41 : The results of Hilbert envelope spectrum of different bearing state: (a) healthy bearing, (b) Inner race defect, (c) outer race defect, and (d) rolling element defect

These clear spectral signatures allow for the visual differentiation of fault types, enabling the resulting time-frequency images to serve as effective inputs for convolutional neural networks in subsequent automated feature extraction and classification tasks.

5.4 Machine Learning Technique

To effectively capture both local and global diagnostic features in Hilbert envelope spectrum images, this study adopts the ConvNeXt architecture—an advanced deep learning model developed for robust image-based classification tasks. To address the challenge of limited labeled bearing fault data, a transfer learning approach is employed, wherein a ConvNeXt-tiny model pretrained on the large-scale ImageNet dataset serves as the foundation. The model is then fine-tuned using vibration spectrum images specific to bearing faults, Figure 42 depicts the transfer learning framework typically utilized in fault diagnosis.

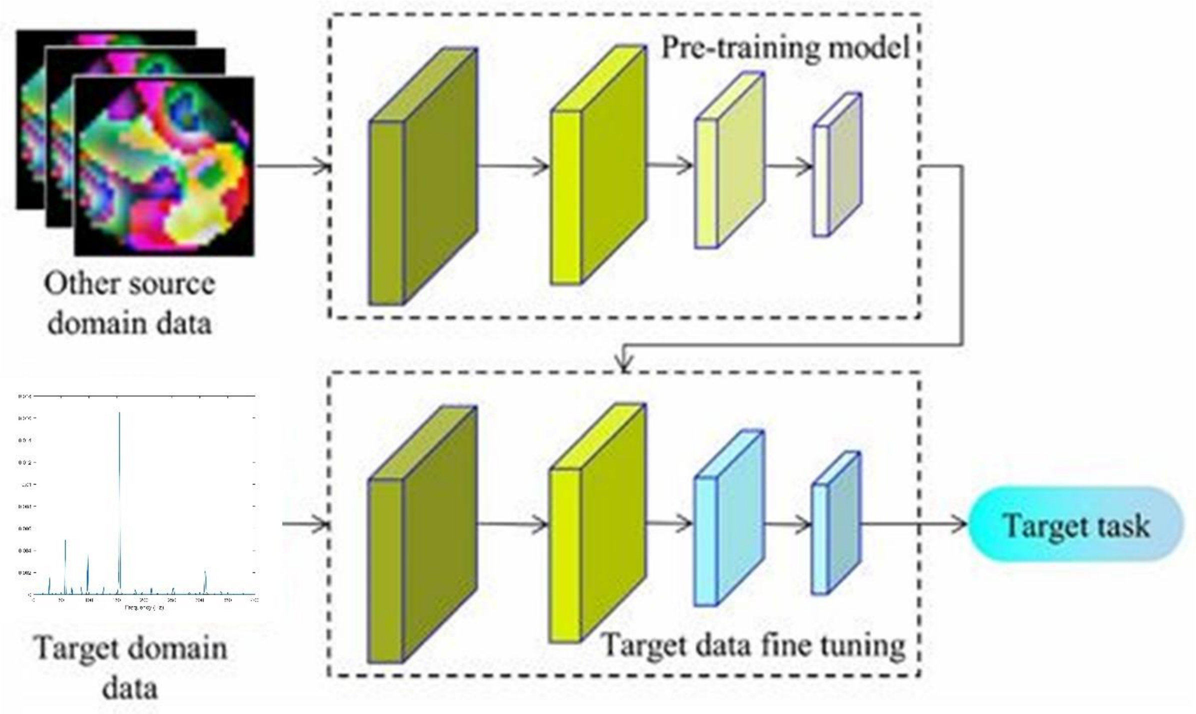

Figure 42 : Transfer learning framework

This process involves replacing the original classification layer with a new softmax layer tailored to the fault categories of interest and adding global average pooling and dense layers to enhance feature abstraction and adaptability. All model layers are made trainable, enabling refined adjustments across both general and task-specific representations. The structure, adaptations, and effectiveness of the proposed network are concisely illustrated in Figure 43, highlighting how architectural innovations enhance diagnostic precision.

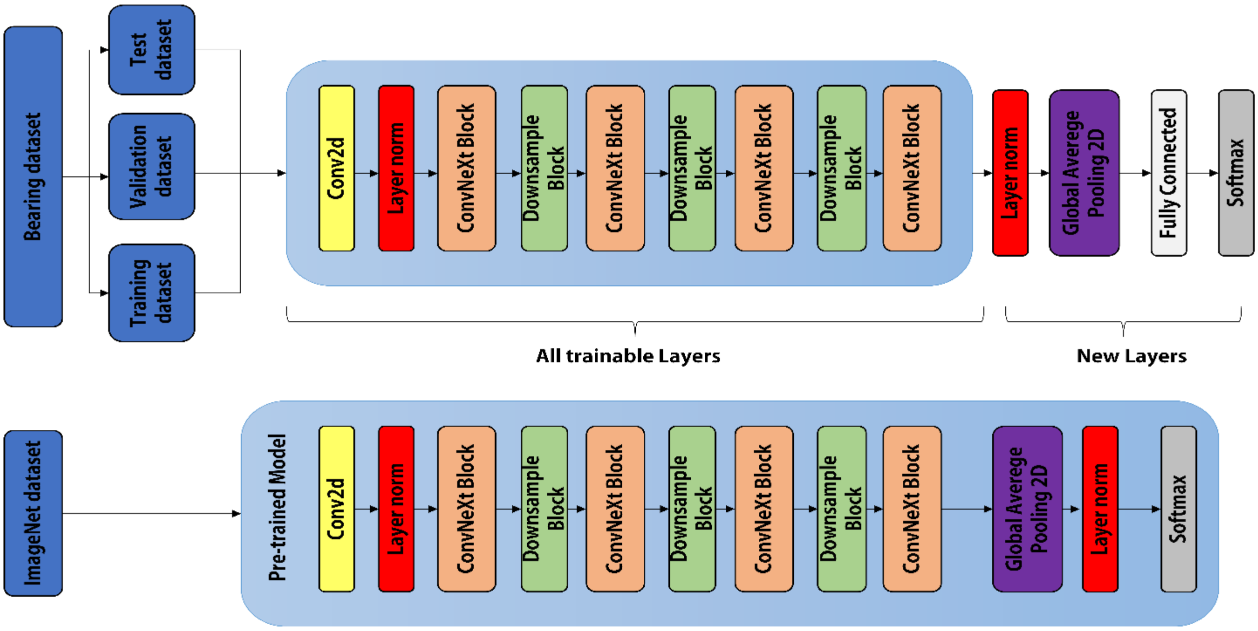

Figure 43 : Bearing fault diagnosis based on fine-tuning

Fine-tuning is conducted with a low learning rate to prevent overfitting and preserve beneficial pre-learned features. This strategy not only accelerates convergence and reduces the need for extensive labeled data but also significantly improves model generalization and fault discrimination performance in the bearing health monitoring scenario.

5.5 Experimental Settings and Results

In this study, we define a set of candidate values for multiple hyperparameters and employ cross-validation to assess the performance of each hyperparameter combination, thereby identifying the optimal configuration. The selected optimal parameters are as follows: 50 iterations, a batch size of 8, and Adam optimization method, with a learning rate of 10^{-5}.

The Hilbert envelope spectrum images were used as input to the ConvNeXt model, which was trained for 50 epochs to optimize classification performance. As illustrated in Figure 44, the algorithm achieved excellent convergence, with low and stable validation loss indicating strong generalization and no signs of overfitting.

(a) Model accuracy

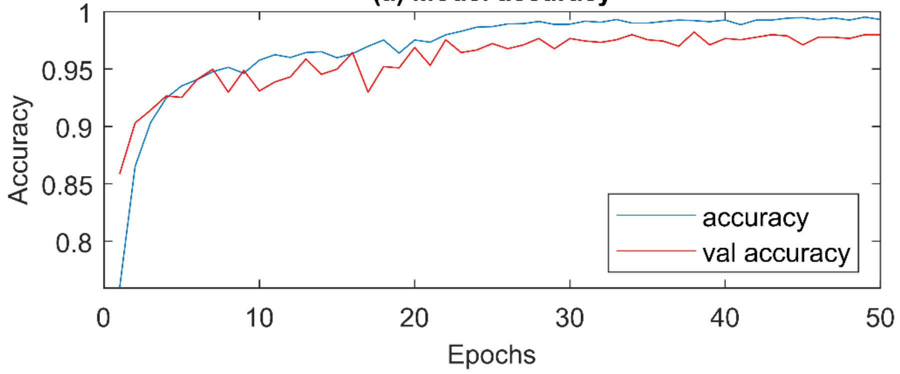

(b) Model loss

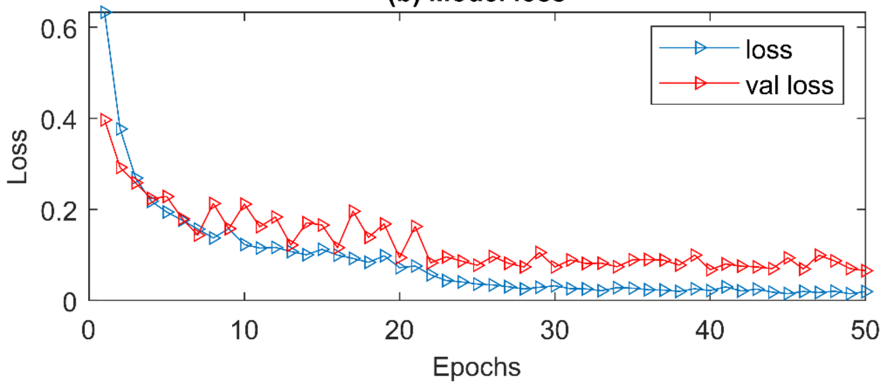

Figure 44 : The accuracy and loss curves of the ConvNeXt model

Following training, the model was evaluated on a separate test set, with the process repeated across five runs under identical conditions. The proposed method consistently delivered outstanding accuracy, achieving an average of 99.04%, with a maximum of 99.44%, a minimum of 98.45%, and a standard deviation of just 0.42%. The confusion matrix for the best trial (Figure 45) demonstrates exceptional classification, showing that outer race defects were identified with 100% precision; only three ball fault instances were misclassified as normal, and one each of inner race and normal condition were misclassified as ball faults. By leveraging the distinct frequency patterns and harmonics present in the Hilbert envelope spectrum, ConvNeXt accurately differentiates between various fault types, learning to recognize the higher frequency modulations typical of ball defects and effectively separating them from inner and outer race faults.

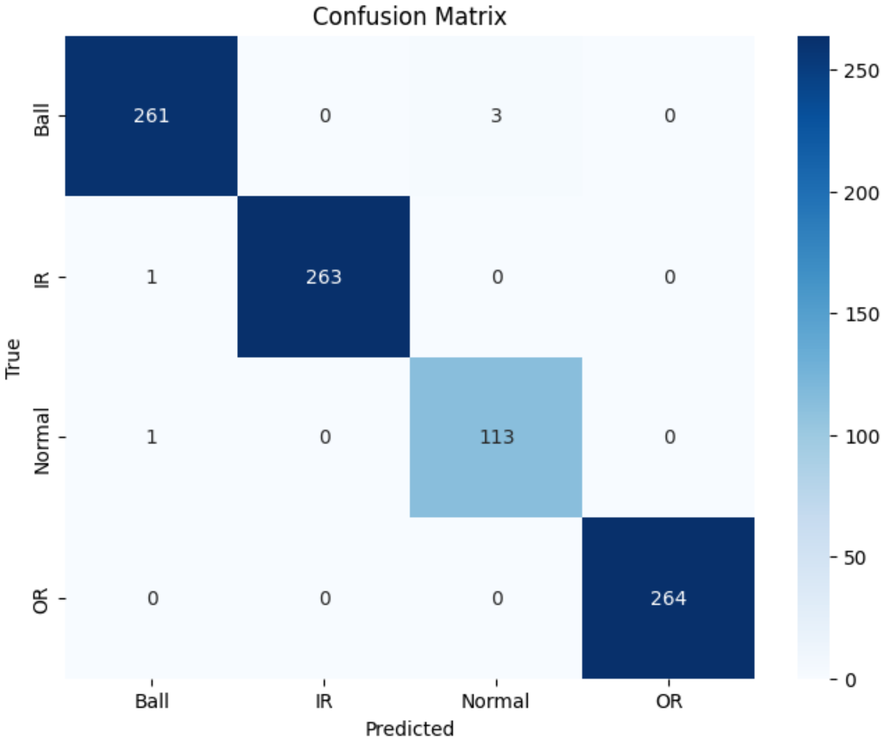

Figure 45 : The confusion matrix of the test dataset

5.6 Comparison with other CNNs and state-of-the-art methods

To rigorously validate the effectiveness of the proposed VMD-AR-ConvNeXt diagnostic approach, a comparative analysis was performed against several state-of-the-art methods and popular CNN architectures from the literature. Competing techniques included VMD with energy entropy and SVM [111], S-Transform with CNN [112], CWT with ResNet50 [113], and widely used architectures such as MobileNetV2 [114], DenseNet121 [115], and ResNet152 [116]. To ensure a fair and meaningful comparison, all models were implemented using the same partitioning and experimental conditions on the Hilbert envelope spectrum dataset.

Table 4 : Comparison of the proposed method with state-of-art approaches and DL architectures

Method	Average accuracy (%)
VMD+energy entropy+SVM [103]	97.40
S-Transform+CNN [104]	83.79
CWT+ResNet50 [105]	96.86
MobileNetV2 [106]	98.91
DenseNet121 [107]	98.81
ResNet152 [108]	98.81
Proposed Method	**99.04**

As summarized in Table 4, the ConvNeXt-based method consistently achieved the highest accuracy (99.04%), outperforming the other approaches by a notable margin. These results highlight the advantages of combining advanced signal decomposition and deep learning, and particularly demonstrate ConvNeXt's strong capacity to extract diagnostic features from time-frequency images for intelligent bearing fault diagnosis.

5.7 Conclusion

In this chapter we have demonstrated the effectiveness and robustness of the proposed intelligent bearing fault diagnosis approach, which integrates advanced signal processing with state-of-the-art deep learning. By combining Variational Mode Decomposition (VMD), Autoregressive (AR) filtering, and the ConvNeXt neural network, the methodology consistently achieved high diagnostic accuracy. Comparative analysis showed that this pipeline not only outperformed traditional machine learning techniques and established CNN-based models but also proved its ability to classify subtle and compound bearing faults with exceptional reliability.

The experiments confirmed ConvNeXt's superior feature extraction capabilities when working with Hilbert envelope spectrum images, leading to strong generalization and minimal overfitting—as reflected in both accuracy metrics and confusion matrices. This method is a promising instrument for practical wind turbine maintenance and broader condition monitoring applications due to its clear interpretability and adaptability.

6

A Study of MPPT control techniques for PV systems under normal and partial shading

6.1 Introduction

Photovoltaic (PV) technology is a cornerstone of modern renewable energy, harnessing the photoelectric effect to convert sunlight directly into electricity through solar panels. PV systems are typically categorized as either grid-connected, where the generated power feeds into the public utility grid, or stand-alone systems, which operate independently to supply specific DC or AC loads. While PV systems offer a sustainable energy source, their efficiency is challenged by the nonlinear electrical characteristics of PV cells—characteristics that are highly sensitive to changing environmental conditions such as solar irradiance, temperature, and especially partial shading.

Under uniform irradiance, the power–voltage (P–V) characteristic of a PV array presents a single, well-defined maximum power point (MPP), enabling conventional maximum power point tracking (MPPT) algorithms to reliably extract peak output. However, real-world conditions often impose partial shading, significantly reducing energy harvest, complicating system design, and giving rise to multiple potential maxima on the P–V curve. These phenomena can undermine efficiency and demand more sophisticated MPPT strategies. Achieving optimal performance, therefore, hinges on robust MPPT algorithms that adaptively guide the PV array to operate at its maximum possible power point under all circumstances.

This chapter provides a comparative simulation study of four MPPT techniques, evaluating their energy extraction capabilities under both normal and partial shading conditions. The analysis aims to clarify the strengths and limitations of each method and guide the selection of MPPT controllers for various PV deployment scenarios.

6.2 Maximum Power Point Tracking Techniques

Maximum Power Point Tracking (MPPT) algorithms are indispensable in photovoltaic (PV) systems to ensure that the maximum available power is continuously extracted under varying environmental conditions such as solar irradiance and temperature. Because the maximum power point (MPP) shifts as these atmospheric variables change, maintaining operation near the MPP is essential for high system efficiency. MPPT algorithms operate by dynamically adjusting the PV array's output voltage to match the optimal value for current conditions. Whether through search-based routines or calculation models, the goal is always to maximize the energy delivered by the PV array.

6.2.1 Conventional Methods

Conventional MPPT strategies are widely adopted due to their simplicity, ease of implementation, and satisfactory performance in most operating scenarios. Chief among these are the Perturb and Observe (P&O), Incremental Conductance (INC), and Hill Climbing methods:

- **Perturb and Observe (P&O)**

The Perturb and Observe (P&O) algorithm stands out as the most widely adopted MPPT technique due to its straightforward design and practical implementation. This method relies on periodically perturbing (either increasing or decreasing) the PV array's terminal voltage or current, then monitoring the resulting change in output power. If the perturbation leads to an increase in output power, the algorithm continues perturbing in the same direction; otherwise, it reverses the direction of the perturbation. This process is repeated until the change in power approaches zero, indicating proximity to the maximum power point (MPP). The principal advantages of P&O are its simplicity and the fact that it does not require any prior knowledge of the PV array's characteristics. However, a notable drawback is that the algorithm continues perturbing even after reaching the MPP, causing the operating point to oscillate around the true maximum. This can result in minor but persistent power losses, especially under steady-state conditions.

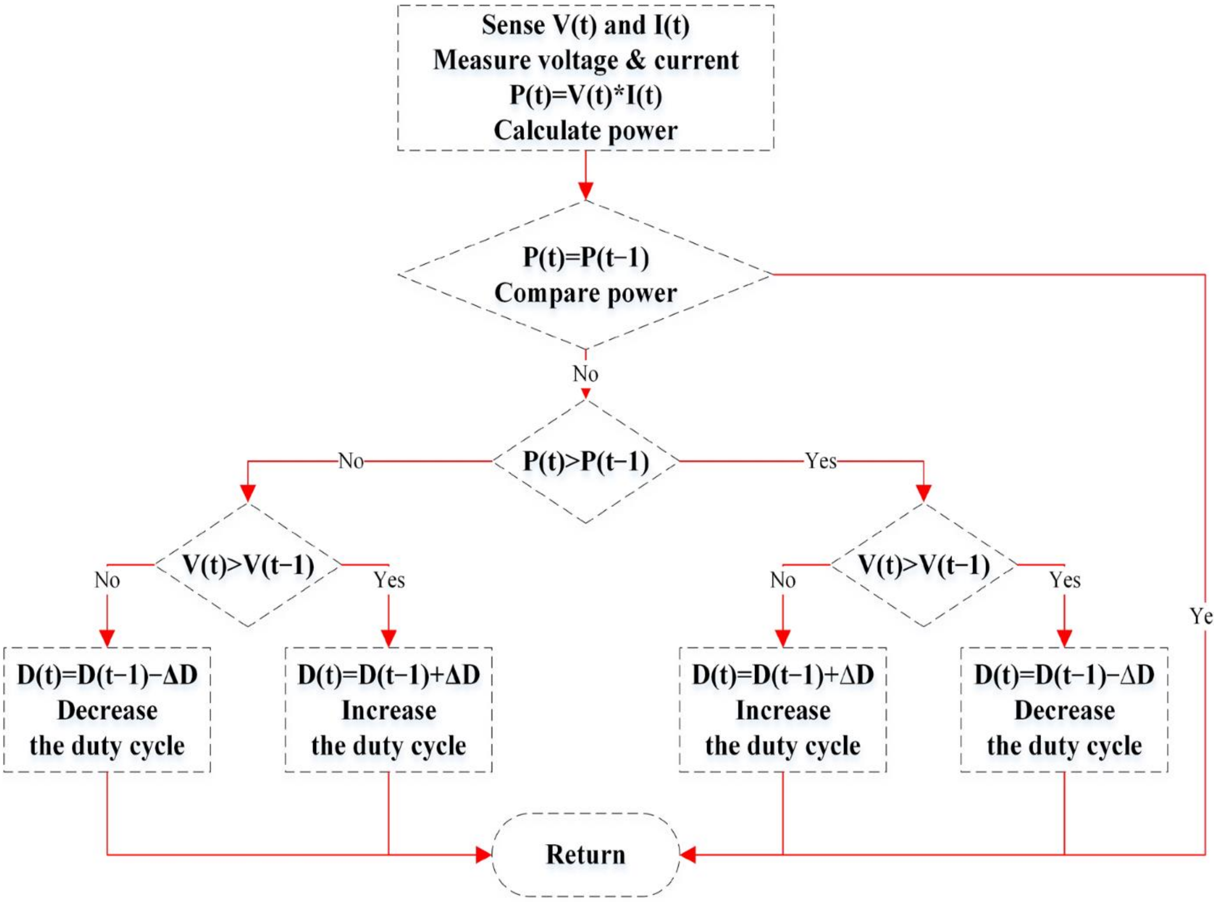

Figure 46 : flowchart of the Perturb and Observe (P&O) algorithm

Figure 46 presents the flowchart of the Perturb and Observe (P&O) algorithm, where V(t) denotes the module voltage, I(t) the module current, and P(t) the output power of the photovoltaic module. In this flowchart, D(t) represents the duty cycle applied to the DC-DC converter and ΔD indicates the incremental change in the duty cycle at each iteration.

• Incremental Conductance Algorithm (INC)

The Incremental Conductance (INC) algorithm is an advanced MPPT strategy that enhances the efficiency of photovoltaic systems by monitoring how the power output changes in relation to voltage. By continuously comparing the incremental conductance (the change in current over the change in voltage) with the instantaneous conductance (current divided by voltage), the algorithm determines whether to increase or decrease the PV array's voltage to converge on the maximum power point. A key advantage of the INC method is its ability to accurately and rapidly track the MPP, even during swiftly fluctuating irradiance and temperature conditions. Nonetheless, like other real-time algorithms, INC can still exhibit some oscillations around the MPP under highly dynamic scenarios. The flowchart depicted in Figure 47 details the step-by-step IC process, where variables such as dP (power change), dV (voltage change), dI (current change), and Vref (reference voltage)

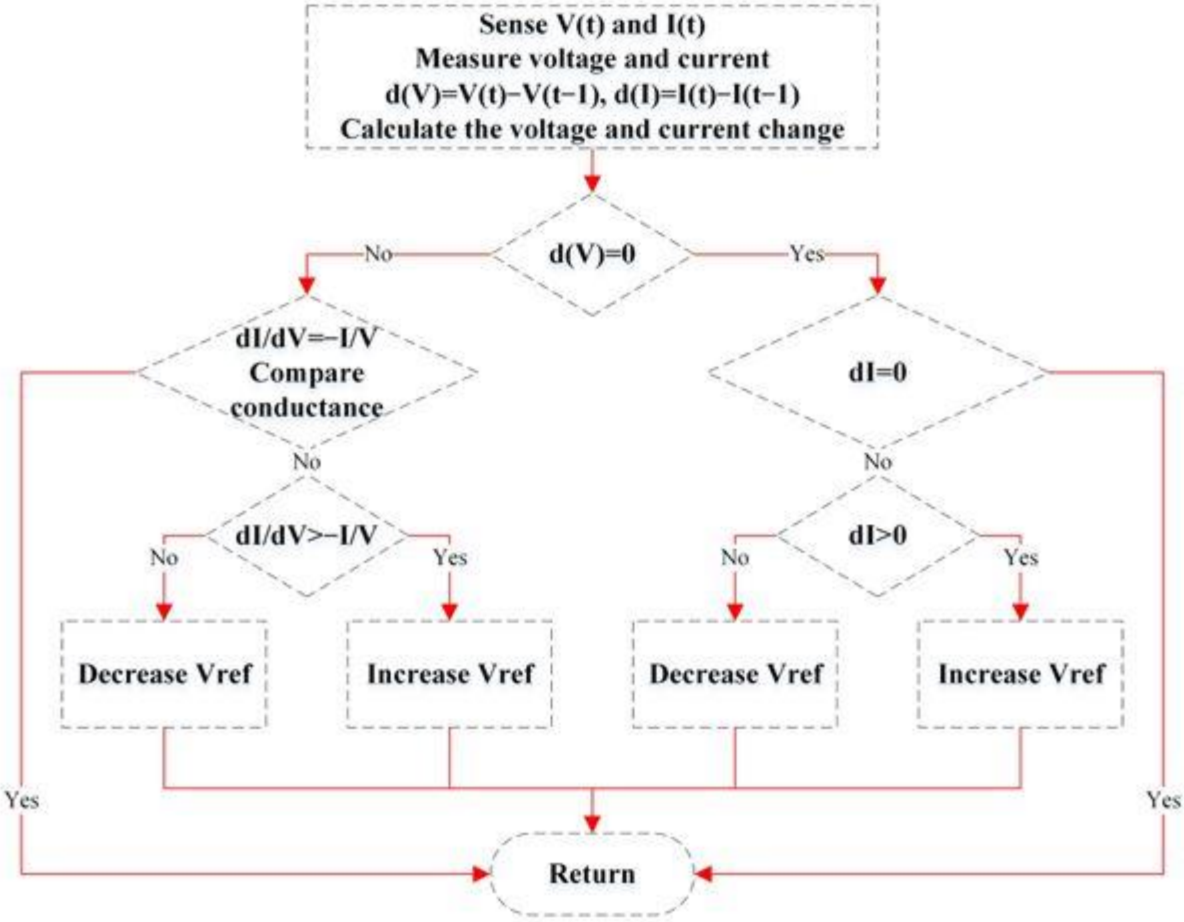

Figure 47 :Flowchart of Incremental Conductance (INC) algorithm

• Hill Climbing Algorithm

The hill climbing algorithm is a foundational method in maximum power point tracking (MPPT) due to its straightforward design and proven effectiveness. In this approach, voltage and current measurements are used to calculate the output power, and the duty cycle of the DC-DC converter is adjusted—either incremented or decremented—based on these calculations. Over several cycles, this iterative adjustment steers the converter towards the maximum power point (MPP). The simplicity of this technique makes it easily understandable and straightforward to implement. However, a main limitation is that the algorithm often introduces oscillations near the MPP and may struggle to converge if the initial duty cycle or step size is poorly chosen, which can result in delays in reaching optimal steady-state performance.

6.2.2 soft computing techniques

Over the past decade, soft computing techniques have become increasingly prominent for addressing complex, nonlinear challenges in maximum power point tracking (MPPT) of photovoltaic systems. These approaches—ranging from fuzzy logic and neural networks to evolutionary algorithms—offer high reliability and faster convergence compared to conventional controllers. Their adoption has been largely motivated by the limitations of traditional methods, such as slow response or diminished accuracy under dynamic conditions. The following section provides a comprehensive review and analysis of various soft computing algorithms that have been successfully implemented to optimize power extraction in PV systems.

- **Fuzzy Logic Controller (FLC)**

The Fuzzy Logic Controller (FLC) is an MPPT algorithm that employs a rule-based system to optimize the power output of photovoltaic systems, effectively managing imprecise and uncertain information. Based on fuzzy logic principles, this approach uses a series of "if–then" rules to map input variables—such as voltage and current—to the corresponding control actions. As outlined in Figure 48, the FLC process consists of three primary stages: fuzzification, which translates numerical measurements into linguistic variables through membership functions; rule evaluation, where these fuzzy inputs are processed using the established rule base; and defuzzification, wherein the resulting linguistic values are converted back into numerical outputs.

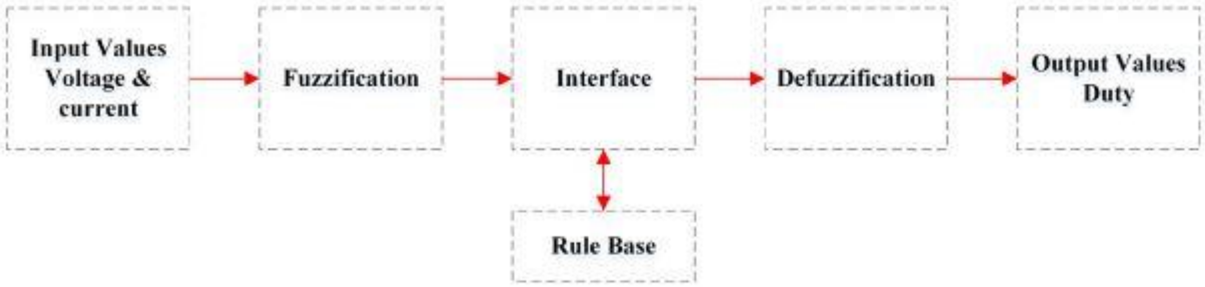

Figure 48 : Flowchart of the Fuzzy Logic Controller (FLC)

The algorithm evaluates not only the present power but also its rate of change from one sampling instant to the next, using error (E) and change in error (ΔE) as main inputs. A key strength of the FLC is its flexibility and robustness in adapting to variable operating conditions, including changes in irradiance and temperature, without requiring an exact mathematical model of the PV module. This adaptability makes it particularly effective in handling complex scenarios, such as partial shading. However, designing and tuning the fuzzy rules is inherently complex and may require specialized knowledge. Ultimately, the control signal for maximizing output power is generated based on these evaluated error variables and their mathematical relationships.

$$E(n) = \frac{P(n) - P(n-1)}{V(n) - V(n-1)}$$

$$\Delta E = E(n) - E(n-1)$$

- **Particle Swarm Optimization (PSO)**

The Particle Swarm Optimization (PSO) algorithm is an advanced MPPT approach for photovoltaic systems, inspired by the collective behavior of natural swarms such as birds flocking or fish schooling. In this technique, showed in Figure 49, a group of candidate solutions, called particles, collaboratively searches for the maximum power point (MPP) by iteratively updating the DC-DC converter's duty cycle based on both individual and social experiences.

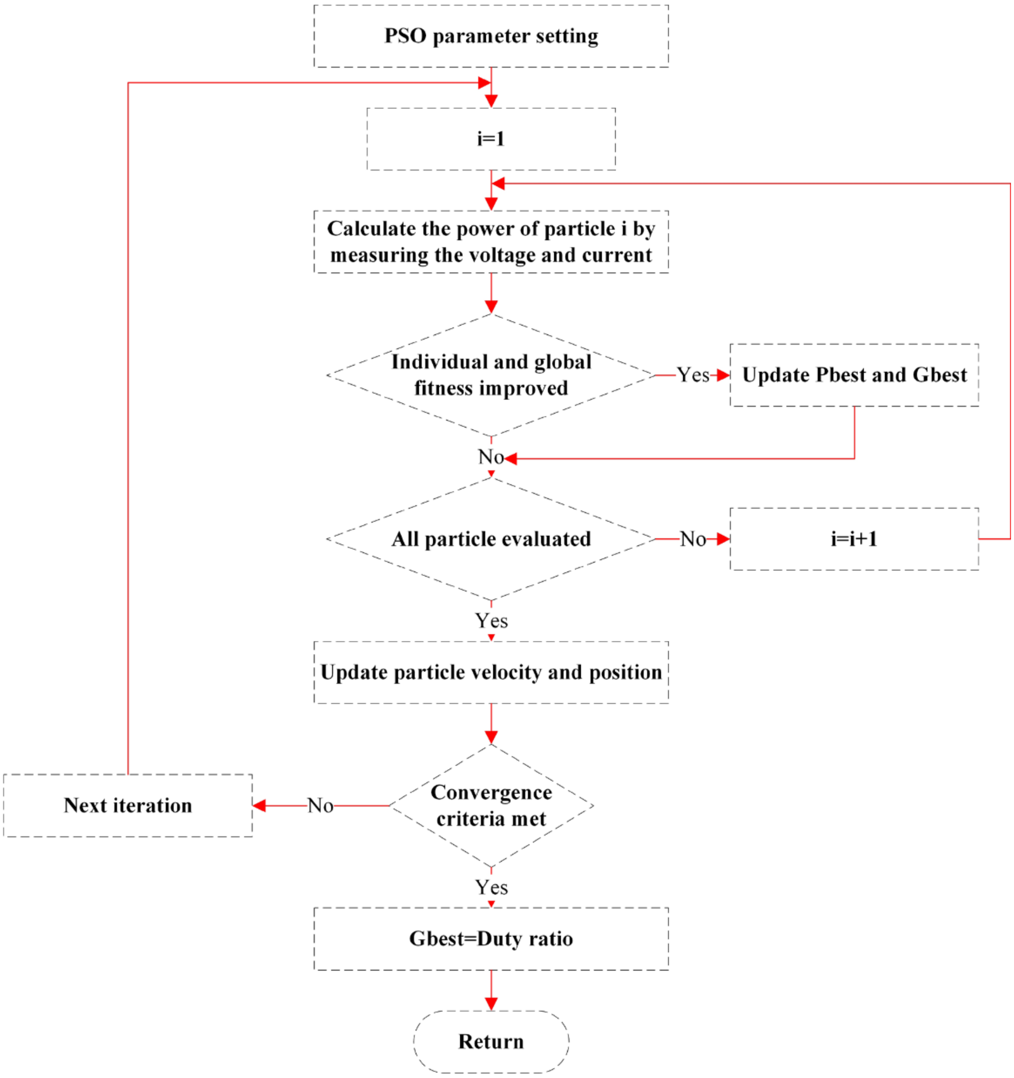

Figure 49 : Flowchart of the Particle Swarm Optimization (PSO)

Each particle adapts its position (personal best, Pbest) using its own performance and that of its peers, collectively converging toward the global best solution (Gbest). As the process progresses, the swarm intelligently navigates the search space until the algorithm outputs the optimal duty cycle and its associated MPP. The primary strength of PSO lies in its ability to efficiently solve complex, nonlinear, and multi-modal optimization problems, making it especially valuable for PV systems exposed to rapidly changing or unpredictable environmental conditions. Nevertheless, the PSO method demands greater computational resources and careful parameter tuning, often resulting in higher implementation complexity compared to more traditional MPPT algorithms.

6.3 SIMULATION AND RESULTS

This section details the development and simulation of a photovoltaic (PV) power conversion system in MATLAB/SIMULINK, focusing on the comparative assessment of four widely studied MPPT algorithms: Fuzzy Logic Control (FLC), Perturb and Observe (P&O), Particle Swarm Optimization (PSO), and Incremental Conductance (INC). The system architecture features a JA SOLAR JAM6-60 250W Monocrystalline panel, Table 5 presents a summary of the PV parameters panel connected to a DC-DC boost converter and a resistive load, forming the testbed for evaluating MPPT performance. Each MPPT technique is implemented within the same simulation environment, enabling direct, fair comparison under different irradiance scenarios—including both uniform sunlight and partial shading conditions. Simulation results are used to analyze the dynamic tracking capabilities, efficiency, and robustness of each algorithm. This methodology underscores the strengths and weaknesses of each approach in maximizing energy extraction, providing a comprehensive foundation for selecting optimal MPPT strategies in real-world PV applications.

Table 5 : JA SOLAR JAM6-60 250W parameters

Power at STC (W)	250
Power at PTC (W)	222.1
Power Density at STC (W / m2)	152.439
Power Density at PTC (W / m2)	135.427
Vmp: Voltage at Max Power (V)	30.96
Imp: Current at Max Power (A)	8.07
Voc: Open Circuit Voltage (V)	37.92
Isc: Short Circuit Current (A)	8.62
Nominal Operating Cell Temp (°C)	48.0

6.3.1 Model design and simulation

The set of models depicted in the provided figures represents the complete system architecture and simulation workflow used in this chapter to analyze and compare Multiple Maximum Power Point Tracking (MPPT) algorithms for photovoltaic (PV) systems under various irradiation scenarios, including partial shading.

The Figure 50 illustrates the PV string configuration under partial shading conditions. Three similar PV modules are connected in series, with each module subjected to different irradiation levels (e.g., 1000, 800, 600 W/m^2).

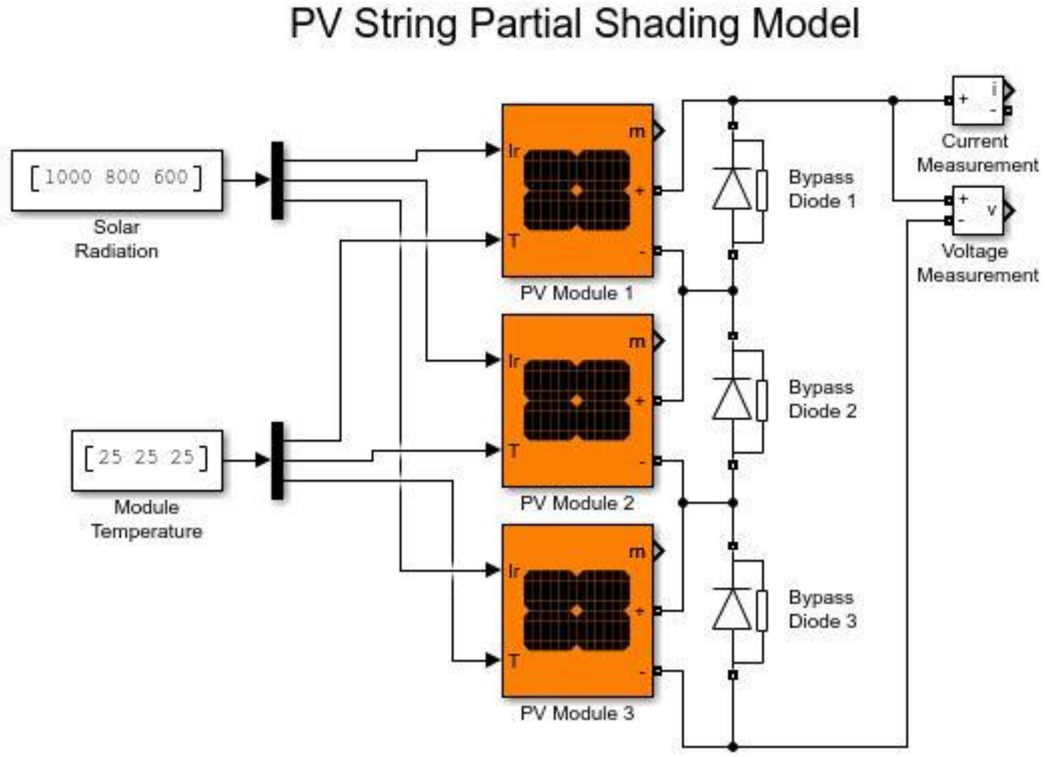

Figure 50 : PV string configuration under partial shading

The figure below presents the MPPT control structure. Voltage (Vpv) and current (Ipv) measurements are used as an entries to four distinct MPPT algorithms—Incremental Conductance (INC), Perturb and Observe (P&O), Particle Swarm Optimization (PSO), and Fuzzy Logic Control (FLC)—, they are individually implemented and can be selected for operation. Each algorithm generates a pulse-width modulation (PWM) signal to control the DC-DC boost converter.

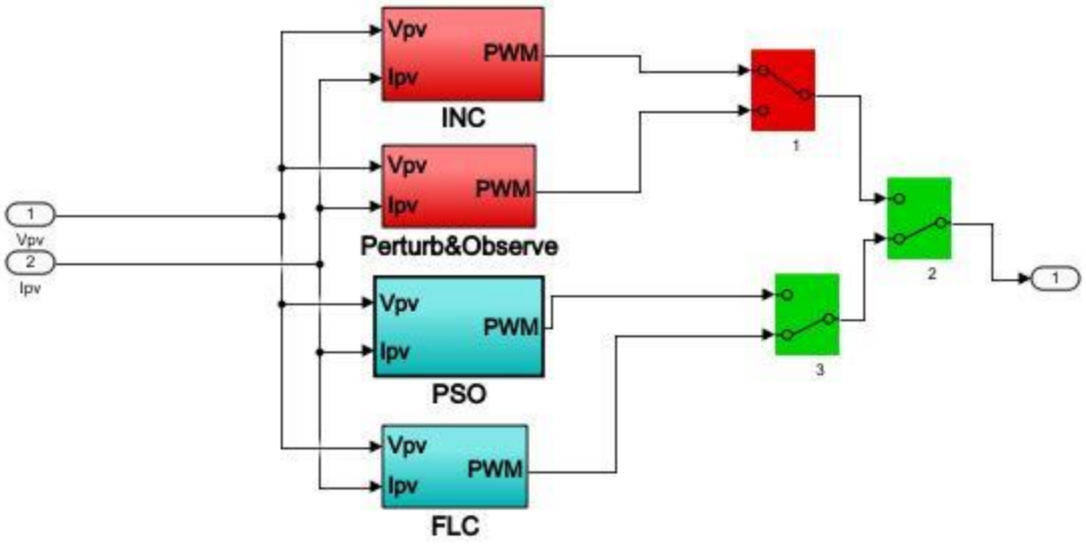

Figure 48b : MPPT control block

The block diagram Figure 51 shows the integrated simulation system in MATLAB/SIMULINK, encompassing the PV source, the boost converter, MPPT block, and the resistive load. The MPPT system receives instantaneous PV voltage and current data, computes the optimal duty cycle, and regulates the converter to ensure the load receives maximum available power.

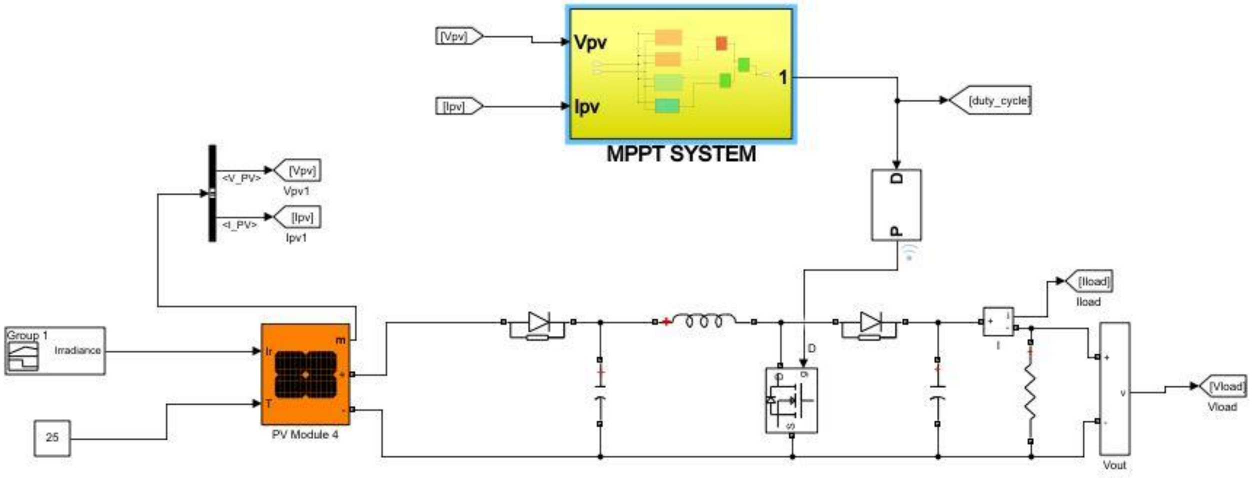

Figure 51 : The proposed SIMULINK model

6.3.2 Results under different radiation

Figure 52 illustrates the time-varying irradiance profile applied during the simulations, Each of the four MPPT techniques—Fuzzy Logic Control (FLC), Perturb and Observe (P&O), Particle Swarm Optimization (PSO), and Incremental Conductance (INC)—was tested under these dynamic irradiance steps. The purpose was to assess the ability of each algorithm to rapidly and accurately track the maximum power point (MPP) of the PV panel as the level of incident solar radiation changed.

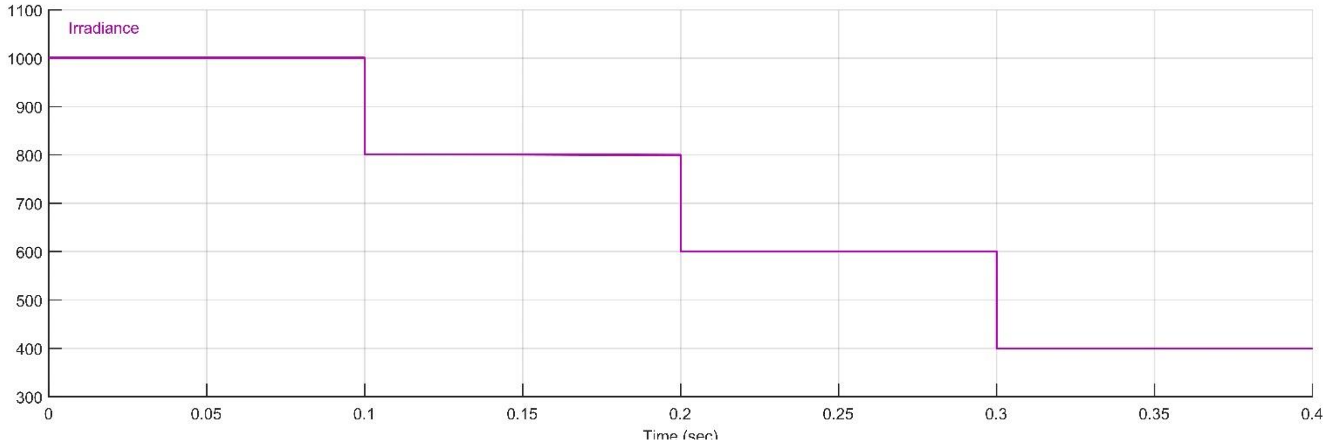

Figure 52 : time-varying irradiance profile

• Simulation using Perturb and Observe technique

The Perturb and Observe (P&O) algorithm, introduced in Section 6.2.1, was implemented within the MATLAB/SIMULINK environment to serve as a benchmark for MPPT control. Figure 53depicts the SIMULINK block, where the P&O logic was embedded via a MATLAB function (the full script is provided in Appendix A.1.), and Figure 54 presents the parameters for the P&O algorithm. This modular implementation accepts PV voltage and current as inputs, runs the real-time P&O MPPT logic, and outputs the appropriate duty cycle to the PWM generator.

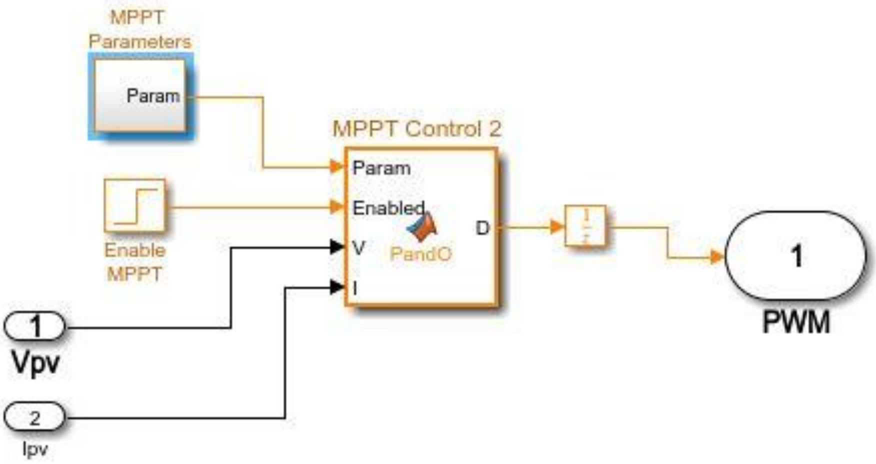

Figure 53 : The SIMULINK block of P&O technique

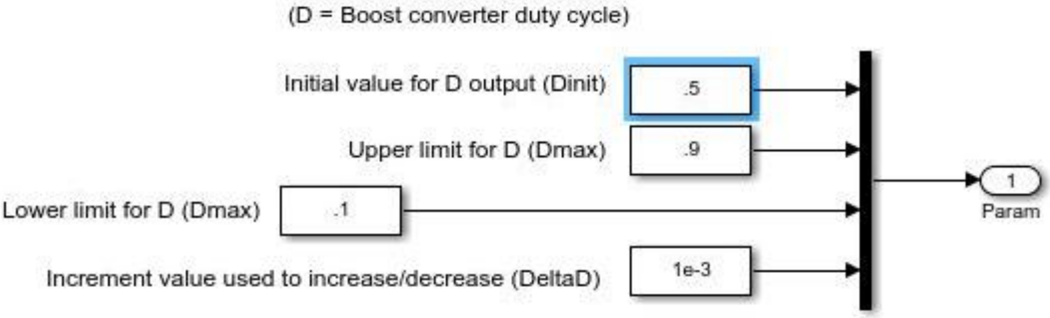

Figure 54 : The parameters for the P&O algorithm

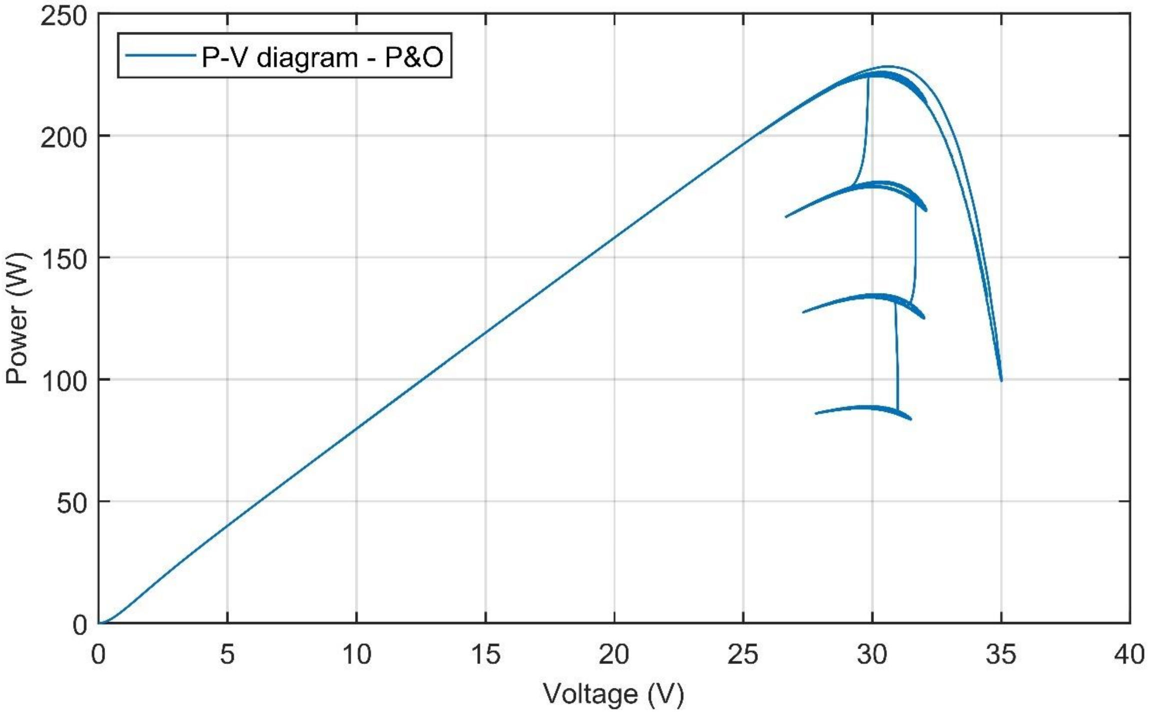

Figure 55 : The P-V diagram of PV module using P&O

The P–V (Power–Voltage) graph (Figure 55) is generated directly from the output of the PV panel using the P&O MPPT algorithm and clearly demonstrates how the maximum power point responds to different irradiance levels. At each plateau, the mean power output in Figure 56 observed for the corresponding irradiance is approximately 215 W for 1000 W/m², 170 W for 800 W/m², 130 W for 600 W/m², and 90 W for 400 W/m².

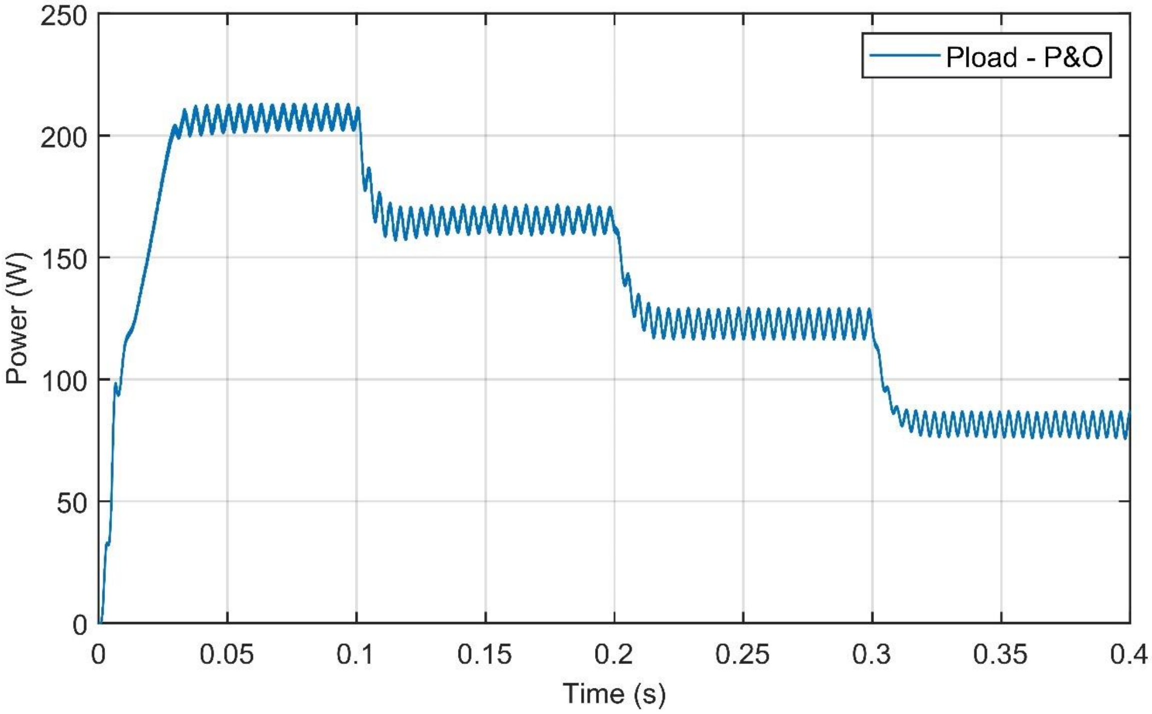

Figure 56 : The output power at the level of the load using P&O technique

These results confirm both the PV system's sensitivity to changes in solar input and the P&O controller’s effectiveness in dynamically tracking the evolving maximum power point as conditions fluctuate. The Figure 56 further corroborates this performance, as power delivered to the load shows prompt adaptation to each drop in irradiance, with characteristic steady-state oscillations around MPP, illustrating the tracking precision and the minor inherent power ripples of the P&O method

- **Simulation using Incremental Conductance**

The Incremental Conductance (INC) algorithm, detailed in Section 6.2.2, was implemented in MATLAB/SIMULINK, as shown in Figure 57. The algorithm operates as a MATLAB function block that uses current and previous PV voltage and current values to compute the optimal duty cycle for the PWM generator, ensuring maximum power tracking. The INC code structure, designed for flexible tuning and evaluation under varying conditions, is fully provided in Appendix A.2.

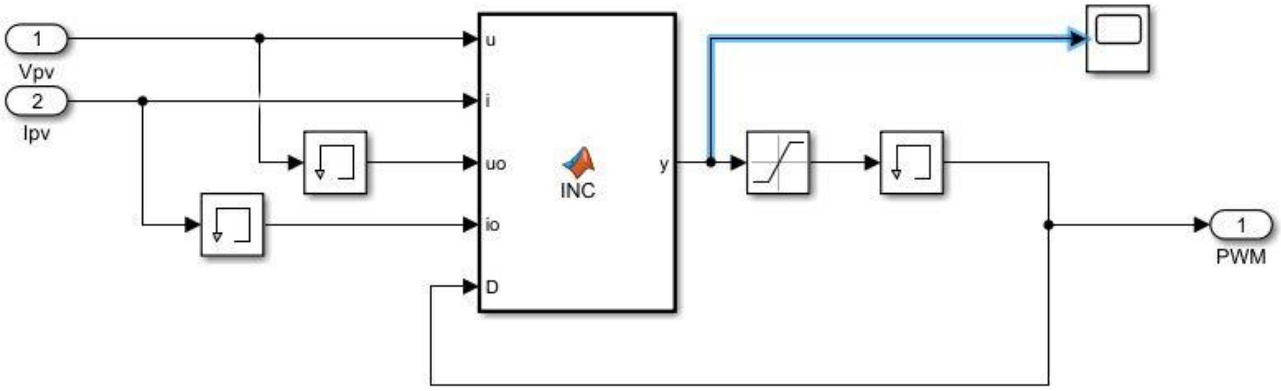

Figure 57 : The SIMULINK block of the INC technique

The P–V characteristic diagram (Figure 58) displays four distinct peaks corresponding to each irradiance level, with the algorithm successfully tracking the maximum power point as irradiance steps from 1000 W/m² (220 W) to 400 W/m² (90 W). The smooth curves indicate stable and effective algorithm performance throughout all test conditions.

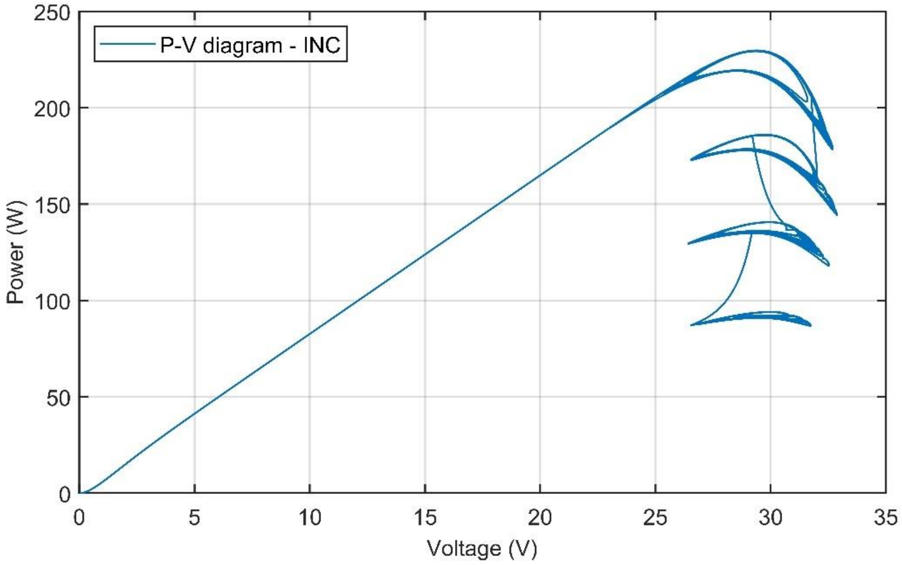

Figure 58 : The P-V diagram of PV module using INC

The output power plot (Figure 59) reveals rapid convergence to each new maximum power point within 20-30 milliseconds after irradiance changes. However, the algorithm exhibits noticeable high-frequency oscillations around each steady-state plateau, with power fluctuating between approximately ±5-8%

of the mean value. Mean power outputs achieved are: 205 W (1000 W/m²), 170 W (800 W/m²), 130 W (600 W/m²), and 85 W (400 W/m²), representing approximately 91% of the panel's 225 W rated capacity.

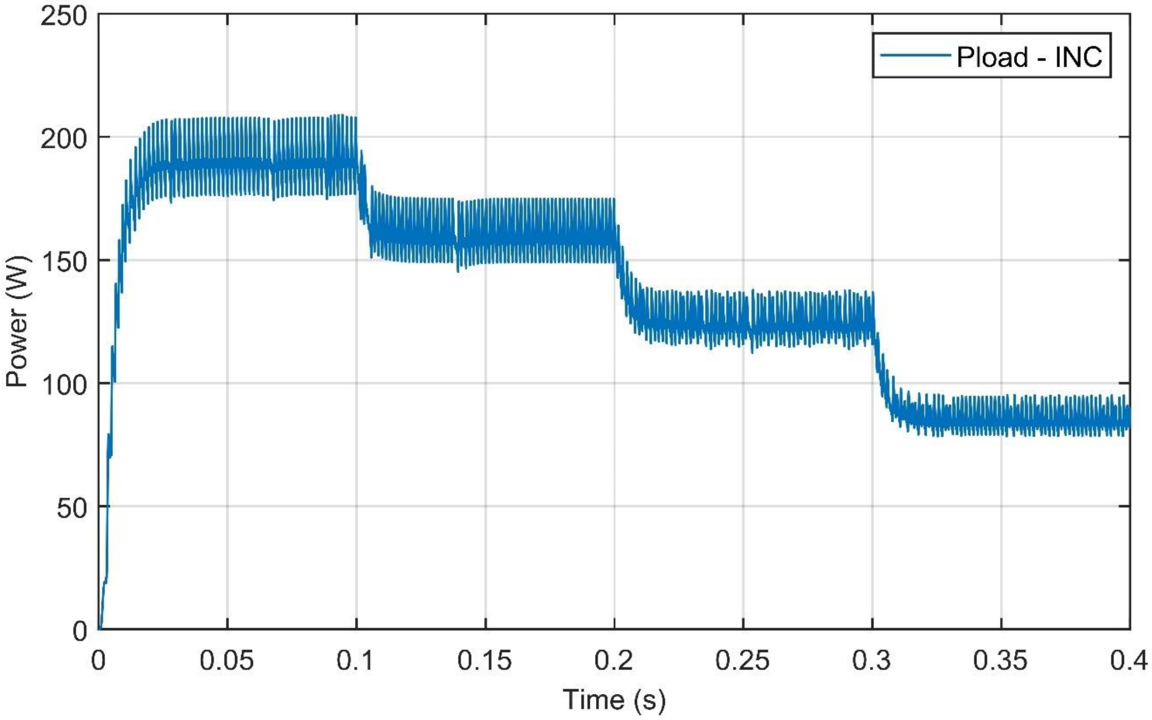

Figure 59 : The output power at the level of the load using INC technique

• Simulation using Particle Swarm Optimization

The block diagram in Figure 60 shows the Particle Swarm Optimization MPPT algorithm implemented in MATLAB/Simulink. Voltage (Vpv) and current (Ipv) measurements from the PV panel are fed into the PSO optimization block, which evaluates instantaneous power and iteratively adjusts particle positions to track the maximum power point. The algorithm outputs a PWM duty cycle signal controlling the DC-DC converter. The complete PSO algorithm implementation code is provided in Appendix A.3.

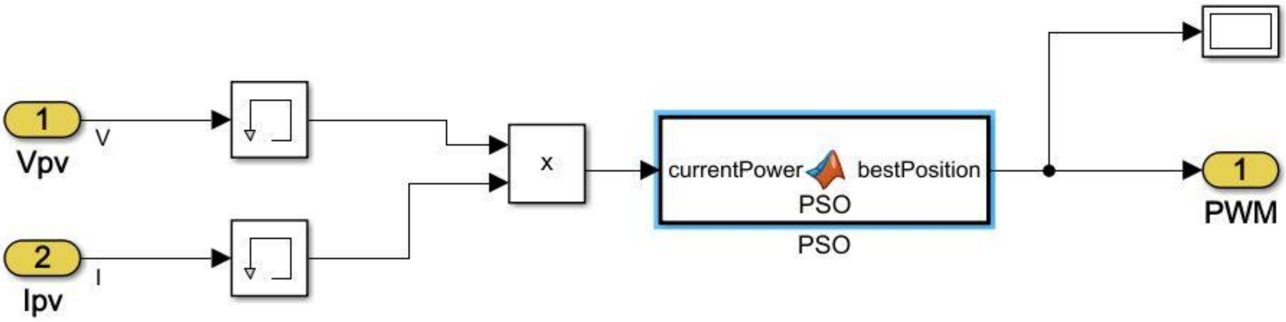

Figure 60 : The SIMULINK block of PSO technique

The following figures (Figure 61, Figure 62) present the simulation results of the Particle Swarm Optimization MPPT algorithm tested under identical conditions with stepwise irradiance variations. As illustrated in the P–V characteristic diagram and temporal load power response, the PSO approach revealed significant limitations in responding to rapid irradiance changes that were not anticipated from conventional algorithm analysis.

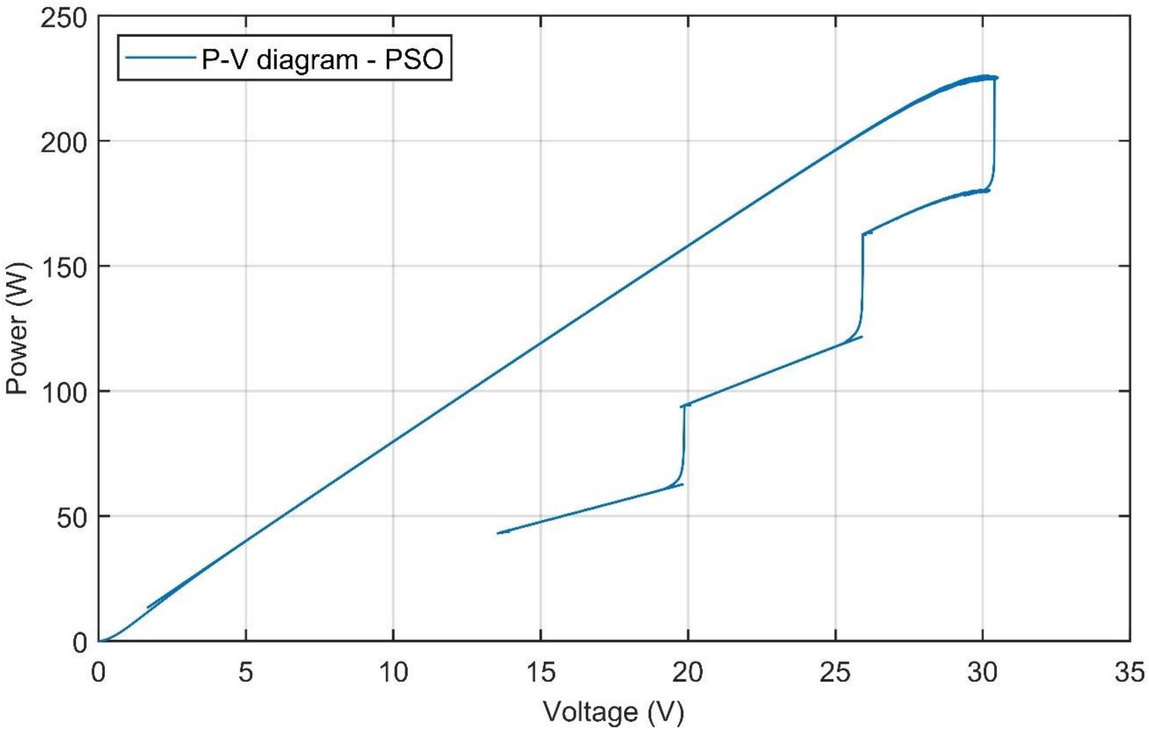

Figure 61 : The P-V diagram of PV module using PSO

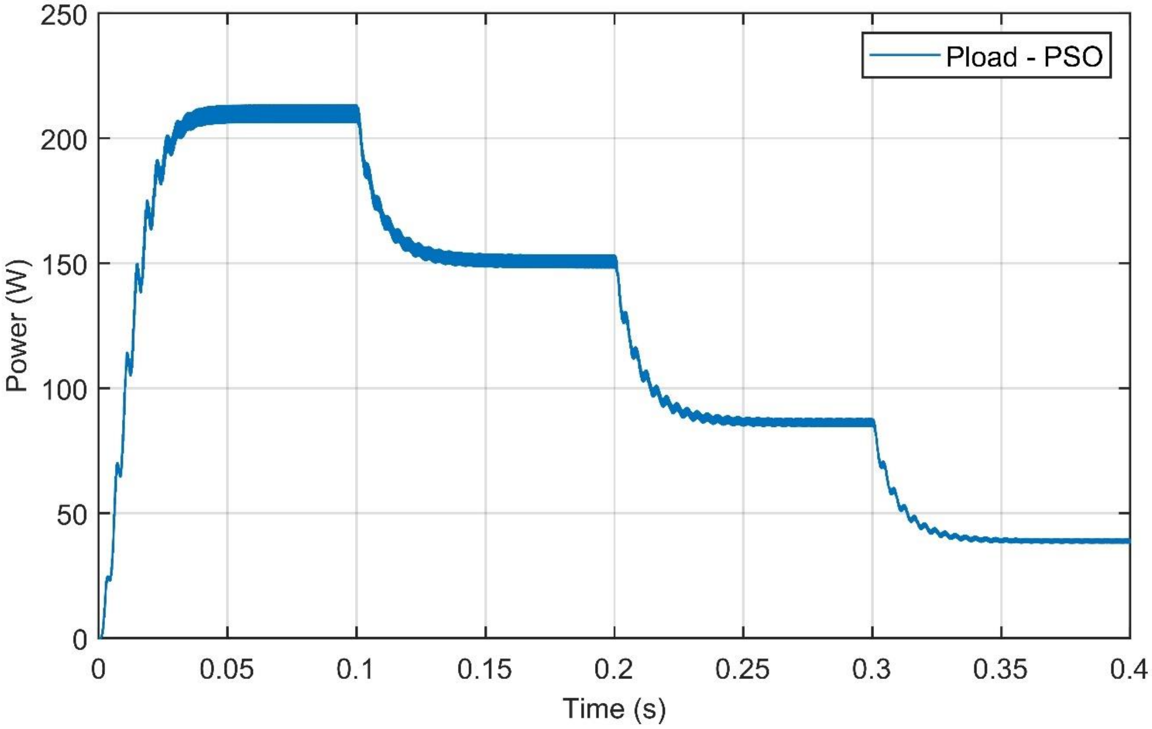

Figure 62 : The output power at the level of the load using PSO technique

The P–V diagram shows the power-voltage trajectory traced by the PSO algorithm across the four irradiance steps. While the 1000 W/m² plateau demonstrates adequate tracking near the expected maximum (approximately 220 W at 30V), the algorithm exhibits markedly degraded performance at lower irradiance levels. At 800 W/m², the operating point fails to reach the true MPP, settling instead at lower power around 155 W. This performance deterioration becomes increasingly pronounced at 600 W/m² (approximately 100 W) and critically severe at 400 W/m² (approximately 40 W). The P–V curve reveals that PSO operates at suboptimal voltage and current points, operating on regions of reduced power gradient rather than at the true maxima.

The temporal power delivery plot vividly demonstrates the algorithmic deficiency. Following each irradiance step decrease, the PSO controller fails to rapidly relocate the maximum power point. Instead of the sharp convergence observed with P&O or INC algorithms, the output power decreases gradually and stabilizes at values well below the theoretical maximum. Notably, after each transition, a prolonged settling period (60-100 milliseconds) occurs before power reaches quasi-steady state, and even then, the achieved level falls substantially short of expectations. At the 400 W/m² level, the power output drops to a meager 40 W, representing only 44% of the expected 90 W that other algorithms achieved

• Simulation using Fuzzy Logic Control

The block diagram (Figure 63) presents the MATLAB/Simulink architecture for the Fuzzy Logic Controller (FLC) MPPT algorithm. The fuzzy control principle is based on two input variables: the error (ER) representing the deviation from the target operating point, and the error change (ΔER) representing the rate of change of this deviation. These variables are derived from voltage (Vpv) and current (Ipv) measurements.

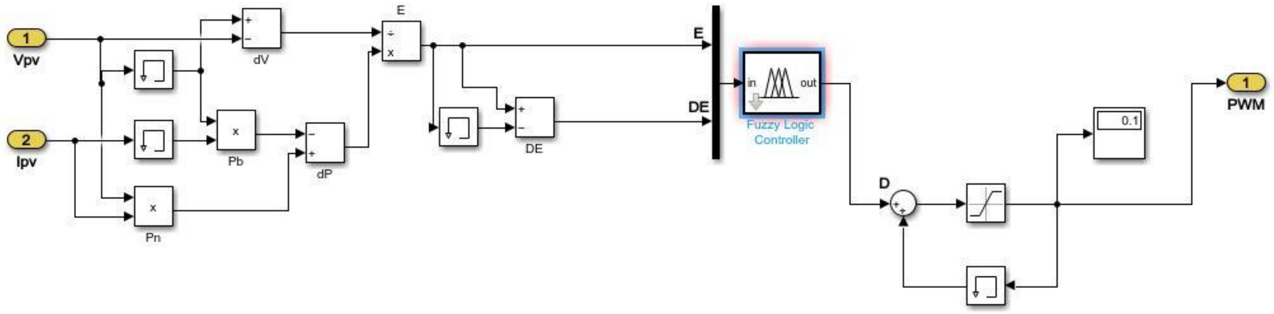

Figure 63 : The SIMULINK block of FLC technique

The fuzzy inference system processes ER and ΔER through membership functions and a truth table of control rules to generate the output variable Δα, which represents the variation of the duty cycle. This dynamic adjustment signal is integrated with feedback control and fed to the PWM generator, enabling the DC-DC converter to adjust its switching frequency and drive the operating point toward the maximum power point. The value of the output variable is determined by the truth table and the continuous evolution of input parameters, allowing adaptive control that responds smoothly to changing environmental conditions.

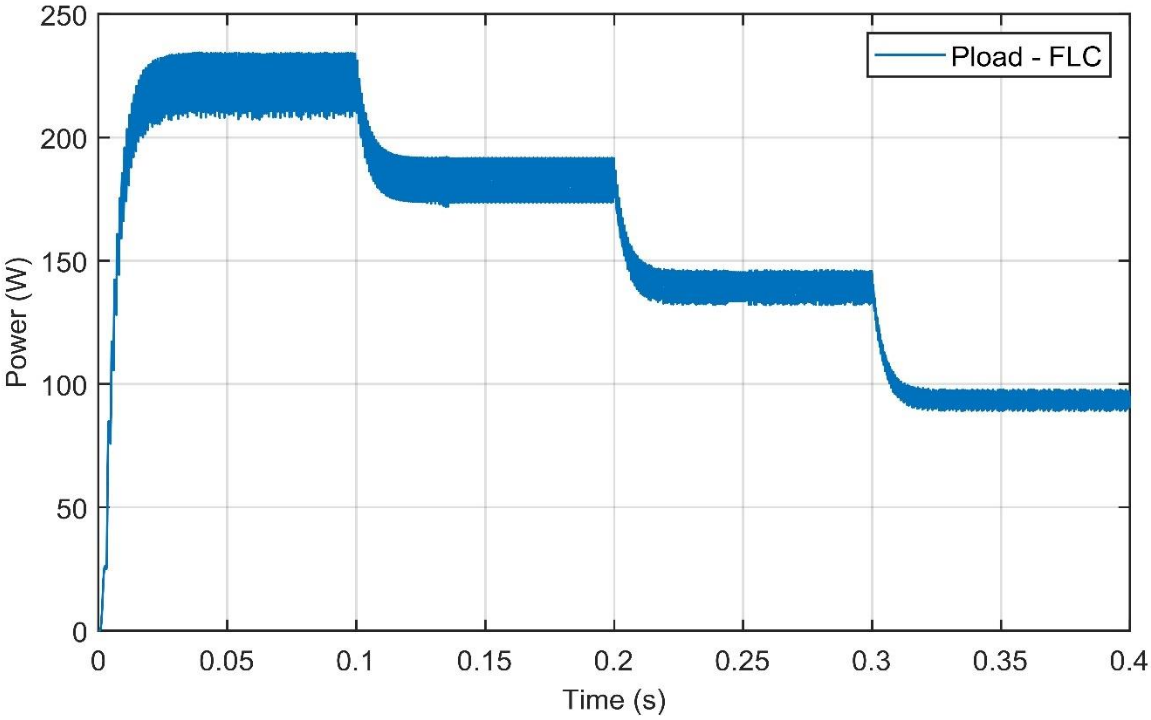

Figure 64 : The output power at the level of the load using FLC technique

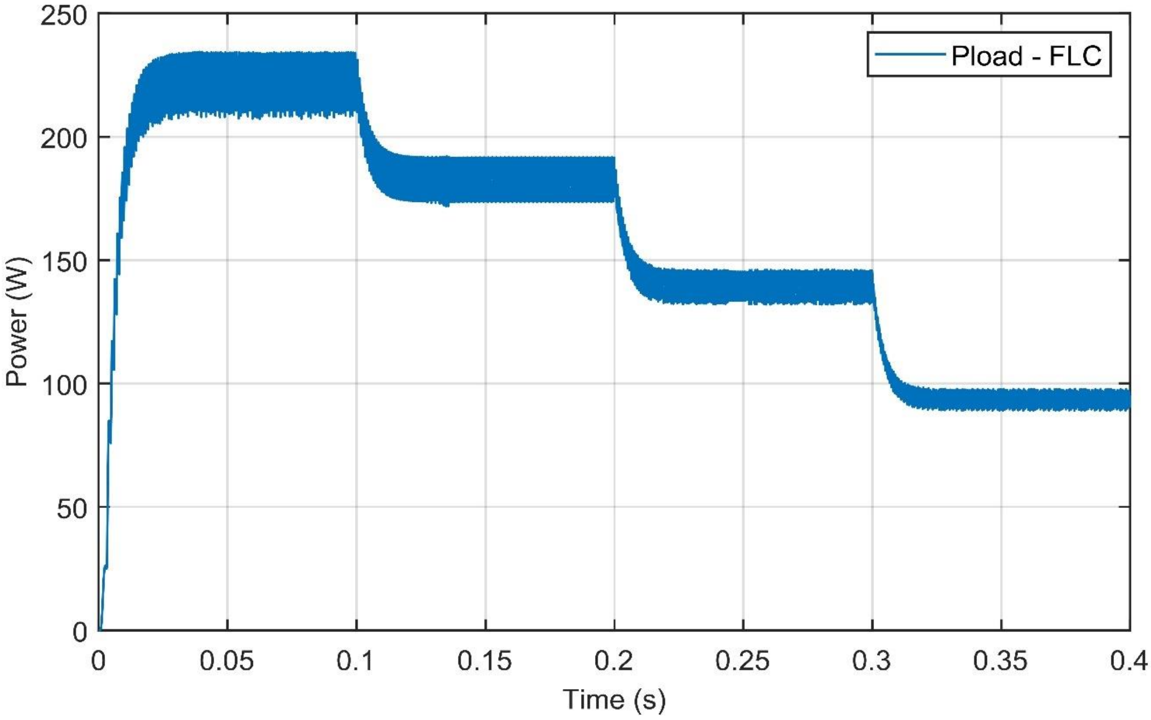

Figure 64 captures the load power response provided by the Fuzzy Logic Controller (FLC) MPPT as the system is subjected to step changes in irradiance. The FLC stands out for its exceptionally rapid transient response, consistently driving the system to the vicinity of the new maximum power point within approximately 30 to 40 milliseconds after each irradiance transition. For each irradiance step (1000, 800, 600, and 400 W/m^2), the mean power output settles at roughly 215 W, 180 W, 135 W, and 90 W, respectively. While the FLC demonstrates superior tracking speed, the steady-state power delivery exhibits a noticeable high-frequency ripple. For instance, at the 1000 W/m^2 plateau, the peak-to-peak power fluctuation is approximately 24 W, translating to a ripple of nearly 11%. This dense chattering is characteristic of this specific FLC tuning. Because the fuzzy inference system is highly sensitive to real-time evaluations of the error (ER) and its rate of change (ΔER), it makes continuous, aggressive micro-adjustments to the duty cycle to maintain the true maximum power point. Overall, this response highlights a fundamental trade-off in MPPT control design. The fuzzy logic method brings rapid adaptation to dynamic environmental conditions, far outpacing the transient response of conventional fixed-step algorithms like P&O or INC. However, this speed comes at the cost of higher steady-state power oscillations. This indicates that while the FLC is highly reactive and robust during transitions, further optimization of the membership functions near the zero-error region would be required to minimize ripple for highly sensitive power quality applications.

6.3.3 Results under partial shading

The following section introduces the comparative study of MPPT algorithms under partial shading conditions

- **Simulation using Perturb and Observe technique**

These two results below show how the classical Perturb and Observe (P&O) MPPT technique behaves when the PV array is affected by partial shading.

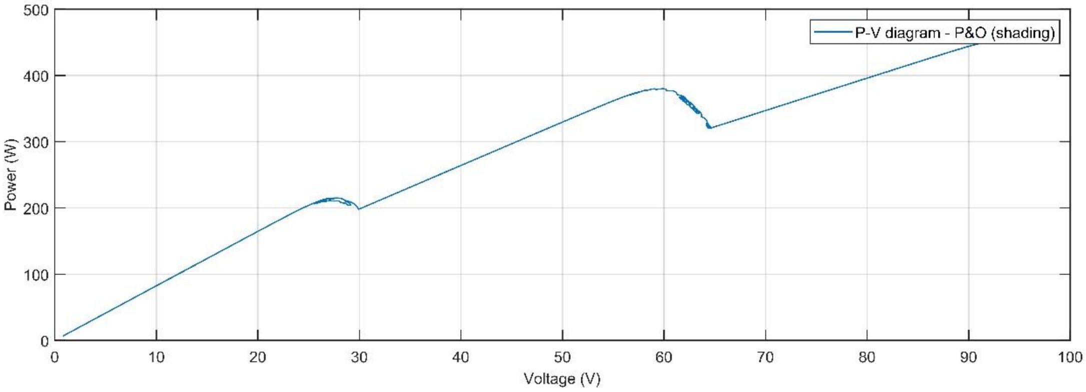

Figure 65 : The P-V diagram of PV module using P&O under partial shading

In the P–V diagram (Figure 65), the characteristic "steps" or local power plateaus caused by uneven irradiance across the PV modules are clearly visible. Interestingly, the P&O algorithm demonstrates the ability to navigate past these local maxima in this specific scenario. Rather than getting trapped at the lower suboptimal plateaus, the controller continues to perturb the operating point until it reaches the vicinity of the Global Maximum Power Point (GMPP) at approximately 440 W. This indicates that the perturbation step size and initialization were sufficient to "jump" across the local peaks to reach the highest available power zone.

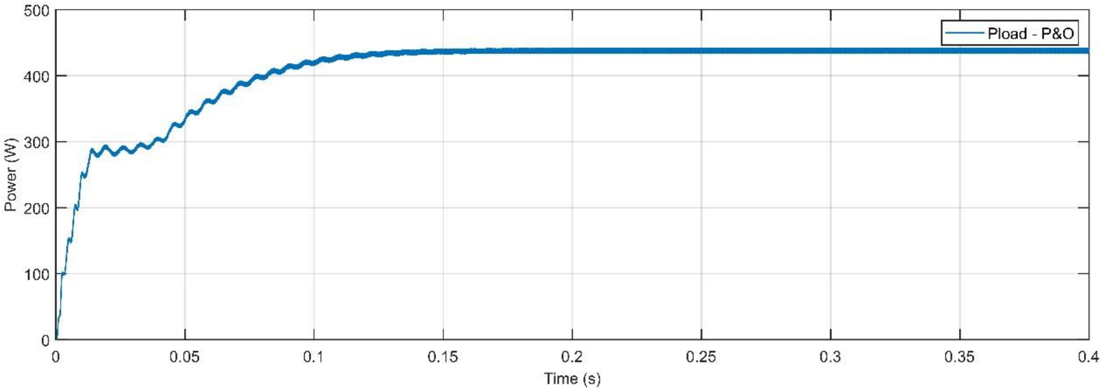

Figure 66: The output power at the level of the load using P&O technique under partial shading

Figure 66 further illustrates this performance over time. After the initial scanning phase, the output power stabilizes near the global peak. However, the primary drawback of the conventional P&O method is evident in the persistent steady-state oscillations around this maximum. While the algorithm successfully avoids leaving significant solar energy "on the table" by reaching the GMPP, these continuous fluctuations around the peak result in a small but measurable loss of efficiency. While effective at finding the global peak in this instance, the result highlights the trade-off between the algorithm's simple tracking logic and its inability to provide a perfectly smooth, ripple-free power output.

- **Simulation using Incremental Conductance**

The experimental results of the INC MPPT under partial shading are presented in Figure 67 and Figure 68. The P–V curve (Figure 67) confirms a multi-peak profile with the global maximum located near 92–95 V, representing a potential power output of approximately 450 W.

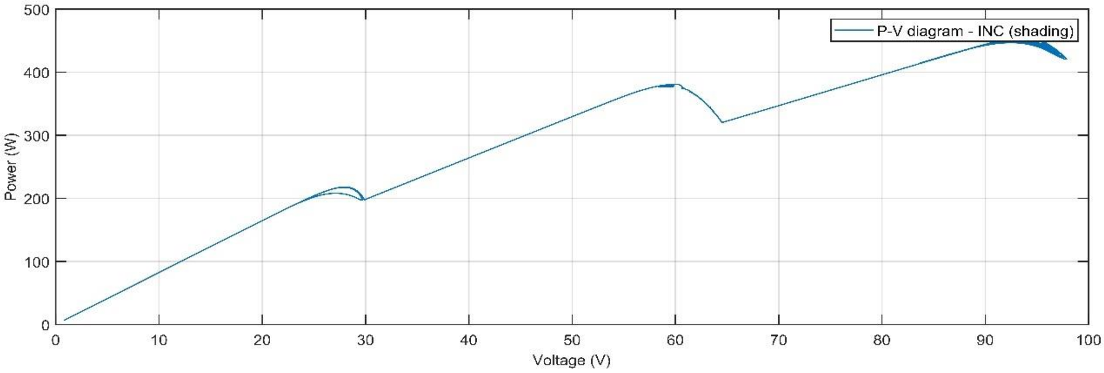

Figure 67 : The P-V diagram of PV module using INC under partial shading

However, the performance of the INC controller in this scenario is characterized by extreme instability. As illustrated in the load-power trace (Figure 68), the algorithm fails to maintain a steady operating point. While the power intermittently reaches the vicinity of the global maximum, the trace is dominated by severe, periodic oscillations and violent transients, with power spikes frequently exceeding 500 W and sudden drops toward lower levels. Rather than settling into a stable tracking state, these continuous excursions indicate that the INC logic is unable to resolve the derivative of power versus voltage effectively under partial shading conditions. Consequently, the mean operating power is compromised by constant fluctuations, suggesting that the standard INC approach lacks the necessary robustness for reliable operation in environments with multiple power peaks.

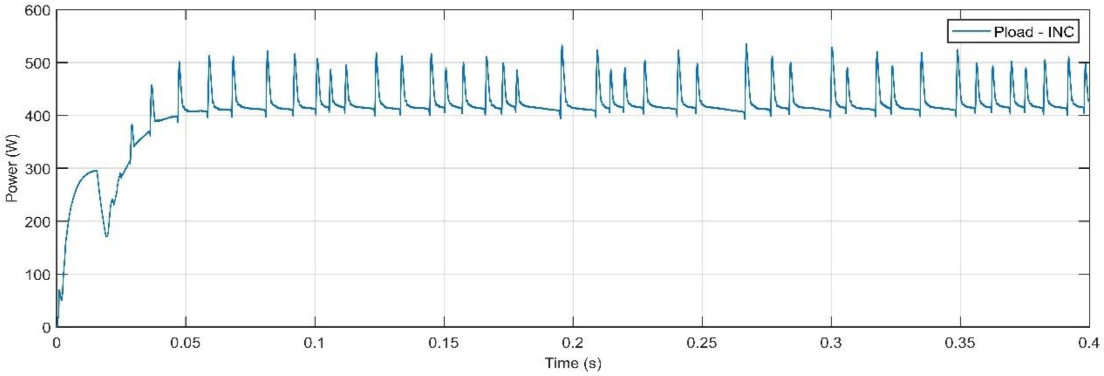

Figure 68 : The output power at the level of the load using INC technique under partial shading

• Simulation using Particle Swarm Optimization

The PSO plots under partial shading show a stable convergence to a local maximum around 370 W even though the P–V curve indicates a higher global peak near to 450 W shown in Figure 69.

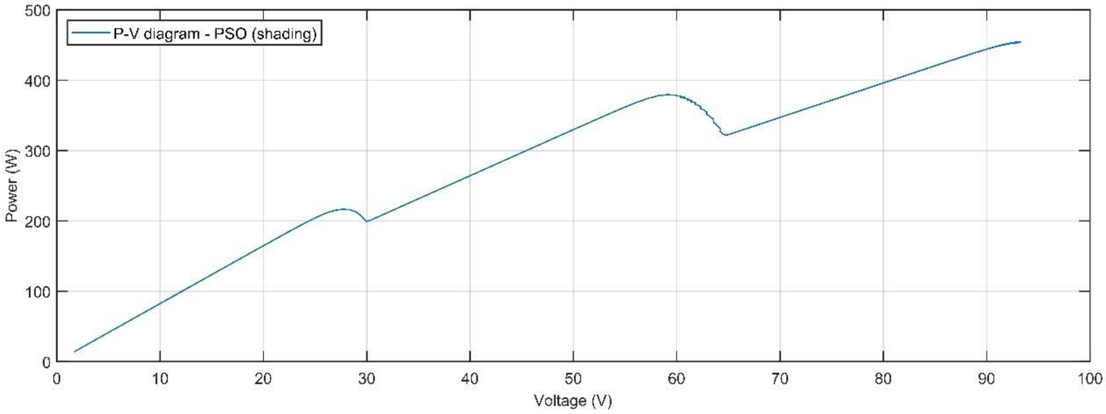

Figure 69 : The P-V diagram of PV module using PSO under partial shading

In the P–V characteristic, several peaks are visible, with the tallest on the far right near 92–95 V at about 450 W, and small ripples around 60–63 V mark the swarm's exploratory steps before settling. This multi-peak profile is consistent with partial shading and indicates that higher power is available than what is achieved in steady operation.

The Figure 70 represents the output power form the converter we can observe that the trace climbs smoothly from startup and levels off near 370 W then stays flat with little oscillation. This steady plateau shows the algorithm has parked on a mid-level peak, delivering consistent but lower power than the global maximum implied by the P–V curve for this case.

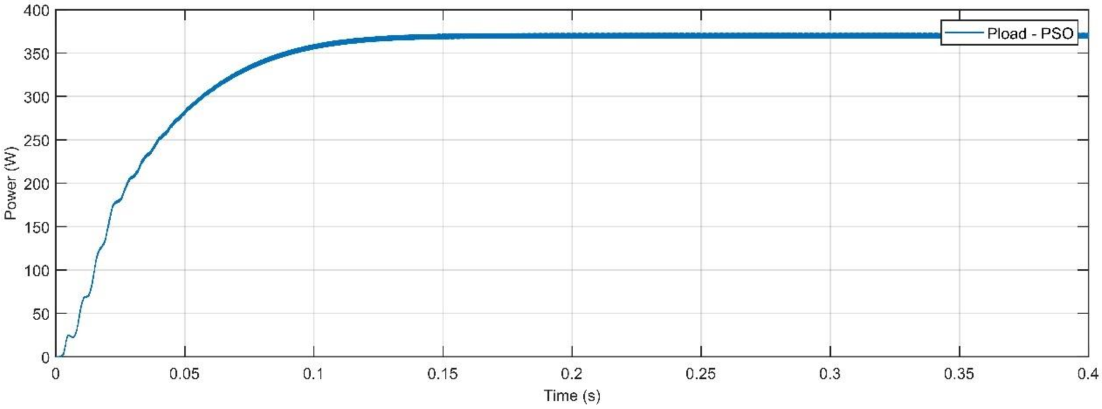

Figure 70 : The output power at the level of the load using PSO technique under partial shading

- ### Simulation using Fuzzy Logic Control

The Figure 71 shows the power output over time as the fuzzy logic controller (FLC) attempts to track the maximum power point. Within the first 0.1 seconds, the power rapidly rises from 0 watts to approximately 270 watts, after which it stabilizes. This quick response indicates that the controller is efficient in locating a peak power point. However, since the system is operating under partial shading conditions, this peak corresponds to a local maximum, not the global one. The controller locks onto this point and maintains it, which suggests good stability but limited adaptability in complex shading scenarios.

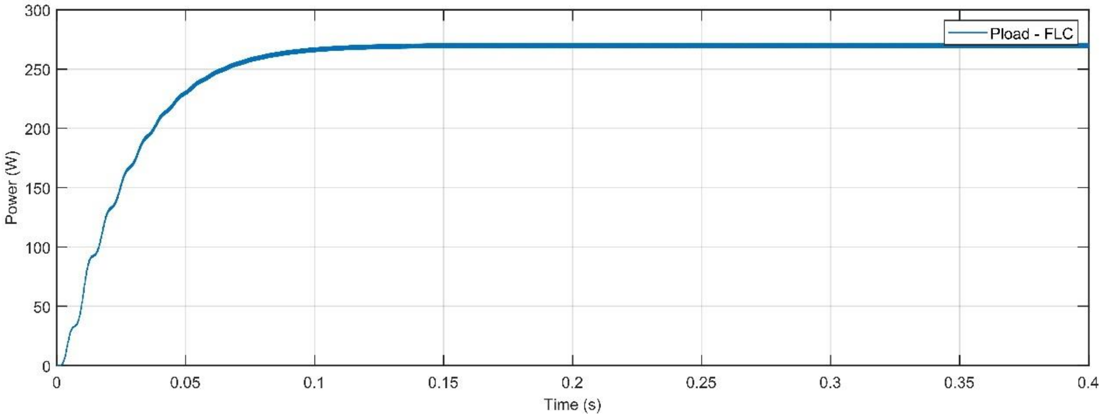

Figure 71 : The output power at the level of the load using FLC technique under partial shading

The Figure 72 plots the power against voltage and reveals the characteristic shape of a partially shaded photovoltaic (PV) array. The curve increases linearly at first, dips around 30 volts, and then continues to rise. This dip represents a local maximum caused by uneven irradiance across the PV modules. The FLC algorithm settles at this local peak, missing the higher global maximum that occurs at a different voltage. This outcome highlights a common challenge in MPPT under partial shading: distinguishing between local and global maxima.

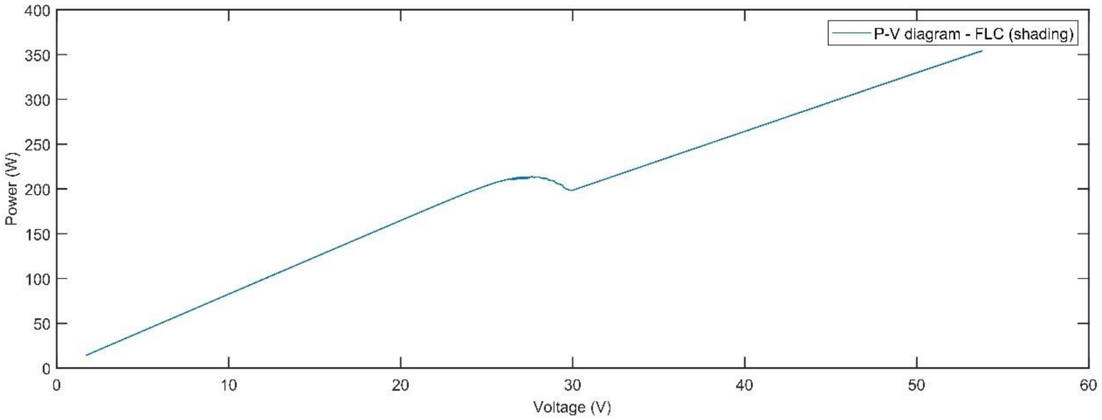

Figure 72 : The P-V diagram of PV module using FLC under partial shading

6.4 Conclusion

Based on comprehensive simulations and analysis, this thesis reveals that each MPPT technique displays unique strengths and weaknesses under varying solar conditions.

Under changing irradiation, Perturb and Observe (P&O) remains reliable for its quick adaptation and simplicity, closely tracking maximum power with characteristic oscillations but minor power ripples. Incremental Conductance (INC) improves upon this with faster convergence and slightly higher accuracy, but exhibits more pronounced oscillations and still doesn't fully reach the theoretical maximum under every scenario. Notably, Particle Swarm Optimization (PSO) excels under stable, high-irradiance conditions but faces significant setbacks when irradiance is low or changes rapidly, falling short of the best possible power point and showing slow, incomplete convergence after each transition. In contrast, Fuzzy Logic Control (FLC) stands out for its rapid dynamic response and high adaptability; it consistently reaches the optimal power point faster than conventional methods. While it exhibits a higher-frequency switching ripple in steady-state, its ability to hold the maximum power point with minimal settling time makes it ideal for environments characterized by fast-changing atmospheric conditions.

Under partial shading conditions (PSC), the performance hierarchy shifts unexpectedly. Simulation results indicate that the classical P&O algorithm, despite its simplicity, is capable of navigating past local maxima to reach the vicinity of the Global Maximum Power Point (GMPP) at approximately 440 W. In contrast, the INC algorithm exhibits critical instability under PSC, characterized by violent power transients and periodic spikes that compromise system reliability.

Furthermore, the results highlight a significant challenge for soft-computing techniques: while PSO and FLC provide the most stable, ripple-free power traces, they are susceptible to premature convergence. In these tests, both algorithms became trapped at local maxima—370 W for PSO and 270 W for FLC—failing to reach the true global peak. This demonstrates that while metaheuristic and adaptive schemes offer superior signal quality, their success under complex shading patterns is highly dependent on rigorous parameter tuning to ensure they maintain sufficient exploration to escape local optima. In summary, for multi-source renewable systems, the trade-off between tracking high power (P&O) and achieving high signal stability (PSO/FLC) remains a central design consideration.

General conclusion and perspectives

This thesis addressed the enhancement of reliability and efficiency in renewable energy systems through intelligent diagnosis and control methods. Two complementary research directions were explored: wind turbine fault diagnosis and photovoltaic system control.

The first part focused on **bearing fault diagnosis in wind turbines**, which represent a major cause of mechanical failure and operational downtime. A hybrid approach combining signal processing, empirical mode decomposition, and machine learning was developed and validated using both experimental and real-world data. The proposed method achieved high accuracy in detecting and classifying bearing defects, demonstrating strong robustness under noise and variable operating conditions. This contribution provides an effective framework for predictive maintenance, reducing costs, and extending the lifespan of wind turbine components.

The second part involved the **study of MPPT control techniques** for photovoltaic systems. Classical and intelligent algorithms were simulated under identical conditions to evaluate their performance. The results confirmed that intelligent approaches such as fuzzy logic provide better tracking stability and power optimization, especially under variable and partially shaded conditions.

Future work can extend this research in several directions.

- Implement real-time monitoring systems based on embedded hardware to validate the proposed fault diagnosis approach in operational wind farms.
- Combine vibration and electrical signal analysis to create multi-sensor diagnostic models.
- Explore deep learning architectures for automatic feature extraction and adaptive fault classification.

- Integrate intelligent MPPT algorithms into hybrid PV–wind systems with energy storage and grid interaction for full-scale testing.

These developments will strengthen the reliability, autonomy, and efficiency of renewable energy systems, contributing to their large-scale deployment in sustainable power networks.

Appendixes

Appendix A.1

```
function D  = PandO(Param, Enabled, V, I)

% MPPT controller based on the Perturb & Observe algorithm.

% D output = Duty cycle of the boost converter (value between 0 and 1)
%
% Enabled input = 1 to enable the MPPT controller
% V input = PV array terminal voltage (V)
% I input = PV array current (A)
%
% Param input:
Dinit = Param(1);  %Initial value for D output
Dmax = Param(2);   %Maximum value for D
Dmin = Param(3);   %Minimum value for D
deltaD = Param(4); %Increment value used to increase/decrease the duty cycle D
% ( increasing D = decreasing Vref )
%

persistent Vold Pold Dold;

dataType = 'double';

if isempty(Vold)
    Vold=0;
    Pold=0;
    Dold=Dinit;
end
P= V*I;
dV= V - Vold;
dP= P - Pold;

if dP ~= 0 & Enabled ~=0
    if dP < 0
        if dV < 0
            D = Dold - deltaD;
        else
            D = Dold + deltaD;
        end
    else
        if dV < 0
            D = Dold + deltaD;
        else
            D = Dold - deltaD;
        end
    end
else D=Dold;
end

if D >= Dmax | D<= Dmin
    D=Dold;
end
```

```
Dold=D;
Vold=V;
Pold=P;
```

Appendix A.2

```
function y = INC(u,i,uo,io,D)
m=0.4;
du=u-uo;
di=i-io;
d=0.05;
if du==0
    if di==0
    m=D;
    else
        if di>0
            m=D-d;
        else
            m=D+d;
        end
    end
else
    if di/du== -(i/u)
    m=D;
    else
        if di/du> -(i/u)
        m=D-d;
        else
            m=D+d;
        end
    end
end
y = m;
end
```

Appendix A.3

```
function bestPosition = PSO(currentPower)
%% PSO Specification
inertiaWeight = 0.0005;        %0.05
cognitiveCoefficient = 1.0908;  %0.3508
socialCoefficient = 1.0908;    %0.3508
numParticles = 4;
positionMin = 0.1;
positionMax = 0.9;

%% Starting Up
persistent particles;
if isempty(particles)
    % Create particles with initial positions and velocities
    particles.positions = linspace(positionMin, positionMax, numParticles);
    particles.velocities = zeros(1, numParticles);
    particles.currentPowers = zeros(1, numParticles);
    particles.bestPositions = zeros(1, numParticles);
```

```
    particles.bestPowers = zeros(1, numParticles);
    particles.globalBestPosition = positionMin;
    particles.currentIndex = 1;
    bestPosition = particles.positions(particles.currentIndex);
else

%% Input Current Power
particles.currentPowers(particles.currentIndex) = currentPower;

%% Update Best Particle's Position
if particles.currentPowers(particles.currentIndex) >
particles.bestPowers(particles.currentIndex)
    particles.bestPositions(particles.currentIndex) =
particles.positions(particles.currentIndex);
    particles.bestPowers(particles.currentIndex) =
particles.currentPowers(particles.currentIndex);
end

%% PSO Algorithm: Update Velocity and Position
particles.velocities(particles.currentIndex) = inertiaWeight *
particles.velocities(particles.currentIndex) ...
    + cognitiveCoefficient * (particles.bestPositions(particles.currentIndex) -
particles.positions(particles.currentIndex)) ...
    + socialCoefficient * (particles.globalBestPosition -
particles.positions(particles.currentIndex));
particles.positions(particles.currentIndex) =
particles.positions(particles.currentIndex) +
particles.velocities(particles.currentIndex);

%% Ensure Position is Within Limits
if particles.positions(particles.currentIndex) <= positionMin
    particles.positions(particles.currentIndex) = positionMin;
end
if particles.positions(particles.currentIndex) >= positionMax
    particles.positions(particles.currentIndex) = positionMax;
end

%% Update Particle Index and Global Best Position
particles.currentIndex = particles.currentIndex + 1;
if particles.currentIndex > numParticles
    [maxPower, maxIndex] = max(particles.bestPowers);
    particles.globalBestPosition = particles.bestPositions(maxIndex);
    particles.currentIndex = 1;
end

%% Output Next Particle Position
bestPosition = particles.positions(particles.currentIndex);

end
```

References

[1] R. K. R. Karduri, “Transitioning to Tomorrow: The Global Journey Towards a Sustainable Energy Economy,” *Int. J. Eng. Res.*, vol. 12, no. 10.

[2] “Is energy from woody biomass positive for the climate? – Bioenergy.” Available: https://www.ieabioenergy.com/iea-publications/faq/woodybiomass/

[3] E. I. Wiloso and R. Heijungs, “Key Issues in Conducting Life Cycle Assessment of Bio-Based Renewable Energy Sources,” in *Life Cycle Assessment of Renewable Energy Sources*, A. Singh, D. Pant, and S. I. Olsen, Eds., London: Springer, 2013, pp. 13–36. doi: 10.1007/978-1-4471-5364-1_2.

[4] “What Is Hydropower & How Does it Work? | Perch Energy.” Available: https://www.perchenergy.com/blog/energy/what-is-hydropower-how-does-it-work

[5] E. Akashie, “Advantages and Disadvantages of Hydroelectric Energy,” Mar. 03, 2022, *Social Science Research Network, Rochester, NY*: 4975373. doi: 10.2139/ssrn.4975373.

[6] “Effects of operation and maintenance costs on the financial sustainability of micro hydropower schemes,” *Sustain. Energy Technol. Assess.*, vol. 83, p. 104651, Nov. 2025, doi: 10.1016/j.seta.2025.104651.

[7] “Power from Geothermal Resources as a Co-product of the Oil and Gas Industry: A Review - PMC.” Available: https://pmc.ncbi.nlm.nih.gov/articles/PMC9670100/

[8] “Trends and prospects of geothermal energy as an alternative source of power: A comprehensive review - PMC.”. Available: https://pmc.ncbi.nlm.nih.gov/articles/PMC9718987/

[9] “Geothermal Energy | Cambridge (CIE) IGCSE Physics Revision Notes 2021,” Save My Exams. Available: https://www.savemyexams.com/igcse/physics/cie/23/revision-notes/1-motion-forces-and-energy/1-8-energy-sources/1-8-4-geothermal-energy/

[10] “Overview of Control and Grid Synchronization for Distributed Power Generation Systems | IEEE Journals & Magazine | IEEE Xplore.” Available: https://ieeexplore.ieee.org/document/1705631

[11] “Pitch-controlled variable-speed wind turbine generation | IEEE Journals & Magazine | IEEE Xplore.” Available: https://ieeexplore.ieee.org/document/903156

[12] S. B. A. Kashem *et al.*, “A Comprehensive Review and the Efficiency Analysis of Horizontal and Vertical Axis Wind Turbines,” *Eur. J. Sustain. Dev. Res.*, vol. 5, no. 3, p. em0163, Jun. 2021, doi: 10.21601/ejosdr/11001.

[13] “Electrical Parts of Wind Turbines,” pp. 269–328, Jan. 2012, doi: 10.1016/B978-0-08-087872-0.00211-0.

[14] F. Blaabjerg, F. Iov, Z. Chen, and K. Ma, “Power electronics and controls for wind turbine systems,” in *2010 IEEE International Energy Conference*, Manama, Bahrain: IEEE, Dec. 2010,

pp. 333–344. doi: 10.1109/ENERGYCON.2010.5771701.

[15] J. D. M. De Kooning, K. Stockman, J. De Maeyer, A. Jarquin-Laguna, and L. Vandevelde, "Digital Twins for Wind Energy Conversion Systems: A Literature Review of Potential Modelling Techniques Focused on Model Fidelity and Computational Load," *Processes*, vol. 9, no. 12, p. 2224, Dec. 2021, doi: 10.3390/pr9122224.

[16] "Modelling and control of variable-speed multi-pole permanent magnet synchronous generator wind turbine - Hansen - 2008 - Wind Energy - Wiley Online Library." Available: https://onlinelibrary.wiley.com/doi/10.1002/we.278

[17] K. Patil and B. Mehta, "Modeling and control of variable speed wind turbine with permanent magnet synchronous generator," in *2014 International Conference on Advances in Green Energy (ICAGE)*, Dec. 2014, pp. 258–264. doi: 10.1109/ICAGE.2014.7050174.

[18] "Solar Energy: Applications, Trends Analysis, Bibliometric Analysis and Research Contribution to Sustainable Development Goals (SDGs)." Available: https://www.mdpi.com/2071-1050/15/2/1418

[19] "Review of photovoltaic and concentrated solar technologies including their performance, reliability, efficiency and storage," *Results Eng.*, vol. 25, p. 104424, Mar. 2025, doi: 10.1016/j.rineng.2025.104424.

[20] V. Benda and L. Černá, "PV cells and modules – State of the art, limits and trends," *Heliyon*, vol. 6, no. 12, p. e05666, Dec. 2020, doi: 10.1016/j.heliyon.2020.e05666.

[21] "Challenges and Approaches to Extending the Safe Operational Life of Future Renewable Energy Infrastructure - IOPscience." Available: https://iopscience.iop.org/article/10.1149/MA2024-02171702mtgabs

[22] Q. Cao, H. Su, and X. Wang, "Research on Predictive Maintenance Strategy of Wind Turbine Based on Generalized Stochastic Differential Equation Model," in *2021 IEEE 2nd China International Youth Conference on Electrical Engineering (CIYCEE)*, Dec. 2021, pp. 1–5. doi: 10.1109/CIYCEE53554.2021.9676783.

[23] Z. Liu and L. Zhang, "A review of failure modes, condition monitoring and fault diagnosis methods for large-scale wind turbine bearings," *Measurement*, vol. 149, p. 107002, Jan. 2020, doi: 10.1016/j.measurement.2019.107002.

[24] W. Qiao and D. Lu, "A Survey on Wind Turbine Condition Monitoring and Fault Diagnosis—Part I: Components and Subsystems," *IEEE Trans. Ind. Electron.*, vol. 62, no. 10, pp. 6536–6545, Oct. 2015, doi: 10.1109/TIE.2015.2422112.

[25] W. Qiao and D. Lu, "A Survey on Wind Turbine Condition Monitoring and Fault Diagnosis—Part II: Signals and Signal Processing Methods," *IEEE Trans. Ind. Electron.*, vol. 62, no. 10, pp. 6546–6557, Oct. 2015, doi: 10.1109/TIE.2015.2422394.

[26] Z. Gao and X. Liu, "An Overview on Fault Diagnosis, Prognosis and Resilient Control for Wind Turbine Systems," *Processes*, vol. 9, no. 2, p. 300, Feb. 2021, doi: 10.3390/pr9020300.

[27] "An Overview on Fault Diagnosis, Prognosis and Resilient Control for Wind Turbine Systems."

Available: https://www.mdpi.com/2227-9717/9/2/300

[28] J. P. Salameh, S. Cauet, E. Etien, A. Sakout, and L. Rambault, "Gearbox condition monitoring in wind turbines: A review," *Mech. Syst. Signal Process.*, vol. 111, pp. 251–264, Oct. 2018, doi: 10.1016/j.ymssp.2018.03.052.

[29] H. Gu, W. Y. Liu, Q. W. Gao, and Y. Zhang, "A review on wind turbines gearbox fault diagnosis methods," *J. Vibroengineering*, vol. 23, no. 1, pp. 26–43, Feb. 2021, doi: 10.21595/jve.2020.20178.

[30] "59111.pdf." Available: https://docs.nrel.gov/docs/fy13osti/59111.pdf

[31] C. Dao, B. Kazemtabrizi, and C. Crabtree, "Wind turbine reliability data review and impacts on levelised cost of energy," *Wind Energy*, vol. 22, no. 12, pp. 1848–1871, 2019, doi: 10.1002/we.2404.

[32] "Wind turbine reliability data review and impacts on levelised cost of energy - Dao - 2019 - Wind Energy - Wiley Online Library." Available: https://onlinelibrary.wiley.com/doi/full/10.1002/we.2404

[33] L. Fadda Mohamed, "Contribution à la modélisation et au diagnostic intelligent des systèmes de production d'énergie électrique à base d'énergies renouvelables," Thesis, 2017. https://dspace.univ-guelma.dz/jspui/handle/123456789/6179

[34] W.-C. Tsao, Y.-F. Li, D. D. Le, and M.-C. Pan, "An insight concept to select appropriate IMFs for envelope analysis of bearing fault diagnosis," *Measurement*, vol. 45, no. 6, pp. 1489–1498, Jul. 2012, doi: 10.1016/j.measurement.2012.02.030.

[35] D. K. Appana, A. Prosvirin, and J.-M. Kim, "Reliable fault diagnosis of bearings with varying rotational speeds using envelope spectrum and convolution neural networks," *Soft Comput.*, vol. 22, no. 20, pp. 6719–6729, Oct. 2018, doi: 10.1007/s00500-018-3256-0.

[36] "Incorporating Machine Learning into Vibration Detection for Wind Turbines - Vives - 2022 - Modelling and Simulation in Engineering - Wiley Online Library." Available: https://onlinelibrary.wiley.com/doi/10.1155/2022/6572298

[37] "Wind Turbines Gearbox - Consequences of Failure | Pall Corporation." Available: https://www.pall.com/en/decarbonization/blog/wind-turbine-gearbox-failures.html

[38] H. Peng, S. Li, L. Shangguan, Y. Fan, and H. Zhang, "Analysis of Wind Turbine Equipment Failure and Intelligent Operation and Maintenance Research," *Sustainability*, vol. 15, no. 10, p. 8333, Jan. 2023, doi: 10.3390/su15108333.

[39] C. Dao, B. Kazemtabrizi, and C. Crabtree, "Wind turbine reliability data review and impacts on levelised cost of energy," *Wind Energy*, vol. 22, no. 12, pp. 1848–1871, 2019, doi: 10.1002/we.2404.

[40] C. D. Dao, B. Kazemtabrizi, C. J. Crabtree, and P. J. Tavner, "Integrated condition-based maintenance modelling and optimisation for offshore wind turbines," *Wind Energy*, vol. 24, no. 11, pp. 1180–1198, 2021, doi: 10.1002/we.2625.

[41] "Offshore Wind Turbines: Reliability, availability and maintenance | IET Digital Library." Available: https://digital-library.theiet.org/doi/book/10.1049/pbrn013e

[42] B. Le and J. Andrews, “Modelling wind turbine degradation and maintenance: Modelling wind turbine degradation and maintenance,” *Wind Energy*, vol. 19, no. 4, pp. 571–591, Apr. 2016, doi: 10.1002/we.1851.

[43] J. Vives, “Monitoring and Detection of Wind Turbine Vibration with KNN-Algorithm,” *J. Comput. Commun.*, vol. 10, no. 7, pp. 1–12, Jul. 2022, doi: 10.4236/jcc.2022.107001.

[44] Y. Sun, J. Kang, L. Sun, P. Jin, and X. Bai, “Condition-based maintenance for the offshore wind turbine based on long short-term memory network,” *Proc. Inst. Mech. Eng. Part O J. Risk Reliab.*, vol. 236, no. 4, pp. 542–553, Aug. 2022, doi: 10.1177/1748006X20965434.

[45] X. Chesterman, T. Verstraeten, P.-J. Daems, A. Nowé, and J. Helsen, “Pattern mining based data fusion for wind turbine condition monitoring,” *J. Phys. Conf. Ser.*, vol. 2507, no. 1, p. 012001, May 2023, doi: 10.1088/1742-6596/2507/1/012001.

[46] R. D. Frederiksen, G. Bocewicz, G. Radzki, Z. Banaszak, and P. Nielsen, “Cost-Effectiveness of Predictive Maintenance for Offshore Wind Farms: A Case Study,” *Energies*, vol. 17, no. 13, p. 3147, Jun. 2024, doi: 10.3390/en17133147.

[47] A. Avižienis, J.-C. Laprie, and B. Randell, “Dependability and Its Threats: A Taxonomy,” in *Building the Information Society*, Springer, Boston, MA, 2004, pp. 91–120. doi: 10.1007/978-1-4020-8157-6_13.

[48] Z. Gao and X. Liu, “An Overview on Fault Diagnosis, Prognosis and Resilient Control for Wind Turbine Systems,” *Processes*, vol. 9, no. 2, p. 300, Feb. 2021, doi: 10.3390/pr9020300.

[49] “Exploring wind farm reliability: Key concepts, databases and fault Trees,” *Renew. Sustain. Energy Rev.*, vol. 211, p. 115227, Apr. 2025, doi: 10.1016/j.rser.2024.115227.

[50] “Model-based fault detection, fault isolation and fault-tolerant control of a blade pitch system in floating wind turbines,” *Renew. Energy*, vol. 120, pp. 306–321, May 2018, doi: 10.1016/j.renene.2017.12.102.

[51] “A Comprehensive Review on Signal-Based and Model-Based Condition Monitoring of Wind Turbines: Fault Diagnosis and Lifetime Prognosis | IEEE Journals & Magazine | IEEE Xplore.” Available: https://ieeexplore.ieee.org/abstract/document/9774410

[52] “Fuzzy model-based faults diagnosis of the wind turbine benchmark - ScienceDirect.” Available: https://www.sciencedirect.com/science/article/pii/S187705091830156X

[53] “Model-based fault-detection and diagnosis – status and applications,” *Annu. Rev. Control*, vol. 29, no. 1, pp. 71–85, Jan. 2005, doi: 10.1016/j.arcontrol.2004.12.002.

[54] J. Solimine and M. Inalpolat, “An unsupervised data-driven approach for wind turbine blade damage detection under passive acoustics-based excitation,” *Wind Eng.*, vol. 46, no. 4, pp. 1311–1330, Aug. 2022, doi: 10.1177/0309524X221080470.

[55] Y. Zhao, D. Li, A. Dong, D. Kang, Q. Lv, and L. Shang, “Fault Prediction and Diagnosis of Wind Turbine Generators Using SCADA Data,” *Energies*, vol. 10, no. 8, p. 1210, Aug. 2017, doi: 10.3390/en10081210.

[56] “A wind turbine bearing fault diagnosis method based on fused depth features in time–frequency

domain," *Energy Rep.*, vol. 8, pp. 12727–12739, Nov. 2022, doi: 10.1016/j.egyr.2022.09.113.

[57] "Fault detection and diagnosis for rotating machinery: A model based on convolutional LSTM, Fast Fourier and continuous wavelet transforms," *Comput. Ind.*, vol. 125, p. 103378, Feb. 2021, doi: 10.1016/j.compind.2020.103378.

[58] "Compound faults diagnosis and analysis for a wind turbine gearbox via a novel vibration model and empirical wavelet transform," *Renew. Energy*, vol. 136, pp. 393–402, Jun. 2019, doi: 10.1016/j.renene.2018.12.094.

[59] "Multi-fault detection and failure analysis of wind turbine gearbox using complex wavelet transform," *Renew. Energy*, vol. 93, pp. 591–598, Aug. 2016, doi: 10.1016/j.renene.2016.03.025.

[60] "Wind turbine fault diagnosis based on Morlet wavelet transformation and Wigner-Ville distribution," *Renew. Energy*, vol. 35, no. 12, pp. 2862–2866, Dec. 2010, doi: 10.1016/j.renene.2010.05.012.

[61] "A Novel Characteristic Frequency Bands Extraction Method for Automatic Bearing Fault Diagnosis Based on Hilbert Huang Transform." Available: https://www.mdpi.com/1424-8220/15/11/27869

[62] "Application of AE techniques for the detection of wind turbine using Hilbert-Huang transform | IEEE Conference Publication | IEEE Xplore."Available: https://ieeexplore.ieee.org/abstract/document/5414591

[63] "An intelligent approach for engine fault diagnosis based on Hilbert–Huang transform and support vector machine - ScienceDirect." Available: https://www.sciencedirect.com/science/article/abs/pii/S0003682X13001515

[64] "Vibration Signal Analysis for Intelligent Rotating Machinery Diagnosis and Prognosis: A Comprehensive Systematic Literature Review." Available: https://www.mdpi.com/2571-631X/7/4/54

[65] "Trends in non-stationary signal processing techniques applied to vibration analysis of wind turbine drive train – A contemporary survey - ScienceDirect." Available: https://www.sciencedirect.com/science/article/abs/pii/S0888327016302758

[66] "A Data-Driven Residual-Based Method for Fault Diagnosis and Isolation in Wind Turbines | IEEE Journals & Magazine | IEEE Xplore." Available: https://ieeexplore.ieee.org/abstract/document/8408495

[67] "Coupling data-driven and model-based methods to improve fault diagnosis - ScienceDirect." Available: https://www.sciencedirect.com/science/article/abs/pii/S0166361521000087

[68] "Vibration Analysis & Condition Monitoring for Rotating Machines: A Review," *Mater. Today Proc.*, vol. 4, no. 2, pp. 2659–2664, Jan. 2017, doi: 10.1016/j.matpr.2017.02.140.

[69] "A Review on Vibration Monitoring Techniques for Predictive Maintenance of Rotating Machinery." Available: https://www.mdpi.com/2673-4117/4/3/102

[70] "Vibration Analysis for Machine Monitoring and Diagnosis: A Systematic Review - Mohd Ghazali - 2021 - Shock and Vibration - Wiley Online Library." Available:

https://onlinelibrary.wiley.com/doi/full/10.1155/2021/9469318

[71] "Automatic rule learning using decision tree for fuzzy classifier in fault diagnosis of roller bearing," *Mech. Syst. Signal Process.*, vol. 21, no. 5, pp. 2237–2247, Jul. 2007, doi: 10.1016/j.ymssp.2006.09.007.

[72] "Practical scheme for fast detection and classification of rolling-element bearing faults using support vector machines," *Mech. Syst. Signal Process.*, vol. 20, no. 7, pp. 1523–1536, Oct. 2006, doi: 10.1016/j.ymssp.2005.05.002.

[73] "Effect of number of features on classification of roller bearing faults using SVM and PSVM," *Expert Syst. Appl.*, vol. 38, no. 4, pp. 4088–4096, Apr. 2011, doi: 10.1016/j.eswa.2010.09.072.

[74] "Analysing RMS and peak values of vibration signals for condition monitoring of wind turbine gearboxes - ScienceDirect." Available: https://www.sciencedirect.com/science/article/pii/S0960148116300064

[75] "ANOVA and vibration kurtosis-based analysis of roller defects in taper bearings for condition monitoring," *Prog. Eng. Sci.*, vol. 2, no. 3, p. 100117, Sep. 2025, doi: 10.1016/j.pes.2025.100117.

[76] "A Review on Vibration-Based Condition Monitoring of Rotating Machinery." Available: https://www.mdpi.com/2076-3417/12/3/972

[77] S. Jawad and A. Jaber, "Bearings Health Monitoring Based on Frequency-Domain Vibration Signals Analysis," *Eng. Technol. J.*, vol. 41, no. 1, pp. 86–95, Sep. 2022, doi: 10.30684/etj.2022.131581.1043.

[78] "Robust condition monitoring of rolling element bearings using de-noising and envelope analysis with signal decomposition techniques," *Expert Syst. Appl.*, vol. 42, no. 22, pp. 9024–9032, Dec. 2015, doi: 10.1016/j.eswa.2015.07.064.

[79] G.-J. Feng, J. Gu, D. Zhen, M. Aliwan, F.-S. Gu, and A. D. Ball, "Implementation of envelope analysis on a wireless condition monitoring system for bearing fault diagnosis," *Int. J. Autom. Comput.*, vol. 12, no. 1, pp. 14–24, Feb. 2015, doi: 10.1007/s11633-014-0862-x.

[80] H. Geraei, E. A. V. Rodriguez, E. Majma, S. Habibi, and D. Al-Ani, "A Noise Invariant Method for Bearing Fault Detection and Diagnosis Using Adapted Local Binary Pattern (ALBP) and Short-Time Fourier Transform (STFT)," *IEEE Access*, vol. 12, pp. 107247–107260, 2024, doi: 10.1109/ACCESS.2024.3438106.

[81] H. Tao, P. Wang, Y. Chen, V. Stojanovic, and H. Yang, "An unsupervised fault diagnosis method for rolling bearing using STFT and generative neural networks," *J. Frankl. Inst.*, vol. 357, no. 11, pp. 7286–7307, Jul. 2020, doi: 10.1016/j.jfranklin.2020.04.024.

[82] J. Chen, J. Pan, Z. Li, Y. Zi, and X. Chen, "Generator bearing fault diagnosis for wind turbine via empirical wavelet transform using measured vibration signals," *Renew. Energy*, vol. 89, pp. 80–92, Apr. 2016, doi: 10.1016/j.renene.2015.12.010.

[83] W. Deng, S. Zhang, H. Zhao, and X. Yang, "A Novel Fault Diagnosis Method Based on Integrating Empirical Wavelet Transform and Fuzzy Entropy for Motor Bearing," *IEEE Access*, vol. 6, pp. 35042–35056, 2018, doi: 10.1109/ACCESS.2018.2834540.

[84] S. Osman and W. Wang, “A Morphological Hilbert-Huang Transform Technique for Bearing Fault Detection,” *IEEE Trans. Instrum. Meas.*, vol. 65, no. 11, pp. 2646–2656, Nov. 2016, doi: 10.1109/TIM.2016.2598019.

[85] A. Soualhi, K. Medjaher, and N. Zerhouni, “Bearing Health Monitoring Based on Hilbert–Huang Transform, Support Vector Machine, and Regression,” *IEEE Trans. Instrum. Meas.*, vol. 64, no. 1, pp. 52–62, Jan. 2015, doi: 10.1109/TIM.2014.2330494.

[86] C. Junsheng, Y. Dejie, and Y. Yu, “A fault diagnosis approach for roller bearings based on EMD method and AR model,” *Mech. Syst. Signal Process.*, vol. 20, no. 2, pp. 350–362, Feb. 2006, doi: 10.1016/j.ymssp.2004.11.002.

[87] X. Liu, L. Bo, and H. Luo, “Bearing faults diagnostics based on hybrid LS-SVM and EMD method,” *Measurement*, vol. 59, pp. 145–166, Jan. 2015, doi: 10.1016/j.measurement.2014.09.037.

[88] R. B. Randall and J. Antoni, “Why EMD and similar decompositions are of little benefit for bearing diagnostics,” *Mech. Syst. Signal Process.*, vol. 192, p. 110207, Jun. 2023, doi: 10.1016/j.ymssp.2023.110207.

[89] H. Li, T. Liu, X. Wu, and Q. Chen, “An optimized VMD method and its applications in bearing fault diagnosis,” *Measurement*, vol. 166, p. 108185, Dec. 2020, doi: 10.1016/j.measurement.2020.108185.

[90] R. Djemili and I. Djemili, “Nonlinear and chaos features over EMD/VMD decomposition methods for ictal EEG signals detection,” *Comput. Methods Biomech. Biomed. Engin.*, vol. 27, no. 15, pp. 2091–2110, Nov. 2024, doi: 10.1080/10255842.2023.2271603.

[91] K. Dragomiretskiy and D. Zosso, “Variational Mode Decomposition,” *IEEE Trans. Signal Process.*, vol. 62, no. 3, pp. 531–544, Feb. 2014, doi: 10.1109/TSP.2013.2288675.

[92] N. E. Huang *et al.*, “The empirical mode decomposition and the Hilbert spectrum for nonlinear and non-stationary time series analysis,” *Proc. R. Soc. Lond. Ser. Math. Phys. Eng. Sci.*, vol. 454, no. 1971, pp. 903–995, Mar. 1998, doi: 10.1098/rspa.1998.0193.

[93] Z. Wu and N. E. Huang, “ENSEMBLE EMPIRICAL MODE DECOMPOSITION: A NOISE-ASSISTED DATA ANALYSIS METHOD,” *Adv. Adapt. Data Anal.*, vol. 01, no. 01, pp. 1–41, Jan. 2009, doi: 10.1142/S1793536909000047.

[94] M. E. Torres, M. A. Colominas, G. Schlotthauer, and P. Flandrin, “A complete ensemble empirical mode decomposition with adaptive noise,” in *2011 IEEE International Conference on Acoustics, Speech and Signal Processing (ICASSP)*, Prague, Czech Republic: IEEE, May 2011, pp. 4144–4147. doi: 10.1109/ICASSP.2011.5947265.

[95] M. A. Colominas, G. Schlotthauer, and M. E. Torres, “Improved complete ensemble EMD: A suitable tool for biomedical signal processing,” *Biomed. Signal Process. Control*, vol. 14, pp. 19–29, Nov. 2014, doi: 10.1016/j.bspc.2014.06.009.

[96] I. Djemili, A. Medoued, and Y. Soufi, “A Wind Turbine Bearing Fault Detection Method Based on Improved CEEMDAN and AR-MEDA,” *J. Vib. Eng. Technol.*, vol. 12, no. 3, pp. 4225–4246, Mar. 2024, doi: 10.1007/s42417-023-01117-x.

[97] "Bearing Data Center | Case School of Engineering | Case Western Reserve University," Case School of Engineering. Available: https://engineering.case.edu/bearingdatacenter

[98] L. Saidi, J. Ben Ali, E. Bechhoefer, and M. Benbouzid, "Wind turbine high-speed shaft bearings health prognosis through a spectral Kurtosis-derived indices and SVR," *Appl. Acoust.*, vol. 120, pp. 1–8, May 2017, doi: 10.1016/j.apacoust.2017.01.005.

[99] L. Saidi, J. Ben Ali, M. Benbouzid, and E. Bechhoefer, "Wind turbine drivetrain prognosis approach based on Kalman smoother with confidence bounds," in *2018 IEEE International Conference on Industrial Technology (ICIT)*, Lyon: IEEE, Feb. 2018, pp. 1865–1870. doi: 10.1109/ICIT.2018.8352469.

[100] D. Siegel, W. Zhao, E. Lapira, M. AbuAli, and J. Lee, "A comparative study on vibration-based condition monitoring algorithms for wind turbine drive trains," *Wind Energy*, vol. 17, no. 5, pp. 695–714, 2014, doi: 10.1002/we.1585.

[101] F. Cong, J. Chen, and G. Dong, "Research on the Order Selection of the Autoregressive Modelling for Rolling Bearing Diagnosis," *Proc. Inst. Mech. Eng. Part C J. Mech. Eng. Sci.*, vol. 224, no. 10, pp. 2289–2297, Oct. 2010, doi: 10.1243/09544062JMES1958.

[102] L. Tian and Z. Peng, "Determining the optimal order of fractional Gabor transform based on kurtosis maximization and its application," *J. Appl. Geophys.*, vol. 108, pp. 152–158, Sep. 2014, doi: 10.1016/j.jappgeo.2014.06.009.

[103] R. A. Wiggins, "Minimum entropy deconvolution," *Geoexploration*, vol. 16, no. 1, pp. 21–35, Apr. 1978, doi: 10.1016/0016-7142(78)90005-4.

[104] G. L. McDonald and Q. Zhao, "Multipoint Optimal Minimum Entropy Deconvolution and Convolution Fix: Application to vibration fault detection," *Mech. Syst. Signal Process.*, vol. 82, pp. 461–477, Jan. 2017, doi: 10.1016/j.ymssp.2016.05.036.

[105] Y. Cheng, B. Chen, and W. Zhang, "Adaptive Multipoint Optimal Minimum Entropy Deconvolution Adjusted and Application to Fault Diagnosis of Rolling Element Bearings," *IEEE Sens. J.*, vol. 19, no. 24, pp. 12153–12164, Dec. 2019, doi: 10.1109/JSEN.2019.2937140.

[106] A. Chennana, A. Ahmia, A. C. Megherbi, S. Sbaa, N. Bessous, and Y. Damine, "A Comparative Study Between EMD-MCKD and EMD-MEDA Techniques for the Bearing Faults Diagnosis in Induction Motors," in *2023 International Conference on Electrical Engineering and Advanced Technology (ICEEAT)*, Nov. 2023, pp. 1–6. doi: 10.1109/ICEEAT60471.2023.10426493.

[107] W. A. Smith and R. B. Randall, "Rolling element bearing diagnostics using the Case Western Reserve University data: A benchmark study," *Mech. Syst. Signal Process.*, vol. 64–65, pp. 100–131, Dec. 2015, doi: 10.1016/j.ymssp.2015.04.021.

[108] N. Sawalhi, R. B. Randall, and H. Endo, "The enhancement of fault detection and diagnosis in rolling element bearings using minimum entropy deconvolution combined with spectral kurtosis," *Mech. Syst. Signal Process.*, vol. 21, no. 6, pp. 2616–2633, Aug. 2007, doi: 10.1016/j.ymssp.2006.12.002.

[109] Z. Liu, H. Mao, C.-Y. Wu, C. Feichtenhofer, T. Darrell, and S. Xie, "A ConvNet for the 2020s,"

Mar. 02, 2022, *arXiv*: arXiv:2201.03545. doi: 10.48550/arXiv.2201.03545.

[110] H. Liu and J. Xiang, “Autoregressive model-enhanced variational mode decomposition for mechanical fault detection,” *IET Sci. Meas. Technol.*, vol. 13, no. 6, pp. 843–851, 2019, doi: 10.1049/iet-smt.2018.5585.

[111] X. Chen, Y. Yang, Z. Cui, and J. Shen, “Vibration fault diagnosis of wind turbines based on variational mode decomposition and energy entropy,” *Energy*, vol. 174, pp. 1100–1109, May 2019, doi: 10.1016/j.energy.2019.03.057.

[112] G. Li, C. Deng, J. Wu, X. Xu, X. Shao, and Y. Wang, “Sensor Data-Driven Bearing Fault Diagnosis Based on Deep Convolutional Neural Networks and S-Transform,” *Sensors*, vol. 19, no. 12, p. 2750, Jun. 2019, doi: 10.3390/s19122750.

[113] N. Diao, Z. Wang, H. Ma, and W. Yang, “Fault Diagnosis of Rolling Bearing Under Variable Working Conditions Based on CWT and T-ResNet,” *J. Vib. Eng. Technol.*, vol. 11, no. 8, pp. 3747–3757, Nov. 2023, doi: 10.1007/s42417-022-00780-w.

[114] M. Sandler, A. Howard, M. Zhu, A. Zhmoginov, and L.-C. Chen, “MobileNetV2: Inverted Residuals and Linear Bottlenecks,” Mar. 21, 2019, *arXiv*: arXiv:1801.04381. doi: 10.48550/arXiv.1801.04381.

[115] G. Huang, Z. Liu, L. van der Maaten, and K. Q. Weinberger, “Densely Connected Convolutional Networks,” Jan. 28, 2018, *arXiv*: arXiv:1608.06993. doi: 10.48550/arXiv.1608.06993.

[116] K. He, X. Zhang, S. Ren, and J. Sun, “Deep Residual Learning for Image Recognition,” Dec. 10, 2015, *arXiv*: arXiv:1512.03385. doi: 10.48550/arXiv.1512.03385.